Simulation der Teilchendynamik in rotierenden Trommeln

DISSERTATION

zur Erlangung des Doktorgrades
der Naturwissenschaften
(Dr. rer. nat.)

dem Fachbereich Physik
der Philipps-Universität Marburg
vorgelegt

von

Christian Mathias Dury
aus Homburg a.d. Saar

Marburg/Lahn 1998

Vom Fachbereich Physik der
Philipps-Universität Marburg als
Dissertation angenommen am: 10.09.1998

Erstgutachter: Dr. habil. Gerald Ristow

Zweitgutachter: Prof. Dr. Siegfried Großmann

Tag der mündlichen Prüfung: 25.09.1998

Meiner lieben Frau

Inhaltsverzeichnis

List of Figures

Symbols

Häufig benutzte Symbole (Commonly used symbols)

γ	Dissipationskoeffizient	dissipation coefficient
ϵ_{res}	Restitutionskoeffizient	coefficient of restitution
η	Packungsdichte	packing fraction
Θ	Böschungswinkel	angle of repose
μ	Reibungskoeffizient	friction coefficient
ρ	Teilchendichte, Wahrscheinlichkeitsdichte	particle density, probability density
$\vec{\tau}$	Drehmoment	torque
Φ	Radienverhältnis	size ratio
Ω	Umdrehungsgeschwindigkeit der Trommel	angular velocity of the drum
$\vec{\omega}$	Rotationsgeschwindigkeit eines Teilchens	angular velocity of a particle
D,R	Trommeldurchmesser, -radius	drum diameter, radius
f	Füllgrad der Trommel	filling fraction of the cylinder
$\vec{F}$	Kraft	force
g	Schwerebeschleunigung	gravitational acceleration
k_s	Scherfederkraft	strength of the spring in shear direction
L	Trommellänge	drum length
m	Teilchenmasse	particle mass
N	Teilchenanzahl	number of particles
$\hat{n}$, $\hat{s}$	Einheitsvektor in Normalen-, Scherrichtung	unit vector in normal, shear direction
q	Ordnungsparameter für die radiale Segregation	order parameter for radial segregation
R, r	Teilchenradius	particle radius
r_0	Rollreibungswiderstand	coefficient for rolling resistance
T	Periodendauer	period
t_c	Charakteristische Zeit	characteristic time
$\vec{x}, \vec{v}, \vec{a}$	Teilchenposition, -geschwindigkeit und -beschleunigung	particle position, velocity and acceleration
$\tilde{Y}$	Materialhärte	material hardness related to the Young modulus

1 Zusammenfassung

1.1 Einleitung

In der Physik teilt man die verschiedenen Erscheinungsformen von Materie üblicherweise in die Aggregatzustände **fest, flüssig und gasförmig** [1] ein. Interessanter Weise können gerade Granulate, die uns in unser alltäglichen Umgebung überall begegnen, nicht in dieses Schema gepreßt werden. Das Paradebeispiel für ein Granulat ist Sand, der weltweit zu finden ist. Auch hantieren viele Industriezweige mit Granulaten. Man denke nur an Getreide in der Landwirtschaft, Erze und Kohle im Bergbau, Pillen in der pharmazeutischen Industrie, Kunststoffgranulate und Chemikalien in der chemischen Industrie, usw.; dies allein zeigt schon die industrielle Wichtigkeit von Granulaten auf [Jaeger et al., 1996]. Aber auch vom Standpunkt der Physik sind granulare Materialien hochinteressant, so können Granulate sowohl die Eigenschaften **fester** als auch **flüssiger** Stoffe zeigen. So ist es wohl kaum verwunderlich, daß Granulate schon über 200 Jahre Gegenstand wissenschaftlicher Untersuchungen sind. Nichtsdestotrotz ist das grundlegende Verständnis granularer Materialien bei weiten noch nicht vollständig, und eine allgemein gültige Theorie ist noch nicht vorhanden. Ein Grund dafür ist sicherlich gerade die Eigenschaft, die diese Materialien interessant machen: das gleichzeitige Vorhandensein von Festkörper- und Flüssigkeitseigenschaften, sowie die Tendenz, daß Granulate zum Entmischen[2] neigen. Um mehr über Granulate zu erfahren, wurden viele Experimente durchgeführt, um aus den so gewonnen Erkenntnissen eine phänomenologische Theorie zu gewinnen. Da aber fast alle Meßmethoden nicht zerstörungsfrei in das Experiment hineinschauen können, ist der Anwendungsbereich der daraus gewonnenen Theorien immer sehr speziell auf eine Eigenschaft, Geometrie, o.ä. festgelegt.

Auch die Beschreibung von Granulaten durch Kontinuumsmodelle steckt noch in den Kinderschuhen [Jenkins and Savage, 1983; Lun et al., 1984; Goldshtein and Shapiro, 1995] und es ist fraglich, ob sie generell dazu fähig sind [Du et al., 1995]. Diese Modelle sind im allgemeinen nur für geringe Dichten gültig und brechen bei Kompaktierung des Granulates zusammen; so können sie z.B. nicht die Brückenbildung beschreiben, die einen Trichter am weiteren Ausfließen hindert [3].

Um nun mehr über die grundlegenden Eigenschaften von Granulaten zu erfahren, müßte man mehr darüber wissen, was überhaupt in den Experimenten passiert. Eine vielverspre-

[1] Von den im Alltag nicht üblichen Plasmen abgesehen.

[2] Segregieren

[3] Dies kann man gut bei Sanduhren beobachten, die manchmal aufhören zu fließen, obwohl noch Sand in der oberen Hälfte zu finden ist.

chende Technik dafür hat sich erst in letzter Zeit aufgetan, die bildgebende Kernspinresonanz (Nuclear Magnetic Resonance Imaging – MRI) [Nakagawa, 1994; Hill et al., 1997b; Nakagawa et al., 1997a]. Mit ihrer Hilfe kann man auch in das Material hineinsehen, dies ist aber erstens nur mit einer sehr groben Zeitauflösung (ca. 60 sec.) möglich, was viel zu langsam ist, um die Dynamik einzelner Teilchen zu beobachten, und zweitens ist nicht jedes Material für MRI geeignet. Sehr beliebt sind dabei die flüssigkeitsgefüllten pharmazeutischen Pillen; durch den Wasserkern erzeugen sie ein klares Kernspinresonanzsignal. Der Nachteil liegt aber auf der Hand: Teilchen mit flüssigem Inneren werden sich rein mechanisch schon anders verhalten (man denke allein an die Rotation), als feste Teilchen.

Mit dem Aufkommen der heutigen Generation von Superrechnern eröffnet sich ein neuer Weg, um ein besseres Verständnis von granularen Materialien zu bekommen: den der **Simulation**. Mit Hilfe von Simulationen ist es möglich, die Trajektorien einzelner Teilchen zu verfolgen und somit etwas über die Dynamik des Granulates zu erfahren. Auch hofft man durch diese Detailkenntnisse zu allgemein gültigen Aussagen und Gesetzmäßigkeiten zu kommen. Die Probleme, die die Simulation mit sich trägt, kann man durch zwei Fragen konkretisieren:

- Können realistische Systemgrößen überhaupt simuliert werden ?
- Beschreibt die Simulation die Wirklichkeit, oder sind die zu erwartenden Ergebnisse nur Artefakte der Simulationstechnik ?

Die erste Frage läßt sich mit einem klaren “Ja” beantworten. Mit den heutzutage zur Verfügung stehenden Rechnern lassen sich durchaus Systemgrößen simulieren, die auch in Laborexperimenten erreicht werden; Systemgrößen industrieller Anwendungen sind zwar immer noch um Größenordnungen zu groß[4], aber um die physikalischen Eigenschaften zu verstehen auch nicht unbedingt notwendig.

Die zweite Frage ist etwas komplizierter: A priori gibt es bestimmt genügend Modelle, die nicht die Realität beschreiben. Die Aufgabe besteht ersteinmal darin, die “richtige” Physik in das Modell zu inkorporieren. Das Modell muß so gewählt werden, daß in den Simulationen die aus den Experimenten zugänglichen Größen verläßlich reproduziert werden. Daraus lassen sich dann aber schon Schlüsse über die Natur von Granulaten ziehen; z.B. welche Kräfte sind wichtig, durch welche vereinfachten Kräfte lassen sich die Teilchen schon beschreiben. Dies allein ist schon sehr hilfreich, um die charakteristischen Eigenschaften und die Physik der Granulate zu verstehen.

Es lohnt sich also die Mühe, granulare Materialien zu simulieren. Einerseits läßt sich schon viel aus der Anpassung der Simulation an die Realität lernen und andererseits können dann Vorhersagen über das Verhalten von Granulaten gemacht werden, die im

[4] Spätestens in der übernächsten Superrechnergeneration werden sich aber auch diese Systemgrößen erreichen lassen.

Experiment so nicht gemessen werden können. In dieser Arbeit soll nun die Teilchendynamik granularer Materialien anhand der speziellen Geometrie der rotierenden Trommeln untersucht werden.

1.2 Rotierende Trommel

Die horizontal rotierende Trommel ist sozusagen der Prototyp eines der vielen Geräte zur Mischung granularer Materialien, wie z.B. Betonmischer, Müllverbrennungsöfen oder Trommeln für das Kaffeerösten, Beschichten, Trocknen, usw.. Viele Anwendungen in der Verfahrenstechnik greifen auf das Prinzip der rotierenden Trommel zurück um Granulate zu bearbeiten und zu mischen. Jedoch weiß man, daß Granulate die Tendenz haben zu segregieren; dieser Effekt ist aber meistens unerwünscht und steht dem ursprünglichen Zweck der möglichst gleichmäßigen Verteilung des Granulates in der Trommel entgegen. Wünschenswert wäre es nun genaueres über die Dynamik der Teilchen in der rotierenden Trommel zu erfahren, da man dann gezielte Veränderungen in den Prozessen vornehmen könnte, um unerwünschte Effekte zu verringern.

1.2.1 Böschungswinkel

Eine wichtige Größe ist der Böschungswinkel (der Winkel zwischen der Materialoberfläche und der Horizontalen). Wird die Böschung zu steil und daher nicht mehr stabil lösen sich Lawinen ab, die zu einer Erniedrigung des Böschungswinkels führen. Den Böschungswinkel, der direkt nach einer Lawine herrscht, nennt man den statischen Böschungswinkel. In diesen Lawinen spielt sich hauptsächlich die Physik ab, da der Rest sich fast wie ein fester Körper verhält. Durch die Rotation der Trommel wird das Material nach oben transportiert, das dann durch Lawinen wieder abtransportiert wird; ab einer bestimmten Rotationsrate werden die Lawinen so häufig, daß sie nicht mehr voneinader unterschieden werden können und sich ein kontinuierlicher Oberflächenfluß bildet. In diesem Fall spricht man von dem dynamischen Böschungswinkel.

1.2.2 Segregation

Auch vom Standpunkt der Physik ist das Phänomen der Segregation interessant, widerspricht es doch auf dem ersten Blick dem Entropiesatz, da sich die Entropie ja verringert, wenn sich zwei Materialien entmischen. Auf den zweiten Blick erkennt man allerdings, daß die rotierende Trommel kein abgeschlossenes System ist, sondern ständig Energie durch die Rotation hinzugeführt wird. Deswegen kann auch das Prinzip, daß ein System in den energetisch günstigsten Zustand übergeht, nicht angewandt werden. Generell ist zu beobachten, daß Granulate, die in Größe, Dichte, Form oder anderen Eigenschaften verschieden sind zur Segregation neigen. Dabei wirkt sich der Größenunterschied wohl am meisten bei der Segregation aus, gefolgt vom Dichteunterschied.

In rotierenden Trommeln kann man zwei Arten von Segregation beobachten:

- *Radiale Segregation*: Die kleineren, bzw. dichteren Teilchen sammeln sich in der Nähe der Rotationsache an und bilden sozusagen einen inneren Kern mit kleinen (dichten) Teilchen. Diese Segregation findet auf sehr kurzen Zeitskalen statt; nach ein oder zwei Trommelrotationen kann man schon sehr schön einen Kern sehen.
- *Axiale Segregation*: Die axiale Segregation hingegen tritt nur bei einigen Teilchenkombinationen mit verschiedenen Teilchenradien auf und braucht wesentlich länger, um sich zu entwickeln (von einigen Minuten bis hin zu Tagen). Bei der axialen Segregation formen sich Bänder kleiner Teilchen entlang der Rotationsachse, die von Bereichen mit großen und kleinen Teilchen, die wiederum radial segregiert sein können, getrennt werden

1.3 Methodik

Eine geeignete Methode zur Simulation dieser Systeme ist die Discrete Element Method (DEM) [Cundall and Strack, 1979] (manchmal als “soft sphere model” bezeichnet), sie ist eine der Molekulardynamik (MD) verwandten Methode, in der auch vergangene Zeitschritte mit berücksichtigt werden können. Der Vorteil gegenüber anderen Methoden ist:

- die Methode enthält eine echte Dynamik,
- alle Teilchenkoordinaten sind zu jedem Zeitpunkt bekannt,
- physikalische Gesetze sind leicht zu inkorporieren, und Parameter lassen sich direkt aus Experimenten bestimmen.

Der Nachteil:

- durch die Berechnung jeder einzelnen Kollision entsteht ein immenser Rechenbedarf in Bezug auf Rechnerleistung und Speicherplatz. Für Teilchen, deren Radius groß genug ist, um die van-der-Waals Kräfte zu vernachlässigen und nur noch Wechselwirkungen mit den nächsten Nachabarn berücksichtigt werden müssen, ist die benötigte Rechnerleistung zwar immer noch sehr groß, aber schon im Bereich des Möglichen.

Um diesen Nachteil abzumildern und auch realistische Systemgrößen simulieren zu können, wurde das Simulationsprogramm für Parallelrechner (wie z.B. die CrayT3E oder die IBM SP2) entwickelt und optimiert. Mit dieser neusten Rechnergeneration lassen sich nun bis zu ca. 500.000 Teilchen simulieren, dies entspricht gängigen Größen in Laborexperimenten, mit denen die Resultate auch verglichen werden können.

Um die Simulation realitätsnah zu gestalten, wurden von Prof. M. Nakagawa an der School of Mines in Golden (Colorado) Experimente durchgeführt, mit denen die Simulationen dann verglichen wurden; dabei wurde hauptsächlich der Böschungswinkel und die Lawinenstatistik betrachtet. Bei einem Besuch bei Prof. M. Nakagawa sind dann

nocheinmal Versuche zur radialen und axialen Segregation durchgeführt worden[5]. In dieser Arbeit werden hauptsächlich Senfkörner, Mohnsamen und Glaskugeln betrachtet, da mit diesen Granulaten die Experimente durchgeführt worden sind.

1.4 Ergebnisse

Im ersten Teil wird die Numerik vorgestellt und verschiedene Kraftgesetze für unsere Simulation verglichen (Kapitel 3). Dabei stellt man fest, daß das Hookesches Gesetz in Normalenrichtung für die von uns betrachteten Meßgrößen ausreichend ist [6] und, daß für die Tangentialkräfte die viskose Reibung eine gute Näherung für uns darstellt (solange die Umdrehungsgeschwindigkeit nicht zu klein wird, $\Omega > 10$rpm). Danach wird der Böschungswinkel genauer untersucht, um unsere Parameter an die Experimente anzugleichen (Kaptiel 4). Nach einem Überblick über die verschiedenen Ω-Bereiche, wird der Böschungswinkel, basierend auf einer zugrundeliegenden Theorie von Zik et al. [1994], berechnet. Da die Übereinstimmung von Experiment (Senfkörneren), Simulation (mit nichtrotierenden Teilchen) und Theorie hervorragend ist, kann man sagen, daß auch Teilchen ohne Rotation in der Simulation eine Berechtigung haben, falls die Rotation der Teilchen im Experiment durch ihre Form (z.B. elliptisch) unterdrückt wird. Dies ist bei Glaskugeln nicht der Fall und in diesen Simulationen müssen Teilchen mit Rotation betrachtet werden. Desweiteren wird in Kapitel 5 der Einfluß der Randeffekte untersucht, da die experimentelle Messung des Böschungswinkel meistens am Trommelende stattfindet. Auch hier bekommen wir eine hervorragende Übereinstimmung zwischen den Simulationen und dem Experiment; außerdem finden wir, daß der Oberflächengradient in Richtung der Rotationsachse in einem weiten Bereich unabhängig von Teilchenradius und Trommelradius ist. Die Übereinstimmung von Simulation und Experiment in Kapitel 4 und 5 sind so gut, daß man nicht fürchten muß, daß die Ergebnisse aus den Simulationen nur numerische Artefakte sind.

In Kapitel 6 wird die radiale Segregation in 2- und 3- dimensionalen Trommeln untersucht. Für den quantitativen Vergleich von Segregationsstärke und -geschwindigkeit wird der sogenannte Ordnungsparameter q eingeführt. Bis dahin war keine vernünftige allgemeine Größe zur Charakterisierung der radialen Segregation vorhanden, viele Experimente haben den “Endzustand” untersucht und daraus rückwirkend die Segregation beschrieben. Da aber dieser “Endzustand” nicht immer gleich ist, waren die Daten aus verschiedenen Experimenten nicht unbedingt quantitativ vergleichbar. In der 3-dimensionalen Trommel wurde einerseits der Effekt des geometrischen Mischens auf die Segregation untersucht und anderseits gezeigt, daß radiale Segregation schon bei beliebig kleinen Radiendifferenzen stattfinden kann[7].

[5] Daten aus Experimenten, die nicht extra gekennzeichnet sind, wurden von mir in Golden bei Prof. M. Nakagawa durchgeführt.

[6] Betrachtet man allerdings die Schallausbreitung in Granulaten ist dies nicht mehr unbedingt gegeben.

[7] In Vibrationsexperimenten wurde ein Schwellenwert angegeben, ab der Segregation stattfindet [Vanel et al., 1997] unterdessen mit einem simplen numerischen Modell keiner in der rotierenden Trommel

In Kapitel 7 fangen wir nicht mit einem gemischten Zustand an, sondern mit einer scharfen Front in der Mitte der Trommel (links und rechts von der Mitte sind Teilchen mit verschiedener Größe eingefüllt); motiviert durch die Tatsache, daß bei Mischungen, in denen axiale Segregation auftritt, diese Fronten ebenfalls stabil sind und sich nicht auflösen[8]. Dabei wird zuerst ein reiner Diffusionsprozess angenommen und untersucht, welchen Einfluß unterschiedliche Reibungskoeffizienten und Dichten der Teilchen auf den Diffusionsprozeß haben. Im zweiten Teil werden die mikroskopischen Diffusionskonstanten und Driftgeschwindigkeiten in den einzelnen Abschnitten der Trommel untersucht und festgestellt, daß für unterschiedliche Dichten der Teilchen der Druckunterschied am Interface es zu einem Kernfluß kommen läßt, d.h. die dichteren Teilchen breiten sich nicht zuerst über die Oberfläche aus, sondern im Inneren des Materials. Diese Art von Kernfluß wurde bisher für nicht möglich gehalten und könnte in Bezug auf die axiale Segregation einen großen Einfluß haben, da eventuell nicht nur die hier untersuchten Dichteunterschiede der Teilchen zu solch einem Verhalten führen können.

vorhergesagt wurde [Baumann et al., 1994].

[8] Um die axiale Segregation selbst zu untersuchen, reicht die Rechenkapazität nicht aus; wir simulieren typischerweise bis zu 50s, die sehr kurz in Bezug auf die typischen Zeiten der axialen Segregation sind.

2 Introduction

The behavior of granular materials is of great technological interest [Jaeger et al., 1996], and its investigation has a history of more than two hundred years. Nevertheless the basic physical understanding of granular media is far from being complete. One of the reasons for this is, that granular media can be in a solid state and at the same time granular material can flow like a liquid. To study this complex system we are using numerical methods.

2.1 Segregation

One of the most puzzling phenomena encountered in granular matter is segregation of a polydisperse mixture of particles. In spite of much work, relatively little is known about the basic physical processes involved in the dynamics of the segregation of granular media and many puzzles remain to be solved in this field. Apart from posing numerous fundamental and difficult questions from a theoretical point of view, knowledge of segregation is needed for many industrial applications. The segregation of particles with different properties is a ubiquitous process of major importance in areas as agriculture, geophysics, material science, and almost all areas of engineering, i.e. involving preparation of food, drugs, detergents, cosmetics, ceramics, etc.. Segregation also appears during industrial processes such as in drying and coating of granular material in rotating kilns. A common feature of all these processes is the dynamical interplay of polydisperse granular particles. Segregation can be brought about by many processes including pouring, shaking, vibration, shear and fluidization (for a short review see [Dury et al., 1998b]). For such systems the random mixed state is not a stable state and the different particle types tend to separate. In most cases, the particle size is by far the most important property controlling segregation and size segregation is observed even in processes designed for particle mixing; also for particles which differ in density, radial segregation is observed [Donald and Roseman, 1962; Williams, 1976; Bridgewater, 1976]. However, all these articles describe mechanisms for the phenomena rather than an explanation of the effects; i.e. they tell us how the particles move and not why. Size segregation seems to contradict equilibrium statistical mechanics since the density of the overall packing decreases with the amount of segregation, i.e. entropy is reduced by segregation.

2.1.1 Size segregation

Size segregation can occur whenever a mixture of particles of different sizes is disturbed in such a way that a rearrangement of the particles occurs; i.e. the mixture gets flu-

idized or expanded. There gaps between particles will occur, allowing a small particle to transverse through whereas for large particles the gaps are too narrow.

2.1.2 Density segregation

A similar mechanism is valid for particles with a higher density, here the denser (heavier) particles can shove the lighter particles away during rearrangements and thus segregate.

2.2 Granular mixtures in a rotating drum

In this thesis, we are studying the segregation of a binary mixture of granular material in a rotating drum. In industrial processing, such devices are mostly used for mixing different kinds of particles, but it is well known that particles of different sizes have the tendency to segregate in radial [Cantelaube and Bideau, 1995; Clément et al., 1995] and axial direction [Nakagawa, 1994; Hill and Kakalios, 1994; Oyama, 1939; Donald and Roseman, 1962] which might counteract such an attempt. In this systems, the surface flow consists most of the time out of small and large particles and can also be viewed as a two phase flow. Usually the drum is roughly about half filled and rotated along the cylinder axis; the drum itself is tilted, so that the cylinder axis is perpendicular to the direction of the gravitation. When granular materials are put in a rotating drum, avalanches along the surface are observed [Rajchenbach, 1990]. The solid block gets rotated upwards and on top of the solid block a fluidized layer is formed with downward flow. For a small angular velocity Ω there are distinct avalanches which are well separated, for larger angular velocities these avalanches follow more rapid to each other till there is a continuous downwards flow for a particular region of the angular velocity Ω. For even higher speeds, the particles are centrifuged to the drum wall. In our simulation we are mostly in the continuous flow regime. Recently, two-dimensional systems were also studied numerically [Ristow, 1994b; Baumann et al., 1995; Ristow, 1996] and could reproduce many of the experimental results (a cross section of a half filled drum is shown in Fig. 2.1(a) and Fig. 2.1(b)).

2.2.1 Unary mixtures

As mentioned before, the rotating drum is an archetype of a mixing device, but still with an unary mixture (e.g. colored beads of the same type) mixing is not as easy as it seems to be, it depends on the filling fraction of the drum due to geometrical effects, since avalanches are the only mechanism for mixing. Metcalfe et al. [1995] investigated experimentally such a system and the results were supported by a theory of Peratt and Yorke [1996]. Although these authors limited their investigations to the discrete avalanche regime, it seems permissible to apply their ideas in the continuous flow regime.

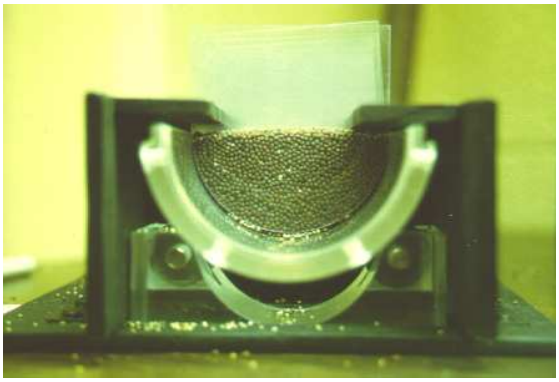

(a) Experimental cross section of a rotating drum with an unary mixture of black mustard seeds.

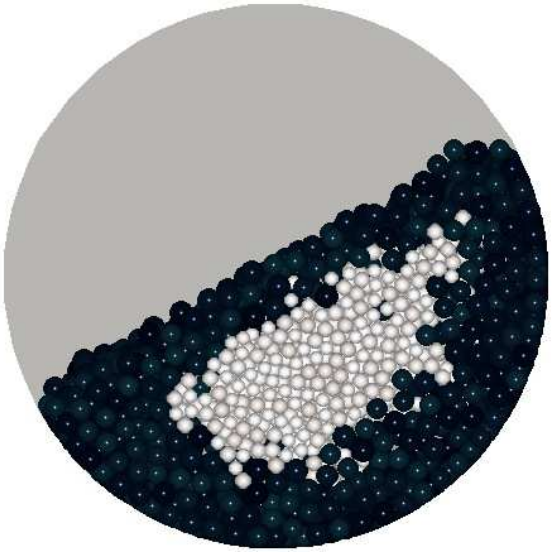

(b) Simulation of a binary mixture. The small (white) particles show a superb radial segregation and nearly no large (black) particle is found in the core.

Figure 2.1: Cross section of the rotating drum.

2.2.2 Binary mixtures

Radial segregation - - The kinematics of the segregation happen only in the shear flow along the surface, here the small particles can percolate through the big ones in the flow and get trapped by the solid block beneath before they can reach the cylinder wall. Through the continuous solid block rotation, a core of small particles at the center of the drum below the surface flow is formed, this we call radial segregation. An example from the simulation if shown in Fig. 2.1(b). This radial segregation takes place on very short time scales, it also happens in a two-dimensional rotating drum [Cantelaube and Bideau, 1995; Clément et al., 1995], however in three spatial dimensions, radial segregation is more easily to achieve, since the voids between the particles are connected by a network and small particles can traverse more easily through it than the large particles, which will lead to a better segregation. Also in three dimensions, small particles colliding with larger ones can be deflected parallel to the direction of the rotational axis and therefore the velocity in direction of the downwards flow is reduced. Hence the particles have more time to segregate until they hit the wall. Another point which has to be noted is that depending on the filling fraction there is also geometrical mixing which competes with the radial segregation (see Chapter 6).

Axial segregation - On the other hand, axial segregation happens on a much longer time scale than radial segregation, here after some minutes to hours axial bands are

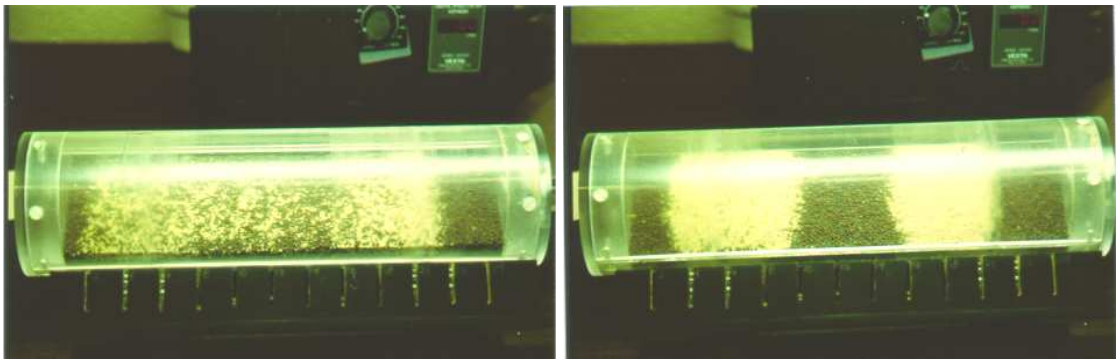

(a) After a couple of minutes. *(b) After one hour.*

Figure 2.2: Experimental pictures of axial segregation in a rotating drum with black mustard seeds (black) and poppy seeds (yellow).

formed. An example is shown in Fig. 2.2 for a 50:50 volume fraction of poppy seeds (yellow) and mustard seeds (black) rotating at 15rpm. Initially, the two components were well mixed but band formation at the end caps is already visible after rotating for a few minutes (see Fig. 2.2(a)). A nearly complete segregation was achieved after 70min, shown in Fig. 2.2(b), and the location and width of the bands hardly changed when rotated for another 5 hours. Also in contrast to the radial segregation, not all polydisperse systems show axial segregation; this is still an unsolved question whether a polydisperse mixture of particles will eventually segregate axially or not. This phenomenon of axial segregation is long known, but the nature of these bands and whether they are stable or not is still hotly debated [Nakagawa, 1994; Zik et al., 1994; Hill and Kakalios, 1995; Frette and Stavans, 1997] .

One suggested mechanism builds on the fact that axial segregation only occurs when the smaller particles have a higher angle of repose (the angle of repose is the angle between the horizontal and the surface of the granular mixture) [Das Gupta et al., 1991]. Due to local fluctuations, there will be regions with less small particles and therefore with a lower angle of repose. Now the larger particles from the sides where the angle of repose is higher will go into this region and therefore enlarge the fluctuations (Fig. 2.3). This systematic self-concentrating effect now leads to zones with no large particles and zones with a very high percentage, eventually 100%, of large particles. Another possible mechanism is due to the percolation of small particles in the solid block, but this would be a much slower mechanism.

2.3 Organization of the thesis

Chapter 3 The numerical implementation will be presented and different force laws for the particle collisions are discussed.

Chapter 4 Here we investigate the angle of repose in dependence of the angular velocity and

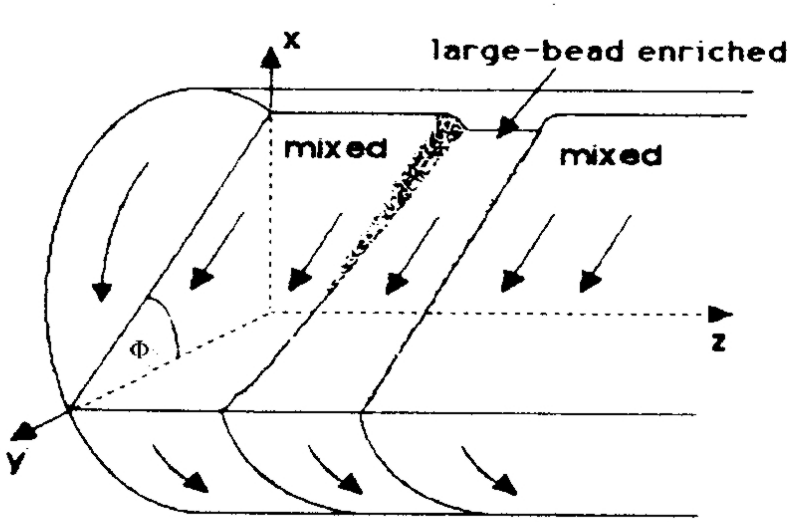

Figure 2.3: Schematic drawing of the surface of rotating beads, indicating bead height variation with concentration [Hill and Kakalios, 1994].

compare the results from experiment, simulation and theory.

Chapter 5 The influence of the boundary on the angle of repose will be studied, mainly for different particle diameters and drum lengths.

Chapter 6 An order parameter q for the radial segregation will be presented and for a two- and three-dimensional rotating drum the segregational behavior will be investigated.

Chapter 7 The diffusion of an initially sharp front in a three-dimensional rotating drum will be investigated. The diffusion process will be first approximated by a pure diffusion law, for particles which differ in size an additional drift term will be considered. There we also will see the possibility of core flow.

3 Numerical implementation

To study particle dynamics it is necessary that the used model includes:

1. a physical time scale
2. more than just geometrical effects
3. individual particles for microscopic evaluation of the data (as diffusion constants).

To include these demands we use a method most widely used to model the dynamics of granular materials called *discrete element method* (DEM) which is essentially a *molecular dynamics method* (MD) including the particle history [Cundall and Strack, 1979]. In order to use a time integration scheme, we have to write down the equations of motion for all particles in the granular system. We approximate each particle i by a sphere with radius R_i, angular velocity $\vec{\omega}_i$ and mass m_i. Since the diameters of granular particles are in the mm or cm range, the van-der-Waals forces can be neglected and the only forces, besides external forces like gravity or a fluid field, are the collisional forces. We are left with binary collisions which lead to the equations of motion via the superposition principle. During collisions, we can distinguish between forces in the normal direction $\hat{n}$, which is given by the line connecting the two centers of mass of the colliding particles. and the forces in tangential direction $\hat{s}$, which lies in the plane perpendicular to $\hat{n}$; this is sketched in Fig. 3.1. Note that the direction of $\hat{s}$ is not unique for collisions in three dimensions and we require that $\hat{s}$ lies in the plane spanned by the relative velocities of the colliding particles and the normal direction as well. During contacts the two particles overlap, which results in a repelling force. This overlapping can be viewed as an elastic deformation of the particles during contact, so after the collision the particles are spherical again. Normally, materials who are deformated by forces will not relax instantly to the original shape whenever the forces vanish, instead it will take some definite time till the original shape is restored. If we consider this, we have to put rolling friction into it.

Close-packed structures are avoided by using particles with different sizes in all our simulations (in two and three dimensions). In Fig. 3.2 a simulated system of an extended cylinder is shown.

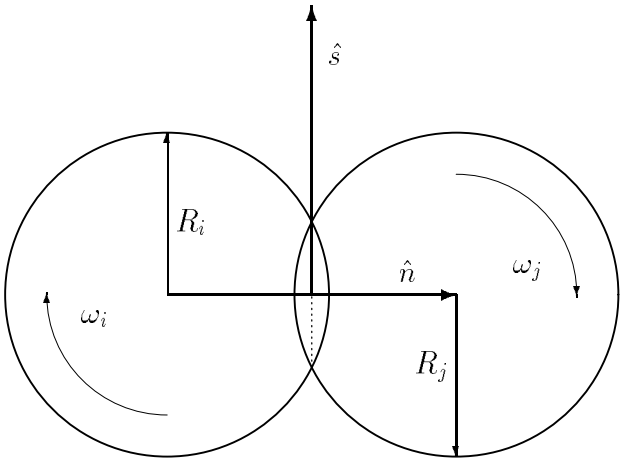

Figure 3.1: Sketch of the collision between two particles.

3.1 Normal and tangential forces

To solve this system with DEM simulations we utilize the so called **Verlet algorithm** [Allen and Tildesley, 1987]. By knowing the positions of all particles for two successive times, or alternatively the positions and velocities at a given time, the future behavior of the system is fully determined by the Forces $\vec{F}_i$ acting on each particle. Whenever two particles i and j are closer than the sum of their radii, particle j exerts a force on particle i and vice versa. The relative velocity of these two particles is

$$\vec{v}_{ij} := \vec{v}_i + (\vec{\omega}_i \times \hat{n}) - (\vec{v}_j + (\vec{\omega}_j \times (-\hat{n})))$$

at the contact point. For non-rotating particles $\vec{\omega}_i$ is set to zero.

3.1.1 Normal forces

Two type of forces are commonly used in DEM type simulations to model the collisional dynamics in the normal direction during collisions. An elastic restoration force, $F_{\text{N,el}}$, modeled as a spring and a dissipative force, $F_{\text{N,diss}}$, modeled as a dash-pot.

- **Elastic, repulsive contact force in normal direction:**

$$F_{\text{N,el}}^{(ij)} = \tilde{Y}(m_{\text{eff}}, r_{\text{eff}}) \ ((R_i + R_j) - \mid \vec{x}_i - \vec{x}_j \mid)^{\nu+1} \quad , \tag{3.1}$$

where $\tilde{Y}$ is related to the Young modulus of the investigated material and $|\vec{x}_i|$ the position of the center of mass of particle i. ν determines whether we get a Hooke like force ($\nu = 0$) or a Hertzian contact force ($\nu = \frac{1}{2}$).

Drake and Walton [1995] investigated the collisions of acetate spheres experimentally and found, that they showed an almost linear loading as function of approach (force-displacement curve). Therefore we can use in certain cases a Hooke like force, which is what we are normally doing.

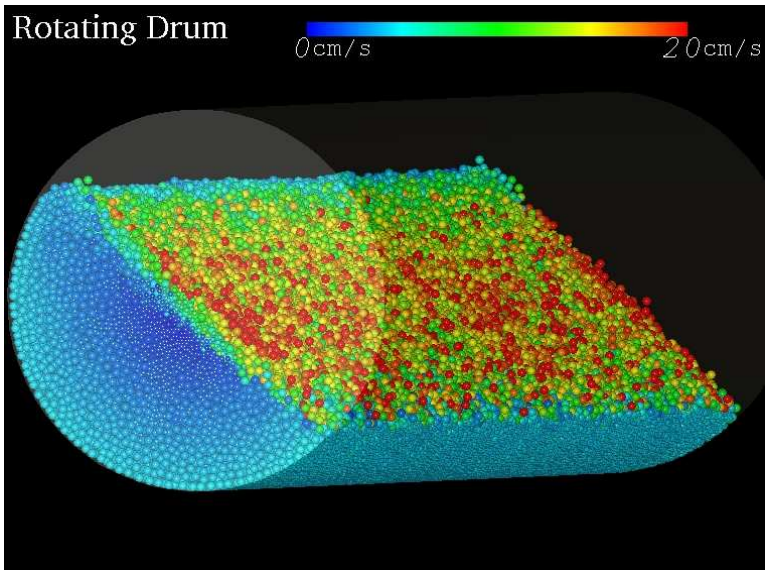

Figure 3.2: Picture of a simulation of the drum looking from the side. The grain velocities are color coded (see legend).

- **Dissipation in normal direction:** For the dissipation force one might try a relation of the form:

  (3.2) $$F_{\text{N,diss}}^{(ij)} = -\gamma_n(m_{\text{eff}}, r_{\text{eff}})\,((R_i + R_j) - \mid \vec{x}_i - \vec{x}_j \mid)^{\beta}\ \vec{v}_{ij} \cdot \hat{n}\ ,$$

  where $\gamma_n(m_{\text{eff}}, r_{\text{eff}})$ denotes the dissipation coefficient which is directly related to the coefficient of restitution $\epsilon_{res} = \frac{|\vec{v}_{ij}^{\text{after}} \cdot \hat{n}|}{|\vec{v}_{ij}^{\text{before}} \cdot \hat{n}|}$. Whereas β switches between linear and non-linear dissipation, e.g. needed by the contact law of Kuwabara and Kono [1987].

For various values of ν and β we get different normal forces (repulsion and damping).

(3.3) $\nu = 0, \beta = 0$: Viscoelastic force law

(3.4) $\nu = \frac{1}{2}, \beta = \frac{1}{4}$: Hertzian force with Tsuji-like damping.

(3.5) $\nu = \frac{1}{2}, \beta = \frac{1}{2}$: Hertzian force with Kurabawa-Kono damping term.

and also for particles without rotation

(3.6) $\nu = 0, \beta = 0$: Viscoelastic force law for particles without rotation as (3.3), but with switched off rotation.

and for the

(3.7) $\nu = 0, \beta = 0$: Viscoelastic force law without rotation and with parameters adjusted to the experiment.

The model parameters for the normal direction $(\tilde{Y}, \gamma)$ are directly determined out of experiments, so we have no free parameter for the normal forces, which quantitates our simulation.

3.1.2 Tangential forces

There are numerous proposals for tangential forces, because the underlying physics of the shear forces are not yet fully understood, and so the frictional forces we are using are just forces who model the real forces.

- **Dynamic friction:** The simplest, velocity-dependent shear force in tangential direction has the form:

$$f_{\text{fric}}^{(ij)} = -\gamma_s \vec{v}_{ij} \cdot \hat{s}(t) \; . \tag{3.8}$$

  This is a viscous friction where the force is proportional to the relative velocity. Even though this viscous approach lacks a physical justification on the microscopic level, it was shown that it agrees with a direct implementation of the non-continuous Coulomb friction law, $f_C^{(ij)} = -\text{sign}(v_{ij})\mu|F_n^{(ij)}|$, if a high enough value of γ_s is chosen [Schäfer et al., 1996; Radjai et al., 1997]. This viscous force model is used extensively in the literature as a good approximation for granular flows. In fact it is true, that particles with zero particle velocity are allowed to "creep", but in our system the time scale of this "creep" is at least two orders of magnitude larger than typical time scales (like the revolution time). So this force model is well justified for the investigated system as long as the angular velocity is large enough.

- **Static friction:** A more realistic (and much more CPU consuming) approach records the total displacement of the first point of contact of a collision. This frictional force in tangential direction is modeled via a spring with stiffness, k_s, as

$$f_{\text{fric}}^{(ij)} = -k_s \int \vec{v}_{ij} \cdot \hat{s}(t) dt \; . \tag{3.9}$$

  For the static shear force we put upon contact a linear spring between the two particles which results in a restoring force, i.e. the friction is proportional to the displacement of the original contact points. This frictional law leads to a finite angle of repose for a heap of particles as is observed in nature.

Due to Coulomb's criterion, which states that the shear force cannot exceed the normal force multiplied by the friction coefficient μ, the magnitude of the shear force, F_{shear}^{v}, is given by

$$F_{\text{S}}^{(ij)} = \text{sign}(f_{\text{fric}}^{(ij)}) \;\; \min(f_{\text{fric}}^{(ij)}, \mu \mid F_{\text{N,el}}^{(ij)} + F_{\text{N,diss}}^{(ij)} \mid) \; . \tag{3.10}$$

The model parameters $(k_s(\gamma_s), \mu)$ have the following physical interpretation: the pair $k_s(\gamma_s)$ and μ controls the energy loss and static friction in the shear direction, e.g. via

the surface roughness [Foerster et al., 1994]. A detailed discussion of the different force laws is given in Schäfer et al. [1996] and a review of different applications using granular dynamics is given in Ristow [1994a].

3.1.3 Wall contacts

During particle–wall contacts, the wall is treated as a particle with infinite mass and infinite radius. In the tangential direction the static friction force is used. This was motivated by the observation that when particles flow along the free surface, they dissipate most of their energy in collisions and can come to rest in voids left by other particles. This is not possible at the flat drum boundary. In order to avoid additional artificial particles at the walls which would make the simulations of three-dimensional systems nearly infeasible, we rather use the static friction law to avoid slipping and allowing for a static surface angle when the rotation is stopped.

3.1.4 Rolling resistance

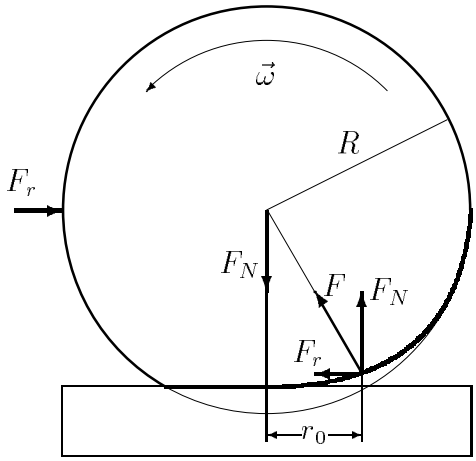

Figure 3.3: Schematic sketch of a viscoelastic rolling sphere on a hard surface.

If we consider glass beads for our simulations, we see that one of the most distinct properties of a glass bead is its ability to roll. Therefore rolling had to be included into our model. The drawback was that a glass bead would have had a Coulomb friction of zero applying our frictional laws; i.e. a glass sphere would start to roll even on an infinitesimal inclined plane or a particle would roll on forever on every flat plane, which in reality clearly does not occur. For an ideal elastic particle, the deformation of the particle would be symmetric to the point of contact and therefore the resulting counter force of the plane would be exactly opposite to the gravitational force F_N for all times. In reality the deformation is not elastic, i.e. the deformation lags behind as is indicated in Fig. 3.3 for a particle on an ideal hard plane. The counter force of the plane F acting on the particle

gets mediated by the deformation of the particle. The point where this force acts on is shifted slightly by r_0 to the back, the normal component of F compensates the gravitational force F_N exactly (otherwise the particle would bounce); leaving the tangential component of F which acts as rolling resistance which must be compensated by a dragging force for a particle with constant velocity on a flat plane. Also simulation shows that the angle of repose is much too small in comparison with experiment without rolling resistance. To overcome this weakness we add rolling resistance [Johnson, 1985] to our model, see Fig. 3.3, by using

$$F_r = \frac{r_0}{R} F_N \quad . \tag{3.11}$$

Here the rolling resistance r_0 is a constant material parameter and results from the slight viscoelasticity of the materials. r_0 is of the order of $10^{-3} - 10^{-5}$mm for most materials. For particle-particle interactions, we take the same law for rolling resistance as for particle-wall interactions. The rolling resistance acts as a net torque constructed out of a force couple F_r with

$$F_r = |F_N| \frac{r_0}{R} (\hat{n} \times \hat{s}). \tag{3.12}$$

We also have to consider that the rolling resistance can only decrease angular momentum, but never revert it. And so we have to limit F_r by the quantity that would reduce the

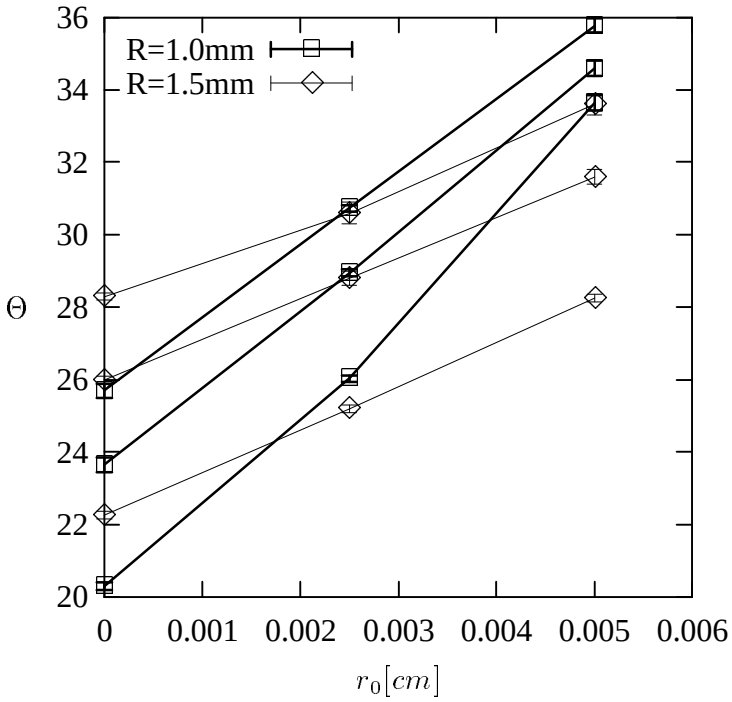

Figure 3.4: Angle of repose for different friction coefficients and particle diameters of 1.0 mm and 1.5 mm for three different values of μ ($\mu = 0.1$, 0.2 and 0.3 from bottom to top).

angular momentum to zero within the next time step, namely

$$F_{r_{max}} = \frac{2}{5} mR \cdot ((\hat{n} \times \hat{s}) \cdot \vec{\omega})/(\Delta t). \tag{3.13}$$

For the torque we therefore get

$$\tau = R \cdot \min(F_r, F_{r_{max}}). \tag{3.14}$$

As can already be seen from the definition of the rolling resistance, Eq. (3.11), the rolling resistance of small particles will be higher than for large particles which was also observed by studying one particle on a bumpy line [Ristow et al., 1994] and in experiments with glass marbles. To illustrate this fact, we show in Fig. 3.4 the dependency of the angle of repose on the rolling friction parameter r_0. The higher friction of smaller particles results in a steeper slope of the angle of repose in Fig. 3.4. An important result of this is that we can adjust the rolling friction in such a way that small and large glass beads have the same angle of repose as is seen in experiments for glass beads (Chapter 4 and [Zik et al., 1994]). Also one clearly sees that for small r_0 the slope of the angle of repose $\frac{\delta\Theta}{\delta r_0}$ is proportional to r_0, which result from the law of rolling resistance Eq. (3.11).

3.2 Brief comparison between Hooke and Hertz type contact laws

Even though detailed experiments for binary collisions of particles were performed, the force relations before and after a collision depend on the material and the asphericity of the particles [Foerster et al., 1994] and since these two quantities were not available for mustard seeds, we can only take the published values for glass.

In contrast to the Hertzian force, for the Hook like force the contact time and ϵ_{res} is collision-velocity independent and can be calculated analytically:

$$\epsilon_{res} = \exp\left[-\frac{\gamma_n(m_{\text{eff}}, r_{\text{eff}})}{2m_{\text{eff}}} t_c\right], \tag{3.15}$$

where t_c is the contact time of the two colliding particles:

$$t_c = \frac{\pi}{\sqrt{\frac{\tilde{Y}(m_{\text{eff}}, r_{\text{eff}})}{m_{\text{eff}}} - \left(\frac{\gamma_n(m_{\text{eff}}, r_{\text{eff}})}{2m_{\text{eff}}}\right)^2}}. \tag{3.16}$$

3.2.1 Binary collisions

To measure the collision properties, we plot the dimensionless final tangential velocity $\psi_f := \frac{v_s^f}{v_n^i}$ versus the initial tangential velocity $\psi_i := \frac{v_s^i}{v_n^i}$. The advantage of using these velocities is that they can be directly measured by experiments. Therefore to get a realistic behavior we are fitting our parameters to the experimental values for glass [Louge,

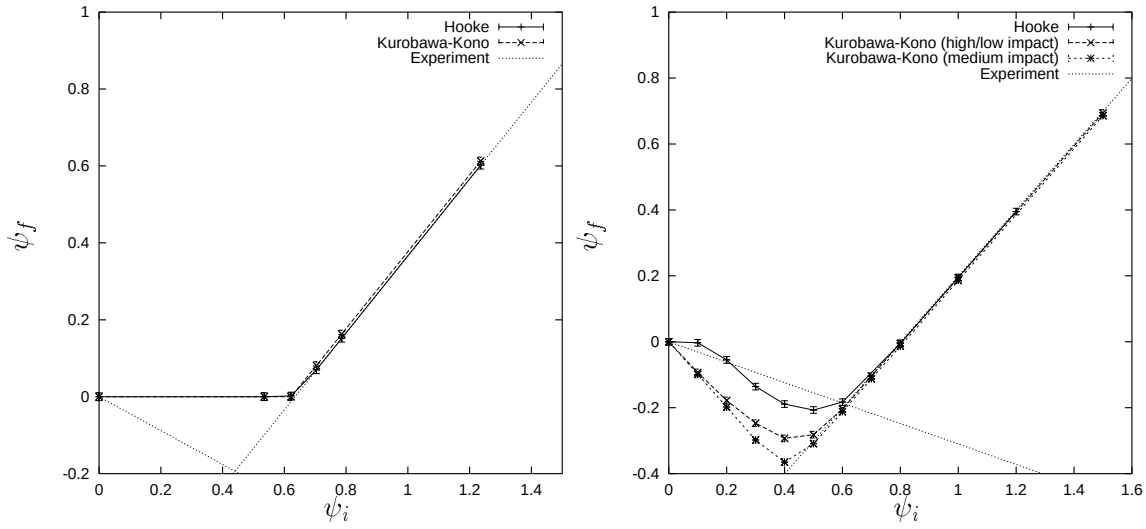

(a) particle-particle contacts

(b) particle-wall contacts

Figure 3.5: $\psi_f(\psi_i)$-graph for different force laws. The experimental data is denoted by the dotted lines. Note that for the Hertzian forces (laws (3.5) and (3.4)) the graph is velocity dependent!

1994; Schäfer et al., 1996] (Fig. 3.5; the dotted line is the experimental curve fitted to the theory). The coefficient of restitution in normal direction is directly measurable in experiments as well. For our force law (3.6) without rotation we just took the parameters for force law with rotation (3.3) and switched the rotation off. For force law (3.7) we adjusted our parameter to fit the experimental curve; here we had to *increase* friction to get the experimental curve which seems unphysical. So fitting non-rotating particles to the experimental $\psi_f(\psi_i)$ graph seems questionable and leads to wrong behavior for the macroscopic properties as we can see later on. This is intuitively visible, but this also illustrates the fact, that the $\psi_f(\psi_i)$ graph is not sufficient to characterize the full particle dynamics.

3.2.2 Flow properties

To compare the macroscopic behavior of the different force laws we are looking at the velocity profile and the energy distribution of the particles in the fluidized layer of the rotating drum.

Velocity profile

The velocity profile is taken in a four diameter wide band which goes through the drum center and is perpendicular to the free surface. In Fig.3.6(a) we see that the Hooke like

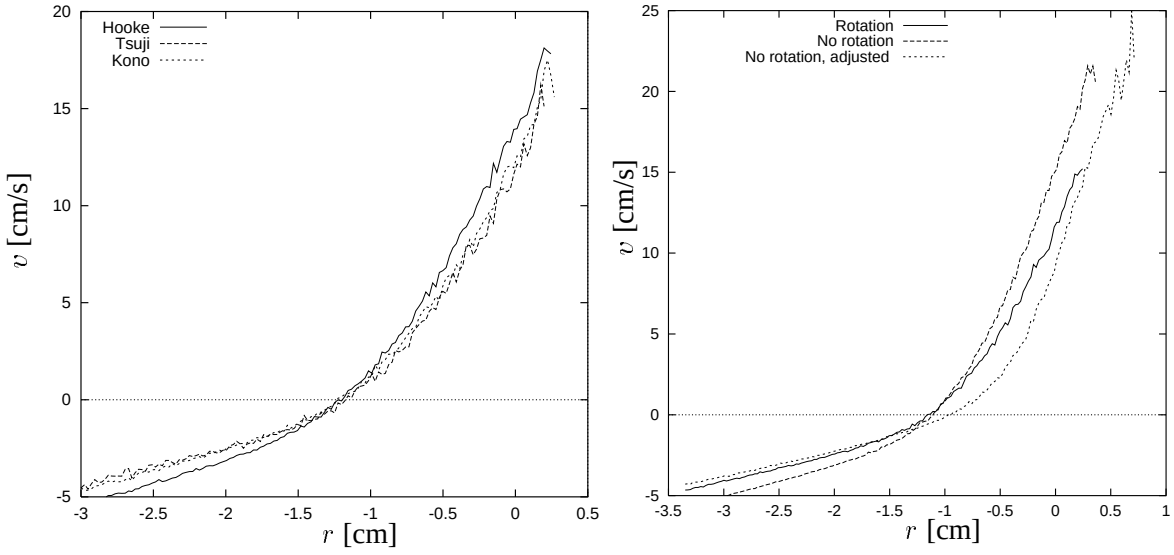

(a) Velocity profiles for the force laws with rotation (3.3)-(3.5) and $\Omega = 3$Hz.

(b) Velocity profiles for the force Hooke like laws (3.3), (3.6) and (3.7) with $\Omega = 2$Hz.

Figure 3.6: Velocity profiles for different force laws.

force law (3.6) tends to have a higher surface flow velocity and that the two Hertzian force laws (3.5) and (3.4) give nearly the same result. For lower angular velocities, $\Omega \leq 2$Hz, the profiles of force laws (3.5), (3.4) and (3.6) cannot be distinguished within the statistical error. The difference could be due to the fact that the $\psi_f(\psi_i)$-graph for the Hertzian forces are different for different impact velocities and for a higher angular velocity the $\psi_f(\psi_i)$-graph deviates more and more from the $\psi_f(\psi_i)$-graph of the Hooke like forces (see Fig. 3.5). However, the two different damping terms in the force laws (3.5) and (3.4) do not seem to deviate much. One reason for not observing differences could be due to the fact that for this investigations we only used particles of nearly one size.

Fig.3.6(b) shows the particle velocities for Hooke like forces with and without rotation. Both force laws without rotation (3.3) and (3.7) have the same slope in the fluidized regime $r \geq -0.5$ cm, but the velocity profile of the force law with rotation (3.3) and with switched off rotation (3.6) does not agree at all. At least the force law with adjusted parameters (3.7) agrees well with the plot for the rotational particles in the solid block, $r \leq -1.5$cm. Whereas the fluidized regime for the non rotational particles is much thicker than the fluidized regime for rotational particles. Also one observes that for particle rotations the solid block is smaller than without particle rotations and therefore particle rotations could support solid block slipping.

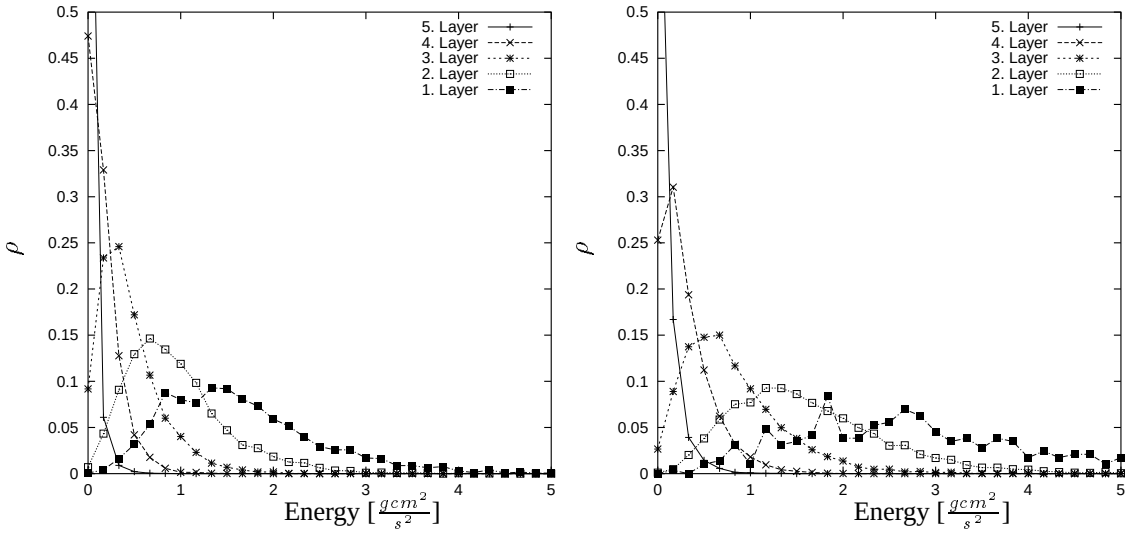

(a) Translational energy distribution ($\frac{1}{2}m\vec{v}^2$) in different shear layers for Hooke like force law (3.6) with rotation.

(b) Translational energy distribution ($\frac{1}{2}m\vec{v}^2$) in different shear layers for Hooke like force law (3.3) without rotation.

Figure 3.7: Translational energy distribution ($\frac{1}{2}m\vec{v}^2$) in different shear layers.

Energy distribution in the fluidized layer

The kinetic energy can be written as sum of the contribution from translational motion $E_T = \frac{1}{2}m\vec{v}^2$ and from rotational motion $E_R = \frac{1}{5}mr^2\vec{\omega}^2$. In Fig.3.7(a) we plot the translational energy distribution for the top 5 layers from the free surface; whereas the layer thickness is one particle diameter. The amount of translational energy in both cases is 100 times larger than the rotational energy; even though the rotational energy is only about one percent of the total kinetic energy, we saw in the velocity profiles that rotation is important and cannot be neglected. However, this does not mean that particles without rotation are useless, it only means that particles without rotation cannot be used to approximate particles with strong rotations. They still can be used to model particles where rotation is suppressed, i.e. mustard seeds; there they agree very well with the experiment (see Sec. 4.1.3). One thing to note is that even though the energy scales are different for translational and rotational energy, the energy distribution looks nearly identical (albeit on a different scale). Comparing the translational energy distribution in different shear layers for the Hooke like law with and without rotation (3.6) and (3.3) shown in Fig. 3.7 we see that for both force laws the distribution in the first three top layers follows a Weibull-distribution which turns to an exponential distribution from the fifth layer on, this can be seen as the transition from the fluidized layer to the solid block motion. Quantitatively the tail of the energy distribution without rotation is longer than for the distribution with rotation. This means that in the fluidized layer where particles cannot

rotate the maximum velocity is higher than in the rotational case. The reason for this is that the angle of repose is higher where we do not have rotations, so the particles have a higher potential energy which leads to a higher average velocity during the downward flow and therefore the maximum velocity is as well higher.

Result

We investigated the behavior of important macroscopic properties in a three dimensional rotating drum and their dependence on different force laws and the ability for the particles to rotate. For different damping terms in the Hetzian forces (3.5) and (3.4) we do not find any significant differences. Also different repulsive forces (3.4) and (3.6) do not seem to give very different results for low rotation speeds $\Omega \leq 2$Hz, albeit for large angular velocities, $\Omega \geq 3$Hz, they tend to differ more and more. A much more drastic effect is the ability for the particles to rotate. Particles without rotation must not be used for an approximation of rotating particles, but are still adequate to model particles where rotation is suppressed.

3.3 Short note on the computational implementation

The algorithm is stable for a time step of $\Delta t < \frac{t_c}{8}$; to be on the save side we choose the time step to be $\Delta t := \frac{t_c}{15}$. A more detailed analysis can be found in [Dury et al., 1998a].

3.3.1 Integration scheme

We took the Verlet algorithm as integration scheme for integrating our system [Allen and Tildesley, 1987]. This method is a direct solution of Newtons equation $\vec{F} = m\ddot{\vec{x}}(t)$ and is quite simple, only the present positions $\vec{x}(t)$, accelerations $\vec{a}(t)$ and the previous positions $\vec{x}(t - \Delta t)$ are needed (nine variables for each particle in 3D have to be stored). Taylor expanding about $\vec{x}(t)$ we get:

$$\vec{x}(t + \Delta t) = \vec{x}(t) + \Delta t\vec{v}(t) + \frac{1}{2}(\Delta t)^2 \vec{a}(t) \tag{3.17}$$

$$\vec{x}(t - \Delta t) = \vec{x}(t) - \Delta t\vec{v}(t) + \frac{1}{2}(\Delta t)^2 \vec{a}(t)\,, \tag{3.18}$$

adding both equation we get our integration scheme:

$$\vec{x}(t + \Delta t) = 2\vec{x}(t) - \vec{x}(t - \Delta t) + (\Delta t)^2 \vec{a}(t)\,. \tag{3.19}$$

The velocities can be obtained by subtracting the first two equation, when needed for obtaining $\vec{a}(t)$

$$\vec{v}(t) = \frac{\vec{x}(t + \Delta t) - \vec{x}(t - \Delta t)}{2\Delta t}\,. \tag{3.20}$$

Such a simple integration method is sufficient for our numerics, because of the very small time steps used (15 time steps per collision).

3.3.2 Neighboring list

The simplest method to check which particles collide, is just a loop for each particle over every particle and check the distance. Unfortunately, this will lead to an algorithm of the order $O(N^2)$ (with N as the number of particles) and is therefore unusable. For our small time steps we know that for the next time step the particle positions will only change slightly. So only particles can collide, which were in the neighborhood of an other particle the previous time step. Utilizing this, we need only to check the particles in the neighborhood; this can be done in two different ways:

1. Neighboring list: At the first time-step we build a list of all neighbors within a certain distant (skin) of a particle. After that we only need to check particles which are in the neighboring list for contact. But we still have to update the neighboring list once a particle outside the skin could collide with the particle. Thus we still haven an algorithm of $O(N^2)$, but the prefactor is much smaller (ca. 100 times), because we do not need to update the neighboring list every time step.

2. Linked cell algorithm: We put a grid onto the drum and sort each particle into a cell of the grid. For contact detecting we now only have to look in the cell and in the neighboring cells (9 in 2D and 27 in 3D) for colliding particles. This would be an algorithm of $O(N)$, but the grid generation and sorting of the particles takes much time, so the overall prefactor is large.

In our simulation, we combined these two methods: We used effectively a neighboring list, but the neighboring list itself was constructed with the linked cell algorithm. So our code scaled like $N^{1.3}$ with the particle number N.

3.3.3 Parallelization

The parallelization was done with the MPI-library. The natural way to parallelize this cylinder geometry, is to use a one dimensional domain decomposition scheme along the rotational axis. So essentially only neighboring processors have to communicate.

4 Angle of repose

The angle of repose is a very interesting quantity. First of all, because it can be observed easily and second, and more important, all the dynamics happens in the surface layer which depends on the other hand heavily on the angle of repose Θ (Fig. 4.1(a)). Due to the rotation of the drum material gets transported upwards and the angle between the free surface and the horizontal Θ increases, for angles higher than the a certain angle the pile becomes unstable (angle of marginal stability) and avalanches will detach to decrease the angle towards the static angle of repose, where no avalanches will occur. This avalanche mechanism will lead to a flow on the free surface and in this flow the main physics will happen.

4.1 The role of the angular velocity

The largest effect on the free surface and therefore also on the angle of repose has doubtless the angular velocity Ω. The upward transported material through the rotation in the cylinder is proportional to Ω and out of flux conservation also the downward flow. When the drum rotates, most particles can be viewed as being part of a solid block rotating upwards. On top of it, a fluidized layer is formed with downwards flowing particles. For a small angular velocity, Ω, there are distinct avalanches which are well separated, for increasing angular velocity, the avalanches follow each other more rapidly and finally exhibit a continuous downwards flow for a particular range of the angular velocity Ω; then we are speaking of the dynamic angle of repose. For even higher speeds, the particles are centrifuged to the drum wall.

4.1.1 Experiment

An acrylic cylinder of diameter 6.9 cm and length 49 cm was used. The material used was mustard seeds which are relatively round of average diameter about 2.5 mm, and have a coefficient of restitution, estimated from a set of impact experiments, of about 0.75 [Nakagawa et al., 1993]. A set of experiments were conducted to measure the angle of repose in different flow regimes.

Discrete avalanche regime

For a small rotation speed, Ω, intermittent flow led to a different angle before and after each avalanche occurred, called the starting (maximum) and stopping (minimum) angle, respectively. There seems to be a rather sharp transition from intermittent to continuous

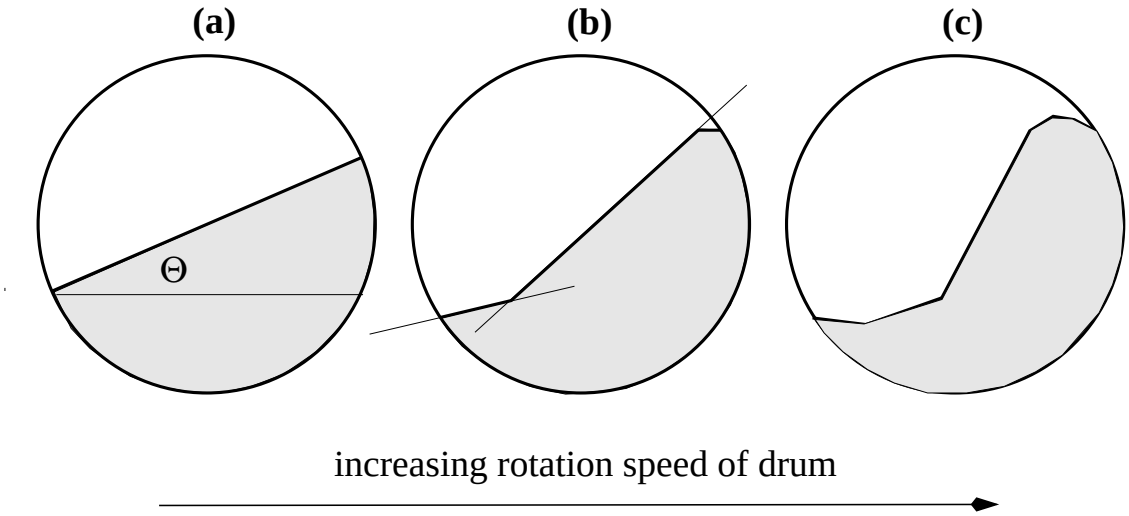

Figure 4.1: a) Flat surface for low rotation speeds, (b) deformed surface for medium rotation speeds with two straight lines added as approximation and (c) fully developed S-shaped surface for higher rotation speeds, taken from Dury et al. [1998c].

avalanches, which happens around $\Omega = 4$ rpm. For Ω greater than 4 rpm where the avalanches are continuous, the mustard seed data indicate a linear dependence of the dynamic angle of repose on the rotation speed which differs from the quadratic dependence found by Rajchenbach [1990].

Continuous regime

For a larger rotation speed these avalanches become a continuous flat surface and thus enables to define an angle of repose defined as the *dynamic angle of repose* as shown in Fig. 4.1(a). When Ω increases, the flat surface deforms with increasing rotation speeds and develops a so-called S-shape surface for higher rotation speeds, shown in Fig. 4.1(c). The deformation mostly starts from the lower boundary inwards and can be well approximated by two straight lines with different slopes close to this transition, sketched in Fig. 4.1(b). For all measurements in this regime, we took the slope of the line to the right which corresponds to the line with the higher slope.

We also investigated the dynamic angle of repose for different particle diameters and materials in the continuous regime in more detail using a 27 cm long acrylic cylinder of diameter $D = 6.9$ cm. For a given rotation speed, Ω, the dynamic angle of repose was measured four times at one of the acrylic end caps and the average value with an error bar corresponding to a confidence interval of 2σ, where σ is the standard deviation of the data points, was then calculated. First we used mustard seeds of two different diameters, namely 1.7 mm (black) and 2.5 mm (yellow), with a density of 1.3 g/cm^3. We varied the rotation speed, Ω, from 5 rpm to 40 rpm and took the higher angle in the S-shaped regime which exists for higher rotation rates, see Fig. 4.1(b). Both data sets are shown in Fig. 4.2(a) for black ($\bullet$) and yellow ($\circ$) seeds. The figure also illustrates the transition to

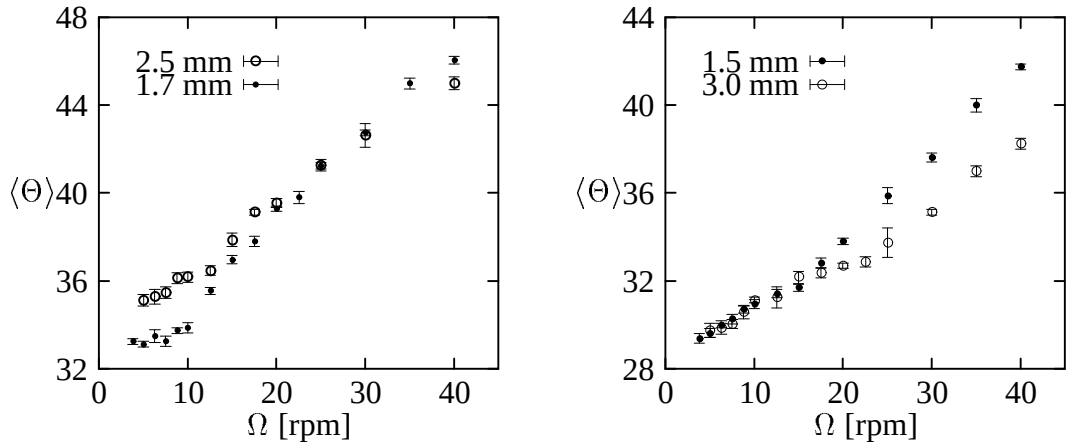

(a) Black (•) and yellow (○) mustard seeds.

(b) Small (•) and large (○) glass beads.

Figure 4.2: Experimental measured dynamic angle of repose.

the S-shaped regime which occurs at the change of slope, e.g. at around 11 rpm for the smaller seeds and around 16 rpm for the larger seeds. One also notes that the dynamic angle of repose is much higher for the larger particles in the low frequency regime. For values of $\Omega > 15$ rpm in the S-shaped regime, the difference in the dynamic angle of repose for the two different types of mustard seeds decreases with increasing Ω, and both curves cross around 30 rpm giving a slightly higher angle for the smaller seeds with the highest rotation speeds studied.

We applied the same measurements to two sets of glass beads having a density of 2.6 g/cm^3. The smaller beads had a diameter of 1.5 mm with no measurable size distribution, whereas the larger beads had a diameter range of 3.0 ± 0.2 mm. Both data sets are shown in Fig. 4.2(b) for small (•) and large (○) beads. It can be seen from this figure that the transition to the S-shaped regime occurs at around 16 rpm for the smaller beads and around 24 rpm for the larger beads. In general, we found that the small particles exhibit the S-shaped surface at lower values of Ω than the large particles. The angles of repose are, in general, lower for the glass beads compared to the mustard seeds which we attribute to the fact that the mustard seeds are not as round as the glass beads and rotations of the mustard seeds are therefore more suppressed. The coefficient of friction is also higher for mustard seeds.

There are two striking differences when comparing Figs. 4.2(b) (glass spheres) and 4.2(a) (mustard seeds). For rotation speeds, Ω, lower than 15 rpm, the small and large glass beads have the same dynamic angle of repose which agrees with the findings in Zik et al. [1994], whereas the dynamic angle of repose is significantly higher (3 to 4 degrees) for the larger mustard seeds compared to the smaller ones. For rotation speeds, Ω, higher than 15 rpm, the smaller glass beads show a higher dynamic angle of repose than the larger glass beads, and this angle difference increases with increasing rotation speed. For

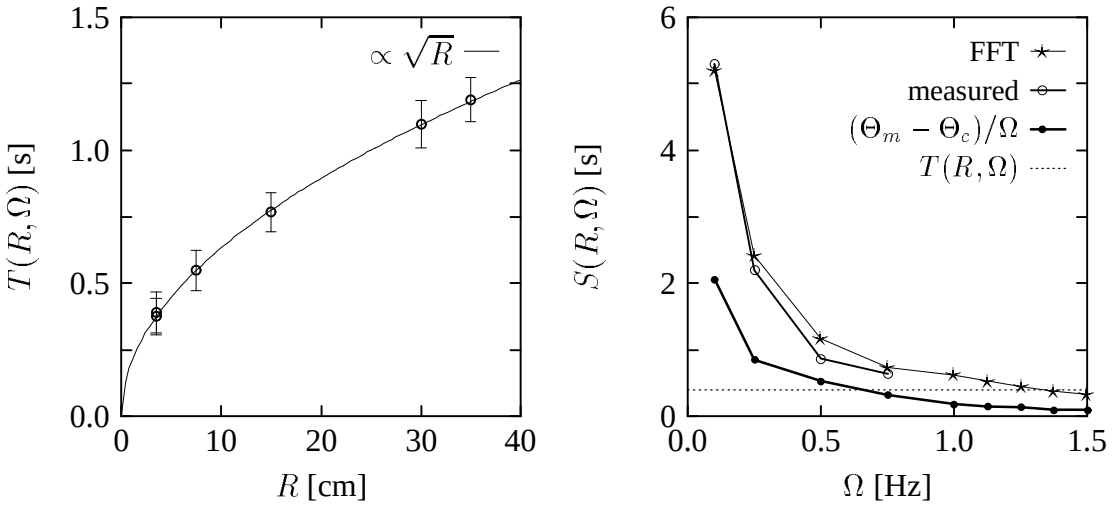

(a) Avalanche duration $T(R,\Omega)$ as function of the drum radius R.

(b) Avalanche separation $S(R,\Omega)$ as function of the angular velocity Ω.

Figure 4.3: Avalanche properties (simulation).

mustard seeds, the difference in the dynamic angle of repose between the smaller and the larger particles decreases with increasing Ω and the smaller seeds only show a higher angle for the highest rotation speeds studied. Both Fig. 4.2(a) and Fig. 4.2(b) seem to indicate that the increase in the dynamic angle of repose with rotation speed, Ω, in the S-shaped regime is larger for the smaller particles.

4.1.2 Simulation

The drum was half filled and the radius R was varied from 3.5 to 35 cm; 836 particles were used and the particle-particle restitution coefficient ϵ_{res} was set to 0.55 and μ to 0.6.

Discrete avalanche regime

For very low Ω, individual avalanches are clearly distinguishable, since the time between avalanches is large compared to the avalanche duration [Jaeger et al., 1996; Rajchenbach, 1990]. This gives all particles enough time to come to rest before the next avalanche. In our numerical simulation, avalanches were either detected and counted by measuring the time evolution of the surface angle or by looking at the kinetic energy of all particles. The latter technique resembles the avalanche detection by microphone used in the early experiments where each peak corresponds to an avalanche [Evesque and Rajchenbach, 1988]. But for higher rotation speeds, the peaks are not so distinct anymore and one has to look at the surface angle directly. This is done automatically in our simulations by either recording the center of mass of all grains or by performing a least square fit of the surface particles in the middle region of the drum. Even though the latter shows larger

fluctuations it gives a more accurate result for higher rotation speeds since wall boundary effects are more suppressed.

By measuring and counting avalanches in the Ω-range 0 ... 1 Hz, we find that the average avalanche duration $T(R,\Omega)$ is 0.4 s and in fact independent of Ω as proposed by using a continuum model [Bouchaud et al., 1995]. But $T(R,\Omega)$ depends on the drum radius R. For the parameters we use, the avalanche statistics are mostly dominated by large events, i.e. avalanches that transport particles over the whole length of the drum diameter. Looking at the energy balance of a single particle in such an avalanche, one finds that the average velocity of an avalanche scales as $\langle v \rangle \propto \sqrt{R}$. Since the particle has to travel a distance of $2R$ the duration of the avalanche scales with R as $T(R,\Omega) \propto \sqrt{R}$. This is shown in Fig. 4.3(a) for a system with 836 particles where R was varied from 3.5 ... 35 cm. The full line shows the theoretical $\sqrt{R}$ behavior and fits the data perfectly well.

Transitional Regime

When Ω increases, the average separation between avalanches $S(R,\Omega)$, measured from the end of an avalanche to the beginning of the next, decreases since the avalanche duration stays constant, see Fig. 4.3(b). For $S(R,\Omega) \approx T(R,\Omega)$, individual avalanches start to overlap which is visible in the kinetic energy as well as the surface angle. A transition takes place to the continuous flow regime and we sometimes see in the data for the surface angle time periods where discrete avalanches are visible that alternate with periods with rather small angle variations. In order to estimate the transition point Ω^*, one can measure $S(R,\Omega)$ directly which is only possible as long as $\Omega < \Omega^*$. Bouchaud et al. estimated that $T(R,\Omega^*) \approx (\Theta_m - \Theta_c)/\Omega^*$, where Θ_m stands for the angle of marginal stability and Θ_c for the angle of repose of the granular material [Bouchaud et al., 1995]. Taking for Θ_m (Θ_c) the average starting (stopping) angle of an avalanche, respectively, we find that the measured values for $S(R,\Omega)$ were underestimated by roughly a factor of two in the transitional regime using this relation. By performing a FFT on the time series of the surface angle $\Theta(t)$, we find that the time that corresponds to the position of the largest Fourier component overestimates $S(R,\Omega)$ only slightly. Any of these procedures can be used to get an estimate for the transition point Ω^* in a given setup and we show the different data in Fig. 4.3(b). The dotted line corresponds to the average avalanche duration of 0.4 s and from this graph we extract a value of $\Omega^* \approx 0.7 \ldots 1.2$ Hz using all three techniques. The transitional regime thus starts at Ω^* and ends around two times this value but the transition is not sharp.

Continuous flow regime

Above the transitional regime, distinct avalanches are no longer visible. The average surface angle fluctuates around its mean value with an amplitude which is significantly smaller than $(\Theta_m - \Theta_c)/2$ and increases with increasing Ω. We found that when d was increased (decreased) by 17% the average surface angle decreased (increased) by $1.1°$

($1.2°$) in the range $\Omega \approx 3 \ldots 6$ Hz. This is consistent with experimental findings and might be the triggering mechanism to start axial segregation in three dimensional rotating drums [Das Gupta et al., 1991; Hill and Kakalios, 1994] (see also Chapter 7).

We also observe that the surface angle depends on the restitution coefficient of the material, e.g. when ϵ_{res} is increased (decreased) by 0.2 the angle decreases (increases) by $5°$ (Fig. 6.5). When Ω increases, the average separation between avalanches $S(R, \Omega)$, measured from the end of an avalanche to the beginning of the next, decreases since the avalanche duration stays constant.

Centrifugal regime

When the rotation speed of the rotating drum increases more and more different other regimes are visible, such as the cateracting regime [Nityanand et al., 1986], but the last observable regime is characterized by the fact that all particles are driven against the container wall forming a ring. No avalanches or free flights of particles are present and since we included shear friction in our force laws at least the outermost ring of particles rotates around the drum center with the external rotation speed. At a characteristic rotation speed, which we will call Ω_z, single particles above the drum center detach from the ring and perform free flights until they hit again particles of the ring.

A careful analysis, which includes the friction between grains was presented by Walton and Braun [1993] and involves the angle of repose of the material. The expression for Ω_z reads

$$\Omega_z = \sqrt{\frac{g}{R \sin \Theta_c \sqrt{1-f}}}\,, \tag{4.1}$$

with f as the filling fraction of the drum and Θ_c as the stopping angle of an avalanche (static angle of repose). This dependence was verified numerically using the above described model and parameters for a half filled drum. The drum diameter was varied from 7 to 60 cm and the particle to drum diameter ratio was kept constant. Our numerical data for the frequency when the first particles detach from the outer particle ring are shown in Fig. 4.4 and are perfectly well fitted by the analytic expression given by equation (4.1) using $\Theta_c = 35°$ which is shown as solid line. The value of Θ_c is reasonable, since the angle of repose Θ_c for the mustard seeds is about the same magnitude ($32° - 36°$), see Fig. 4.2(a).

For frequencies slightly higher than Ω_z, we observe that the ring of particles does not rotate with a constant angular velocity but consists of rings rotating with decreasing angular velocity going inwards.

4.1.3 Theory

The numerical parameters were fine adjusted by comparing the experimentally determined dynamic angle of repose for 2.5 mm mustard seeds ($\rho = 1.3$ g/cm^3) with the

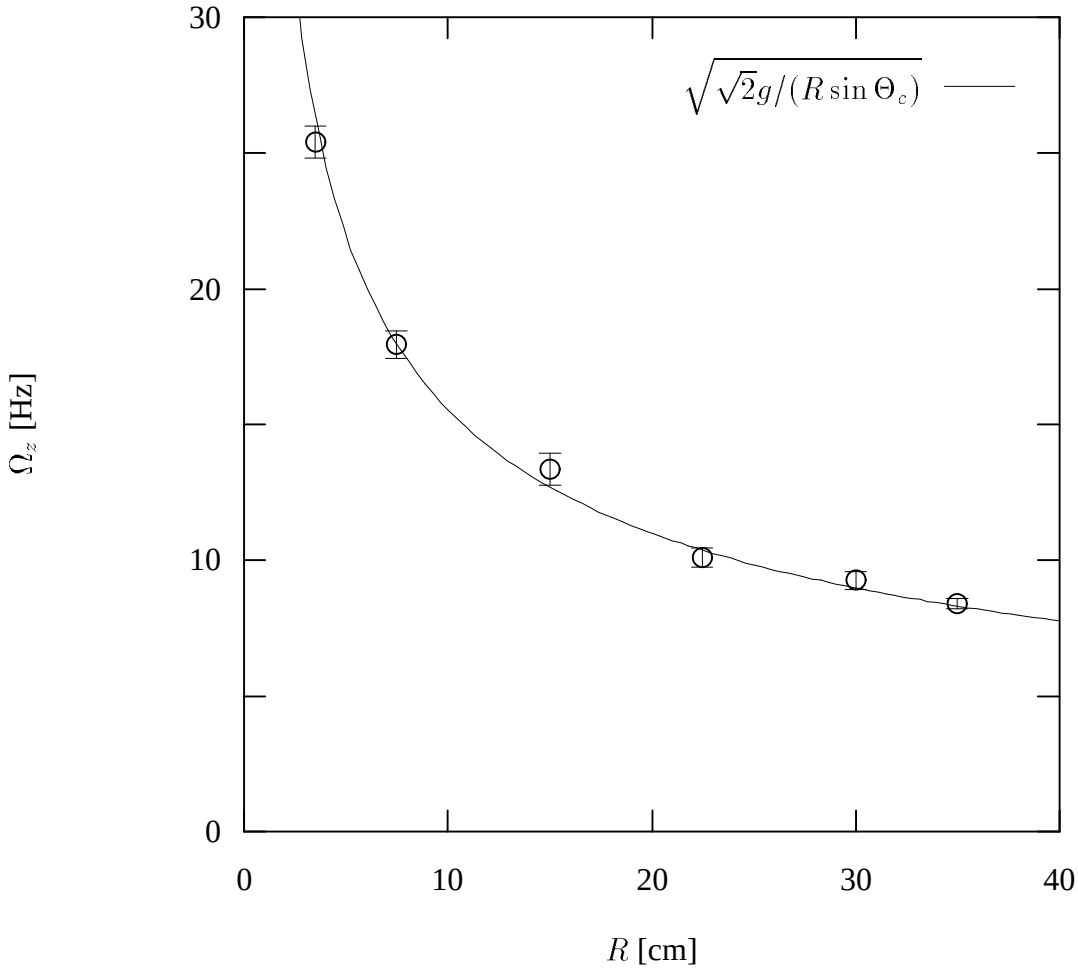

Figure 4.4: Transition frequency Ω_z to the centrifugal regime as function of drum radius R for a half filled drum.

simulation results over the Ω–range from 8 to 35 rpm. The radius of the drum was chosen as $R = 3.5$ cm. Both data sets are shown in Fig. 4.5. Also shown as a solid line in Fig. 4.5 is the theoretical result based on a model by Zik et al. [1994]. They started from the equilibrium condition for the surface flow j in a laminar and thin layer inclined with an angle Θ:

$$j = \frac{\rho g}{3\eta} h_0^3 \cos\Theta(\tan\Theta - \tan\Theta_0) \tag{4.2}$$

where ρ denotes the particle density, g gravity, η the constant viscosity and $\Theta_0 = \arctan\mu$. The cut-off depth, h_0, corresponds to a constant pressure value of $p_0 = h_0 g\cos\Theta$. A second expression for the surface flow in a half filled drum can be obtained by looking at mass conservation, [Rajchenbach, 1990]:

$$j = \rho\frac{\Omega}{2}(R^2 - r^2) \tag{4.3}$$

where r measures distance from the drum center along the free surface. Equating expressions (4.2) and (4.3) and using the relation $\tan\Theta = \frac{dy}{dx} = y'$, where $y(x)$ measures

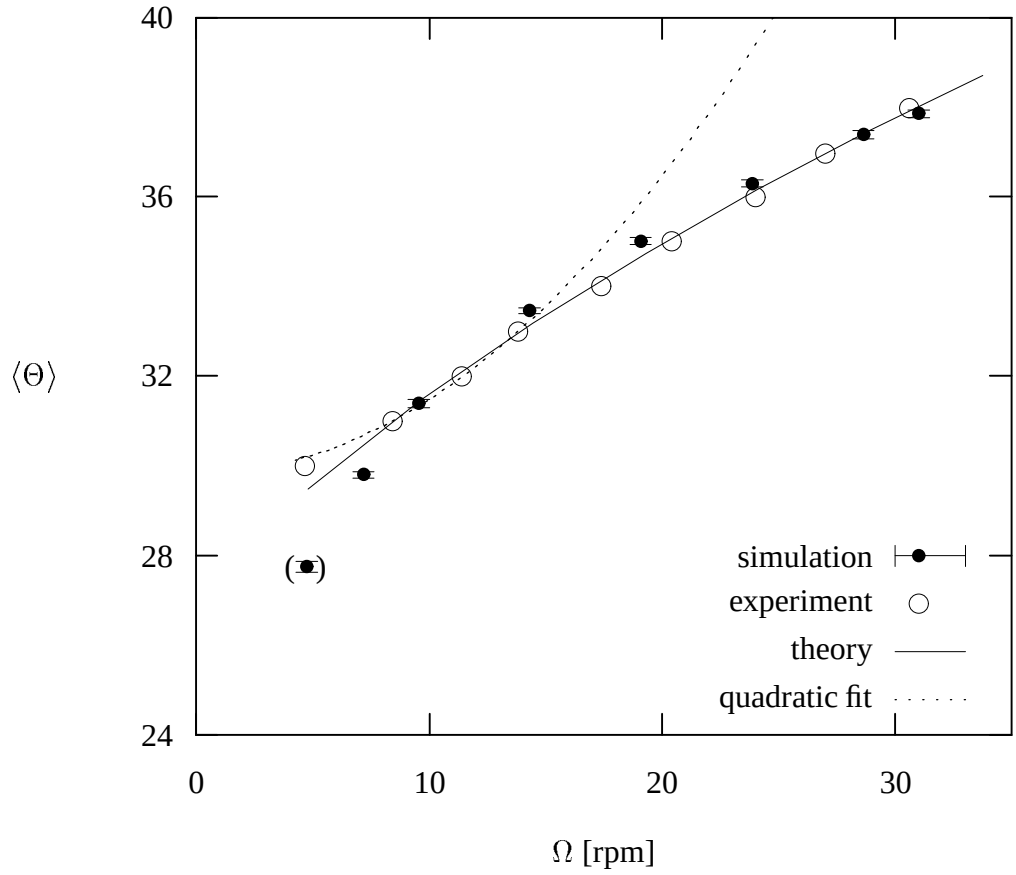

Figure 4.5: Comparison of dynamic angle of repose for large mustard seeds taken from MRI (○), numerical simulation (●) and the theory of Zik et al. [1994] (—).

the height of the top surface particle along the surface and $(\cos\Theta)^{-1} = \sqrt{1+(y')^2}$, we obtain

$$(y')^3 - (y')^2 \tan\Theta_0 + y' + c\,\Omega(y^2 + x^2 - R^2) = \tan\Theta_0 \tag{4.4}$$

with $c = \frac{3\eta g^2}{2\rho p_0^3}$. Corrections to this model were recently proposed by Khakhar et al. [1997b], but they lead to the same equations for the dynamic angle of repose as above in the case of a half filled drum due to the symmetry of the thickness of the fluidized layer for shear flow. Solving for y' at the origin (drum center), the only one of the three roots with no imaginary part reads

$$\tan\Theta = y' = \tilde{\mu} + (B + \sqrt{D})^{1/3} - \frac{1/3 - \tilde{\mu}}{(B + \sqrt{D})^{1/3}} \tag{4.5}$$

where $3\tilde{\mu} = \tan\Theta_0$,

$$B = \tilde{\mu}(1 + \tilde{\mu}^2) + \frac{1}{2} c\Omega R^2$$

and

$$D = 3\left(\tilde{\mu}^2 + \frac{1}{9}\right)^2 + \tilde{\mu}(1+\tilde{\mu}^2)c\Omega R^2 + \left(\frac{1}{2}c\Omega R^2\right)^2 .$$

We integrated Eq. (4.4) numerically and checked that the theoretical profile has a similar shape for different rotation speeds as the numerical data. We adjusted the parameter c using the experimental data points and the best fit was obtained for values of $c = 0.0111 \pm 0.0001$s/cm^2 and $\mu = 0.51(\Theta_0 = 27°)$. It is remarkable how well the theoretical curve fits the data points from the experiments and the numerical simulations, as shown in Fig. 4.5. The theoretical curve is very close to the arcus-tangent curve proposed by Hager et al. [1997]. For low rotation speeds, $\Omega < 8$ rpm, the experiment is very near the discrete avalanche regime, and therefore the simulations where we have used only dynamic friction for the particle-particle interactions and the theory where a steady flow is assumed tend to deviate slightly from the experiment. Rajchenbach experimentally found the relation $\Omega \sim |\Theta - \Theta_c|^m$ with $m = 0.5$ leading to $\Theta = \Theta_c + \alpha\Omega^2$ [Rajchenbach, 1990] which gives an increasing slope for increasing Ω in the graph, whereas the experimental data points in our Fig. 4.5 suggest a decreasing slope with increasing Ω. To illustrate this point further, we replotted all of our available experimental data points of the large mustard seeds measured at the end caps, taken from Fig. 4.2(a) above, in the same fashion as Rajchenbach and obtained a scaling exponent of m=0.87 using $\Theta_c = 34.1°$. This has to be compared with m=0.5 found by Rajchenbach and m=0.7 given by the numerical prediction by Tang and Bak [1988]. The Ω range of Rajchenbach is smaller than the one investigated by us and we speculate that his finding is valid close to the transition point to the continuous flow regime where the quadratic fit works rather well. We included this in Fig. 4.5 as dotted line using a best quadratic fit for the value of $\Omega < 20$ rpm.

Non-rotating particles

The simulations for Fig. 4.5 were done with non-rotating particles. The mustard seeds used in the experiment are elliptical and which is why rotations are somehow suppressed, therefore we are using particles without rotation to simulate them. Also we can calculate the angle of repose theoretically. As one can see the agreement of all three methods to obtain the angle of repose is perfect, only for small Ω the simulations lead to too small angles, because we used only dynamic friction for particle-particle contacts. The theory is in perfect agreement with the experiments (mustard seeds) and simulation (Hooke without rotation, because the ellipsoidal shape of the seeds suppresses the rotations in experiment), see Fig. 4.5. Unfortunately there are no experiments on the $\psi_f(\psi_i)$-graph (see Sec. 3.2.1) for the mustard seeds, so we had to use the angle of repose for validation of our simulation parameters.

4.1.4 Overall picture and comparison

After we have presented the different regimes in a rotating drum and discussed their dependence on R and Ω, we will present an overall picture and argue that it is universal.

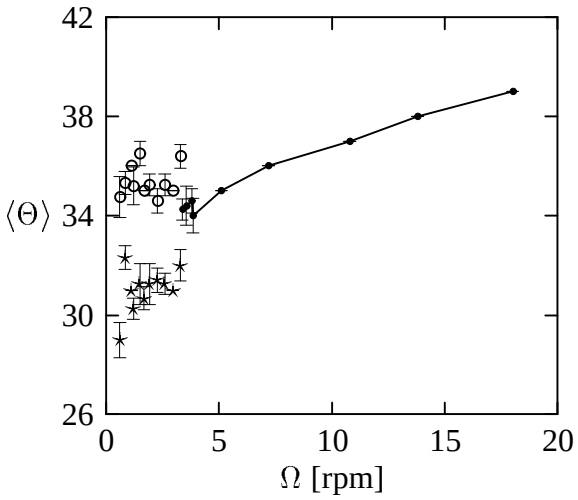

(a) Experimentally measured starting (∘) and stopping (⋆) angle and dynamic angle of repose (•) for mustard seeds [Nakagawa, 1997].

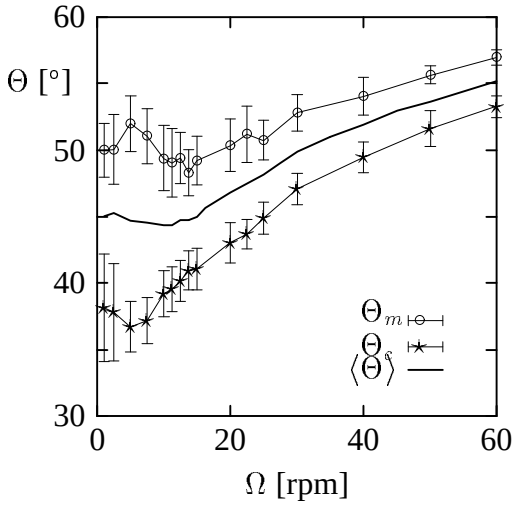

(b) Starting (stopping) angle Θ_m (Θ_c) in the rotating drum and their mean value (2D Simulation)

Figure 4.6: Starting and stopping angle in the rotating drum as function of external rotation speed Ω.

In Fig. 4.6(b), we show the average starting angle $\Theta_m(\circ)$ and stopping angle $\Theta_c(\star)$ for our system ($R = 3.5$ cm, $\alpha = 0.5$) in the Ω-range 0 ... 60 rpm. Also drawn as a thick solid line is the average $\langle\Theta\rangle$ of these two angles and the range goes up to $\Omega_z/4$ as defined by equation (4.1). In the discrete avalanche regime ($\Omega \approx 0 \ldots 10$ rpm), Θ_m and Θ_c stay nearly constant within the error-bars which is more visible by looking at $\langle\Theta\rangle$. In the transitional regime, a slight decrease of Θ_m with increasing Ω is observed. The depth of the minimum and the exact location of Ω^* can be varied by changing our parameters k_s and μ which also changes Θ_c.

The nearly constant value for $\langle\Theta\rangle$ in the discrete avalanche regime is also observed in the three-dimensional experiments (see Fig. 4.6(a)) where a drum with the same diameter was used. This was also reported by Hill and Kakalios [1994] and Cantelaube [1995] and they found in addition a minimum in the translational regime which corresponds to the one visible in our numerical data.

Regarding the dependence of the average surface angle on Ω in the continuous avalanche regime, Rajchenbach [1990] found a quadratic relation, $\langle\Theta\rangle \propto \Omega^2$, by measuring in the range $\Omega_z/111 \ldots \Omega_z/17$. Nakagawa finds a clear linear dependence in the range $\Omega_z/20 \ldots \Omega_z/9$ but the data points below that seem to have larger fluctuations and should be remeasured in order to find the corresponding regime. The data given by Das Gupta et al. [1991] ($\Omega_z/17 \ldots \Omega_z/4$) and Cantelaube [1995] ($\Omega_z/167 \ldots \Omega_z/10$) show for lower rotation speeds an increase in $\langle\Theta\rangle$ that scales like Ω^β with $1 < \beta < 2$, whereas a linear dependence is seen for larger rotation speeds. From the numerical data presented

in Fig. 4.6(b), one sees for $\Omega > \Omega^*$ that the average surface angle increases more than linearly with Ω and shows a cusp around $\Omega_z/8$ after which it depends linearly on Ω. The same type of change in slope around the same value of Ω/Ω_z is found in the data given by Das Gupta et al. [1991] but might be coincidental since we do not see a reason why the exact location of the cusp should be universal.

The experimental data given in Fig. 4.6(a) can be directly compared to the numerical results shown in Fig. 4.6(b). No quadratic dependence of Θ on Ω is found and the data points in the continuous regime ($\Omega > 5$ rpm) can be well fitted by a linear relation within the error bars.

After this discussion, we propose the following universal picture for the dependence of the surface angle in a rotating drum on the external rotation frequency: (i) for low rotation speeds, $\langle\Theta\rangle \approx$ const.; (ii) for $\Omega > \Omega^*$ one first finds $\langle\Theta\rangle \propto \Omega^\beta$ with $1 < \beta < 2$ and for higher values of Ω a dependence of $\langle\Theta\rangle \propto \Omega$; (iii) to compare different experiments and numerical simulations all Ω-values have to be rescaled by the transitional frequency to the centrifugal regime Ω_z which can be derived analytically, equation (4.1).

5 Boundary effects

5.1 Angle of repose again

All the angle of repose measurements presented in Chapter 4 were obtained by looking through one of the acrylic end caps in the experiments. In order to study the boundary effect of these end caps on the dynamic angle of repose, Magnetic Resonance Imaging (MRI) measurements can be performed. This technique of studying non-invasively the flow properties of granular materials was first used by Nakagawa et al. [1993] and is in addition explained in more detail by Nakagawa [1994] and Nakagawa et al. [1997a]. He used the large mustard seeds, with an average diameter of 2.5 mm. The dynamic angle of repose was measured based on the concentration data which was averaged in a thin cross-sectional slice in the middle of the cylinder far away from the end caps. This is shown in Fig. 5.1 as function of the rotation speed by the open circles ($\circ$). Restricting the measurement to the flat surface regime, we see that all data points then lie approximately on a straight line. On the other hand, non-MRI data were measured at the end caps and are shown as stars ($\star$) in Fig. 5.1. The consistently higher dynamic angle of repose at the end cap indicates the significance of the friction between particles and the boundary wall. We also found that the S-shape regime seems to start earlier at the end caps due to the additional wall friction.

For particle–particle collisions we use $\mu = 0.2$, and for particle–wall collisions, $\mu_w = 0.4$. In order to save computer time, we set $\tilde{Y}$ to $6 \cdot 10^4$ Pa m which is about one order of magnitude softer than vulcanite but the maximal overlap of two particles is at most 0.3% of the sum of their radii, which is still realistic. This gives a contact time during collisions of $1.1 \cdot 10^{-4}$ s. The coefficient of restitution for wall collisions is set to $\epsilon_{\text{res}} = 0.77$ which is within the error bar of the experimentally measured value of $\epsilon_{\text{res}} = 0.75$. In experiments with spherical liquid-filled particles, we found only a weak dependence of the restitution coefficient on particle size and therefore used a normal force law, Eq. (3.3), that would make the restitution coefficient independent of particle size. When the same type of force law is applied to particle-particle collisions, it gives a normal restitution coefficient of $\epsilon_{\text{res}} = 0.56$.

5.2 Boundary effect on surface angle

As shown in Fig. 5.1, the dynamic angle of repose of granular material in a rotating drum is significantly higher at the end caps than in the middle. For the experimentally investigated particle sizes of the order of millimeter, the effect was visible up to a few

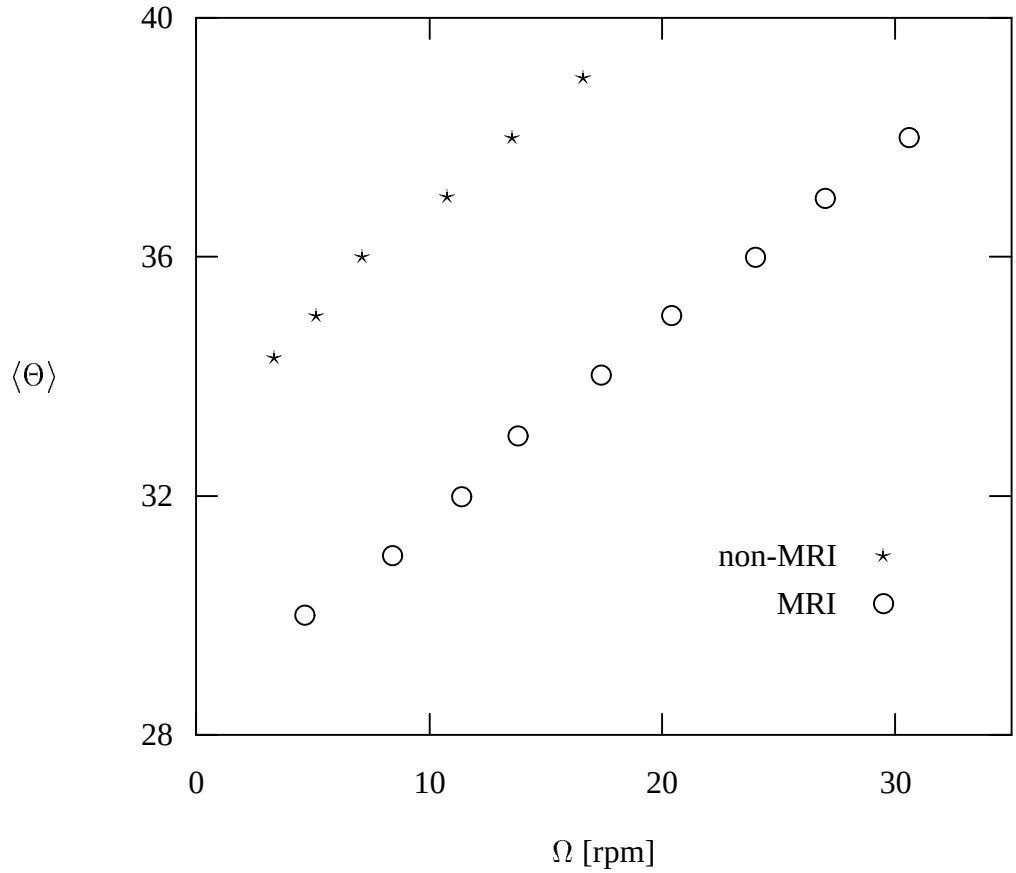

Figure 5.1: Comparison of dynamic angle of repose for large mustard seeds taken from MRI (○) and non-MRI (⋆) measurements [Nakagawa, 1997].

centimeters. But this length scale might depend on the particle diameter and density and also on external parameters like gravity.

Using the above described technique, we simulated extended three-dimensional, half-filled drums. For a particle size of 2.5 mm and a rotation speed of 20 rpm, the time-averaged angle, denoted by $\langle\Theta(z)\rangle$, as function of the position along the rotation axis is shown in Fig. 5.2. Each point with corresponding error bar stands for a weighted average over the nearest neighbors. In order to study the characteristic length, ζ, of the boundary effect, we fit all data points by the relation

$$\langle\Theta(z)\rangle = \Theta_\infty + \Delta\Theta\left(e^{-z/\zeta} + e^{-(L-z)/\zeta}\right) \tag{5.1}$$

where L stands for the length of the drum, Θ_∞ for the dynamic angle of repose far away from the boundaries and $\Delta\Theta$ for the angle difference between the value at the boundary and Θ_∞. For the curve shown in Fig. 5.2, the corresponding values are $\Delta\Theta \approx 4°$, which is the same value given in Fig. 5.1 for the MRI experiment, $\zeta = 3.19 \pm 0.25$cm, $L = 20.6$ cm and $\Theta_\infty = 35° \pm 0.2°$. We tested Eq. (5.1) against the simulation results for different drum lengths of $L/2$, $L/4$ and $L/8$ and found a remarkably good agreement. In the

last two cases, the value for Θ_∞ is never reached in the middle of the drum due to the boundary effects.

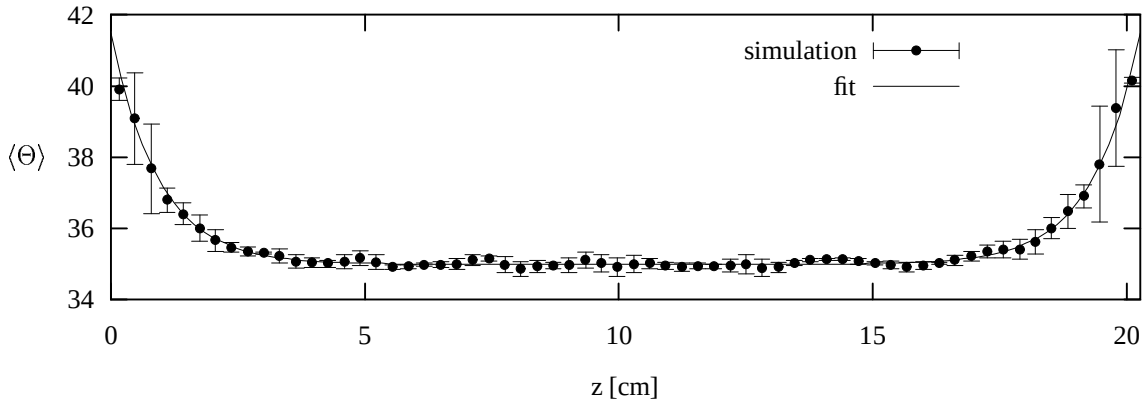

Figure 5.2: Profile of the dynamic angle of repose along the rotation axis for 2.5 mm spheres: (•) simulation, (—) fit ($\Omega = 20$rpm).

Using drums that are at least 64 particle diameters long, we studied the dependence of Θ_∞ (middle) and the angle at the end caps on the particle diameter d at the same rotation speed of 20 rpm. The simulation values in the tangential direction were chosen in such a way that the normalized tangential velocities before and after impact were *independent* of the particle diameter d. The ration $\tilde{Y}/k_s$ was set to 3.1, a value which gives for acetate spheres a good agreement of simulations [Schäfer et al., 1996] and experiments [Foerster et al., 1994] (see Chapter 3). The value of γ_s was chosen sufficiently high to give a similar behavior in particle-particle- and particle-wall-collisions in the sliding regime. The results for the surface angle along the rotation axis are shown in Fig. 5.3, which illustrates that the angle increases with increasing particle size in agreement with the mustard seed experimental results given in Fig. 4.2(a). The angle difference of around 4 degrees, which seems to be independent of the particle size, also agrees with the experimental findings. In other experiments, different dependencies were observed: Das Gupta et al. [1991] mostly found a higher angle for smaller particles using sand grains and Hill and Kakalios [1994] measured higher angles for smaller particles when using sand and glass particles although it was also possible to get no angle difference for certain size ratios of glass spheres. The latter was also found by Zik et al. [1994], whereas Cantelaube [1995] did not find a clear trend when using discs in a quasi two-dimensional drum. What causes the different behavior is not clear at the moment and a more detailed analysis would be desirable but is beyond the scope of this chapter. It is necessary to use appropriate values for the simulation parameters to quantitatively model a desired system, which is why we gathered as much information for the mustard seeds as possible. A arcus-tangent fit which gave a smaller mean deviation than a parabolic fit was added to Fig. 5.3 to guide

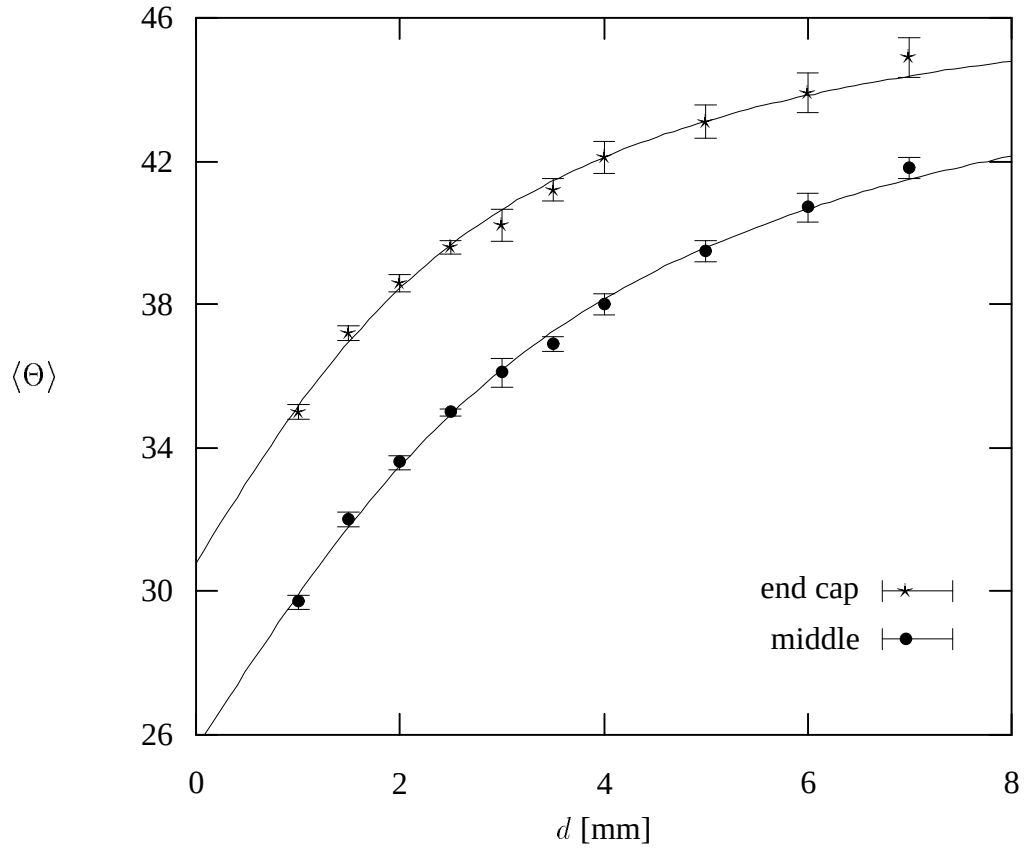

Figure 5.3: Dynamic angle of repose as function of sphere diameter for $\Omega = 20$ rpm (simulation); ($\star$) end cap, ($\bullet$) drum middle, (—) arcus-tangent fit.

the eye. Changing the density, ρ, of the particles or the gravitational constant, g, has a dramatic effect on the angle of repose: for the latter quantity this is shown in table 5.1 and a similar behavior was seen in recent experiments [Peralta-Fabi et al., 1997]. For both ρ and g, an increase in value corresponds to an angle decrease. When a hydrostatic pressure, $p_0 \sim g$, is assumed, the data for $g < 30$ m/s^2 can be well described by Eq. (4.5). The lower g becomes the more pronounced the S-shaped surface becomes, and in the limit $g \to 0$, the transition to the centrifugal regime takes place at (see Eq. (4.1))

$$\Omega_c \approx \sqrt{\frac{\sqrt{2}\, g}{R \sin \Theta_0}}$$

where Θ_0 denotes the average angle in the limit $\Omega \to 0$ [Walton and Braun, 1993; Dury et al., 1997]. In our case, for $\Omega = 20$ rpm the transition to the centrifugal regime occurs at $g \approx 0.45$ m/s^2, which is in perfect agreement with the numerical findings. Even though we studied more than one (two) orders of magnitude in ρ (g), we could not obtain an accurate infinite value limit.

g [m/s^2]	1.62	3.73	9.81	13.6	25.1	274
Θ [°]	48.2	41.4	35.0	33.3	30.2	18.4
ζ/R	0.291	0.274	0.277	0.269	0.283	0.260

Table 5.1: Angle of repose, Θ, in the drum middle and dimensionless characteristic length, ζ/R, as function of gravity, g (simulation).

5.2.1 Range of boundary effect

In order to study the range of the boundary effect, we extracted figures similar to Fig. 5.2 from our simulations and varied the drum length, L, and radius, R, the particle diameter, d, and density, ρ, the gravitational constant, g, and the rotation speed, Ω. The data points for the dynamic angle of repose as a function of position along the rotation axis were fitted by Eq. (5.1) giving the characteristic length, ζ, of this run. As expected, ζ did not vary when the length of the drum or the rotation speed was changed, but surprisingly, the characteristic length, ζ, did not change when the density of the particles or the gravitational constant was changed by more than one order of magnitude, even though the dynamic angle of repose strongly depends on both as shown in table 5.1 for the latter quantity.

Based on the definition of ζ in Eq. (5.1), one might speculate that $\zeta \sim R$ since the gradient of the slope along the rotational axis of the surface should be a material property, i.e. it should not depend on the geometry. The angle of repose is independent of the drum radius, R, and therefore the height difference between the surface at the end cap and the surface in the middle of the drum must be proportional to R. This leads to $\zeta \sim R$ which is indeed the case, and we show in Fig. 5.4 the dimensionless characteristic length, ζ/R, as function of dimensionless particle diameter, d/R, for three different drum radii. Below a critical diameter, d_c, ζ seems to be independent of the particle size, and we propose the following relation

$$\zeta = \begin{cases} \alpha\, R & \text{, if } d \le d_c \\ \alpha\, R + \beta(d - d_c) & \text{, if } d > d_c \end{cases} \tag{5.2}$$

where, in our case, $\alpha = 0.28$ and $\beta = 3.13$. The critical particle diameter $d_c \approx 0.14\, R$ and it seems to decrease slightly with increasing drum radius. Therefore, particles in the fluidized zone with $d < d_c$ might be describable by a continuum model. For particles with $d > d_c$, we have to take finite size effects into account.

5.2.2 Results

We have investigated the dynamic angle of repose, Θ, in a three-dimensional rotating drum in the continuous flow regime. By choosing different materials and particle diameters, we discussed the Ω-dependence of Θ for glass beads and mustard seeds of two different sizes. In the low rotation speed regime, both types of glass beads showed the

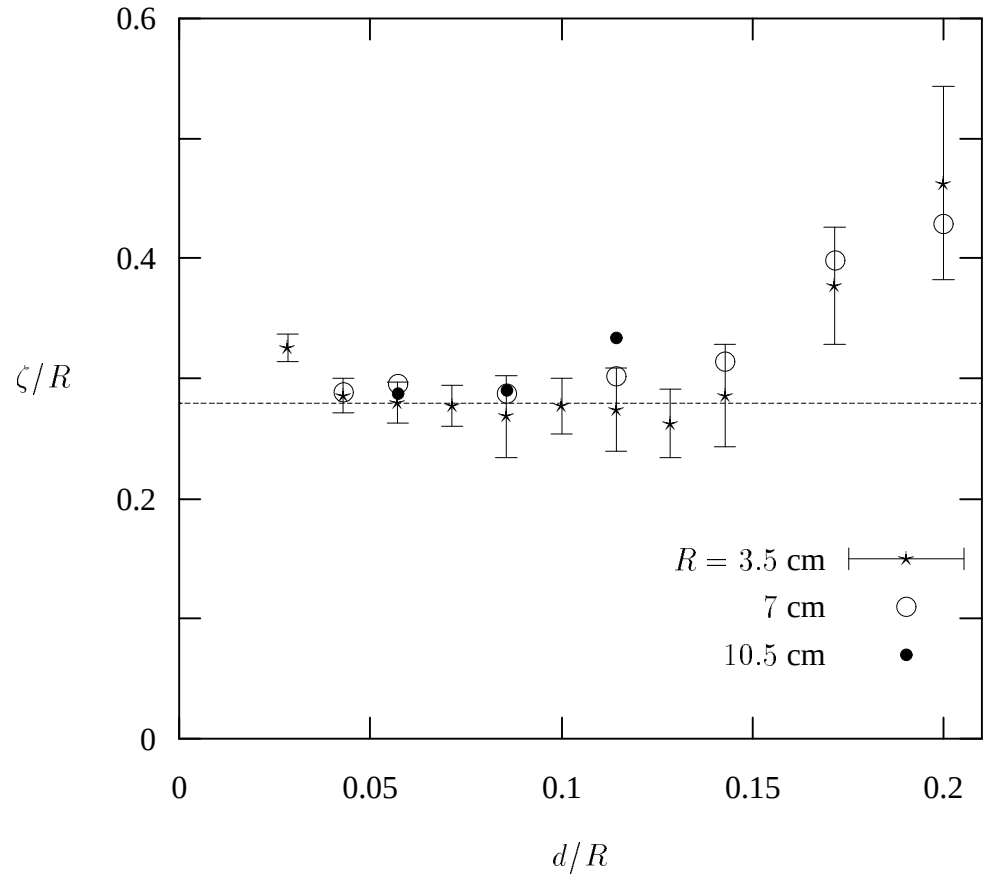

Figure 5.4: Dimensionless range of boundary effect for spheres with different diameter; ($\star$) $R = 3.5$ cm, ($\circ$) $R = 7$ cm, ($\bullet$) $R = 10.5$ cm, dotted line shows value $\zeta = 0.28\,R$ for radius-independent regime (simulation).

same angle of repose, whereas the angle was higher for the *larger* mustard seeds. Using MRI techniques, we could quantify, for the large mustard seeds, the angle difference between the middle and the end of the drum and its Ω-dependence. In all cases, either a linear or an arcus-tangent dependence of Θ on Ω was found. In order to investigate the range, ζ, of the boundary effects, we used a three-dimensional *discrete element* code and fitted the averaged angle along the rotation axis to two exponentially decaying functions. We found that ζ scales linearly with the drum radius. On the other hand, it does not depend either on the particle density or the gravitational constant, even though the surface angle changes drastically with these quantities, or on the rotation speed of the drum. A detailed analysis of the dependence of the characteristic length, ζ, on the particle diameter, d, revealed that ζ is independent of d for small particle diameters but shows finite size effects for larger d.

6 Radial segregation

Radial segregation in rotating drums takes place on very short time scales [Donald and Roseman, 1962]. Usually the drum is roughly about half filled and rotated along the cylinder axis. This was studied experimentally and numerically for varying size ratios [Clément et al., 1995; Cantelaube and Bideau, 1995; Baumann et al., 1995; Hill et al., 1997a] and density ratios [Ristow, 1994b; Metcalfe and Shattuck, 1996; Khakhar et al., 1997a]. Also the amount and direction of segregation depends on the rotation rate [Nityanand et al., 1986]. As pointed out in Chapter 4, there are different flowing regimes depending on the angular velocity Ω. In the case where we have size segregation, the segregational behavior will also change in the different regimes. In the continuous flow regime smaller particles will tend to segregate into the core near the rotational axis, whereas for higher speeds near the centrifugal regime, the small particles tend to gather at the cylinder boundary [Nityanand et al., 1986]. For the rest of this thesis we will restrict our investigations to the continuous flow regime.

The kinematics of the segregation happens only in the shear flow along the surface, in there the small particles percolate through the larger ones in the flow and get trapped by the solid block before they can reach the cylinder wall. Due to the continuous solid block rotation, a core of small particles at the center of the drum below the surface flow is formed, this is commonly referred to as *radial segregation*. Also in two-dimensional systems, this was well observed experimentally [Clément et al., 1995; Cantelaube and Bideau, 1995]. Using discrete element simulation (Chapter 3) an order parameter will be defined that allows to quantify the amount of segregation and it is used to compare the segregation speed and the final amount of segregation for different systems and materials directly.

Another point which has been observed is that depending on the filling ratio there is also geometrical mixing [Metcalfe et al., 1995]. This mixing compete with the radial segregation and is investigated in Sec. 6.2.2.

6.1 Order parameter

To compare the quality and speed of the segregation of different runs with different parameters, it is desirable to have only one order parameter in order to compare all of these. For this we divide the cylinder with diameter D into n concentric hollow cylinders with thickness $\Delta = \frac{D}{2n}$ and measure the number density of the smaller particles, ρ_i, in each

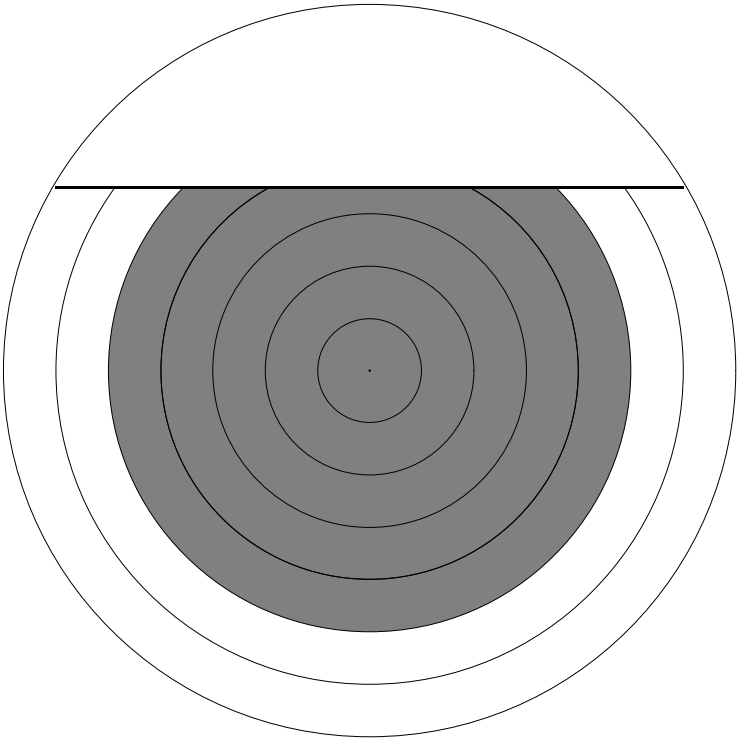

Figure 6.1: Schematic cross section through a more than half–filled cylinder.

hollow cylinder $i = 1, \ldots, n$ (see Fig. 6.1). We choose as such an order parameter q the sum over all positive deviations $\Delta\rho_i$ of ρ_i above the mean number density

$$\rho_0 = (\text{Number of small particles})/(f V_{\text{drum}}) \tag{6.1}$$
$$\text{with } V_{\text{drum}} = L\pi(D/2)^2 \quad \left(\pi(D/2)^2 \text{ ; in 2D}\right)$$

in a cylinder with a filling fraction f, normalized with respect to the ideally segregated case, where all inner cylinders $i = 1, \ldots, c$ are composed only out of small particles shown in grey in Fig. 6.1 and all the outer cylinders $i = c+1, \ldots, n$ are composed only out of large particles. To illustrate this procedure, we show in Fig. 6.2(a) (where we used eleven concentric shells) the packing fraction of small ($\diamond$) and large ($+$) particles in each cylinder for a volume filling fraction of 66.4%. The volume filling fraction is defined as the ratio of the volume occupied by the granular material to the cylinder volume, reading $f = \frac{V_{\text{occupied}}}{V_{\text{drum}}}$, where the occupied volume depends on the packing fraction η via $V_{\text{occupied}} = \frac{1}{\eta}\sum_{\text{all particles}} \frac{4}{3}r^3\pi$. Hence the packing fraction η is determined by

$$\eta = \frac{\sum_{\text{all particles}} \frac{4}{3}r^3\pi}{f \cdot V_{\text{drum}}} \quad ;$$

i.e. filling the drum with a certain filling fraction and summing up the volumes of each particle. We found that this packing fraction η does not change significantly with the amount of achieved segregation, but certainly with the size ratio of the particles (shown

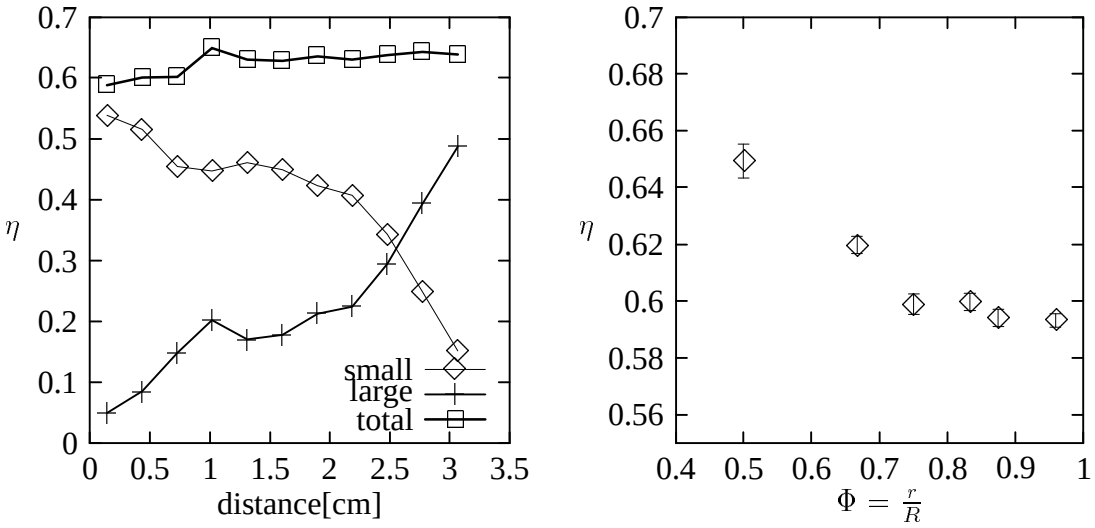

(a) Volume fraction in each cylinder for a volume filling fraction of 66.4% (3D-simulation

(b) Packing fraction of the granular mixture for different size ratios Φ.

Figure 6.2: Volume fraction of small and large particles. (3D-simulation).

in Fig. 6.2(b)). The packing fraction changes from $\eta = 0.59$ for a size ratio near to one, to $\eta = 0.65$ for a size ratio of $\Phi = \frac{1}{2}$, i.e. for $\Phi \approx 1$ we get the packing fraction of a random packed unary mixture and for small size ratios η increases until the smaller particles fit completely into the voids of the large particles, which we could not show, because of the huge demand on CPU-time for systems with small size ratios and therefore only size ratios down to $\Phi = \frac{1}{2}$ were observed.

For Fig. 6.2(a) the particle size ratio of small and large particles $\Phi := \frac{r}{R}$ was $\Phi = 0.5$ and the cylinder was rotated for $2\frac{1}{2}$ revolutions which gives a nearly complete radial segregation, which can be seen in Fig. 6.2(a) by the vanishing packing fraction of the large particles near the drum center. The small particles, denoted by $\diamond$, are mostly found in the middle of the cylinder, whereas the large particles, denoted by $+$, show a higher concentration in the outer cylinders. Also shown is the total volume occupied by all spheres, denoted by $\square$, which gives an average value in each cylinders of $\eta = 0.63$ which is close to the value for a random particle packing $\eta = 0.59$.

6.1.1 Density profile

A better quantity to evaluate than the packing fraction is the number density of (small) particles. To obtain the density profile for small particles we divide the disc segment into concentric shells with width Δ and inner radius $R_i = (i-1)\cdot\Delta$ of shell i. To quantify the quality of the segregation we normalize the measured density by dividing by $\rho_S = \frac{\eta}{\pi\frac{4}{3}r_s^3}$ ($\rho_S = \frac{\eta}{\pi r_s^2}$; 2D) which is the theoretical density if only small particles were present. The

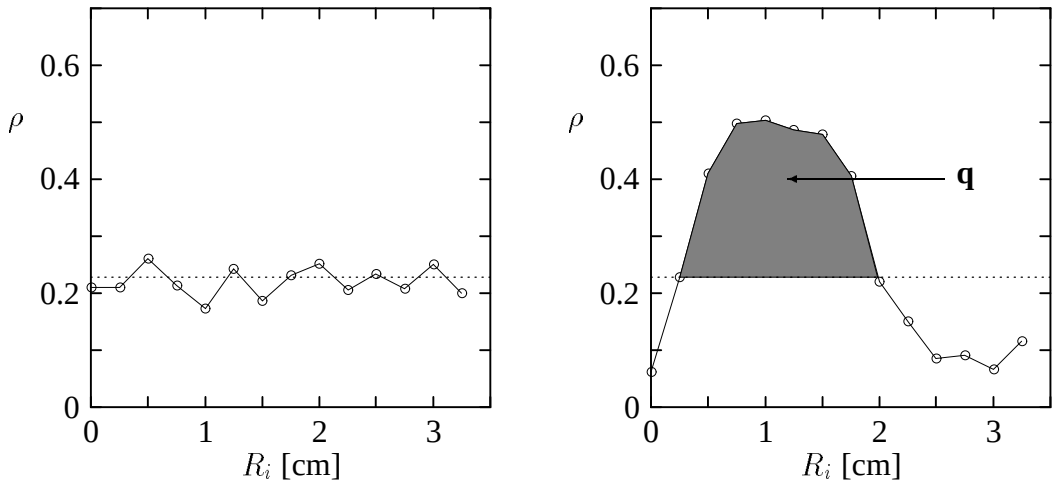

(a) Mixed state (b) Segregated state, giving $q = 0.39$

Figure 6.3: Density profiles. The dotted line denotes the density for the unsegregated case ρ_0.

probability density $\rho_\Delta(R_i)$ is thus defined as:

$$\rho_\Delta(R_i) := \frac{1}{\rho_S} n_\Delta(R_i) \,. \tag{6.2}$$

Here $n_\Delta(R_i)$ is the number of small particles in shell i with width Δ divided by the volume $V = \frac{1}{2}\left[(R_i+\Delta)^2 - R_i^2\right]\pi L$ $\left(A = \frac{1}{2}\left[(R_i+\Delta)^2 - R_i^2\right]\pi \text{ ; in 2D}\right)$ of shell i. $\rho_\Delta(R_i)$ ranges from 0 to 1 and in the unsegregated case the probability density is in all shells ρ_0/ρ_S which gives for our values $\rho_0 = 0.228$ as defined in Eq. (6.1). In Fig.6.3(a) we show the density profile for the unsegregated case where the dotted line denotes ρ_0. The density profile fluctuates around ρ_0 as expected. In Fig.6.3(b) the density profile for a well segregated case is given, here one can clearly see the segregated core of the small black particles where the value of ρ is approximately 0.5 . On top of the core, $R_i < 0.25$cm, we can see the fluidized layer composed of large and small particles. The probability density for our segregated configuration cannot reach the maximum possible value of one, because the segregated core of small particles is not really a half disk and on top of it there is always a fluidized zone which is composed also out of large particles. Therefore the maximum realistic possible value for ρ is about 0.7 . Further away from the center of the drum, $R_i \geq 2$cm, the density of the small particles is below the value of the unsegregated case and even drops to less than $\rho_0/2$ for $R_i = 3$cm. In this region the larger particles concentrate.

6.1.2 Calculation of q

To illustrate this procedure of constructing an appropriate order parameter q, we have shaded the area that enters our calculations in Fig.6.3(b). In the ideally segregated case

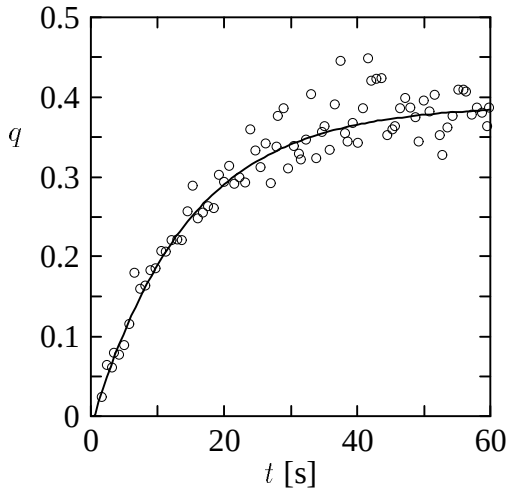

(a) For $\Omega = 0.75$ Hz. The solid line is the fitted curve with $q_\infty = 0.395$ and $\tau = 15.4$s.

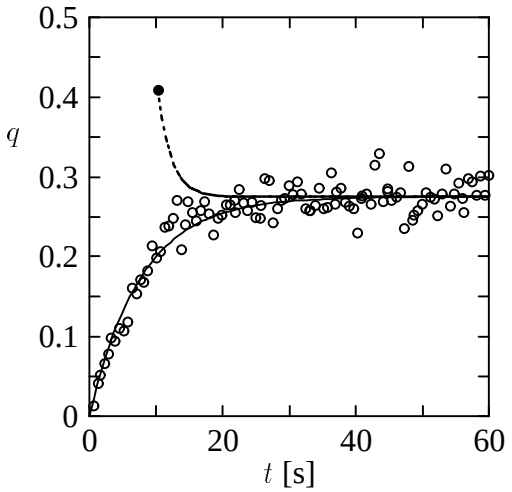

(b) For $\Omega = 2.5$ Hz. The solid line is the fitted curve with $q_\infty = 0.275$ and $\tau = 7.7$ s and the dotted line is the time evolution of a more segregated initial configuration.

Figure 6.4: Time evolution of our order parameter $q(t)$.

the inner half disk has radius of R_c $\left(\text{for an half filled drum } R_c = r_s\sqrt{\frac{2N}{\pi\rho_S}}\right)$. Cast into a formula, we define our order parameter q as:

$$q := \frac{1}{c_n}\sum_{i=0}^{\frac{R_c}{\Delta}-1}\left(\rho_\Delta(R_i)-\rho_0\right)\Theta\left(\rho_\Delta(R_i)-\rho_0\right)\ , \tag{6.3}$$

with $\Theta(x)$ as the Heaviside Step function. For calculating the normalization constant c_n we choose for convenience the width of the shells Δ to be an integer fraction of the drum radius $D/2$ and of R_c. So we get for the probability density in the ideally segregated case $\rho_{S\,\Delta}(R_i) = \Theta(R_c - R_i)$ and the normalization constant c_n is:

$$c_n := \sum_{i=0}^{\frac{R}{\Delta}}(1-\rho_0)\Theta(R_c-R_i) = (1-\rho_0)\frac{R_c}{\Delta} = \left(1-\frac{r_s^2}{R^2}\frac{2fN}{\eta}\right)\frac{r_s}{\Delta}\sqrt{\frac{2fN}{\eta}}\,. \tag{6.4}$$

In Fig.6.4 we compare the time evolution of the order parameter $q(t)$ for runs with different angular velocities and find that $q(t)$ saturates in both cases. The fluctuations of the order parameter in the saturated phase are also seen in experiments by Cantelaube and Bideau [1995] and are therefore most probably not an artifact of our method. Both graphs can easily be fitted to an exponential law of the form:

$$q(t) = q_\infty\left(1-e^{-t/\tau}\right) \tag{6.5}$$

where q_∞ denotes the quality of the segregation (or final amount of segregation) and τ the characteristic segregation time.

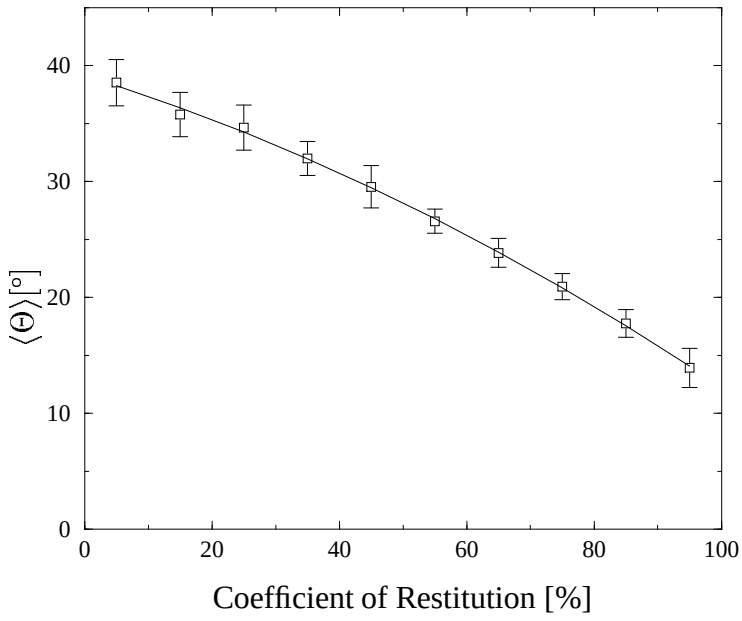

Figure 6.5: The dependence of the angle of repose $\langle\Theta\rangle$ on the coefficient of restitution ϵ_{res} for an angular velocity of $\Omega = 2$ Hz . The solid line is a parabolic fit to the data points.

To get reasonable results, we take Δ to be of the order of the diameter of the larger particles, which gives in our case $n = 11$. For smaller values of n the resolution gets worse and for higher n fluctuations become more pronounced, since there would be "empty" shells with no particle centers in it. For varying n around 11, q has an over-all error of 0.03 for $n \in [9, 20]$ for our simulations.

6.2 Two dimensions

The first investigations for radial segregation are done in 2D, as published in [Dury and Ristow, 1997]. To suppress particle bouncing on the surface,which could disturb the segregation we choose the damping coefficient γ_n to give $\epsilon_{res} = 28.7\%$. The coefficient of restitution has also an effect on the angle of repose, shown in Fig.6.5. With decreasing ϵ_{res} the angle of repose in the rotating drum increases strictly monotonically. The parabolic fit to the data points gives an extrapolated value of $39°$ in the limit $\epsilon_{res} \to 0$. For these values of our parameters the time step is $\Delta t = 0.85 \cdot 10^{-6} s$. In our simulation we use a binary mixture of $N = 1600$ particles with radius $r_S = 0.038$cm and $r_L = 0.064$cm, the fraction of the small particles is $f = 45\%$. Our drum has as usual a diameter of $D = 7$cm and is half filled. The particles and the inner wall of the drum are made of the same material described by the parameters above.

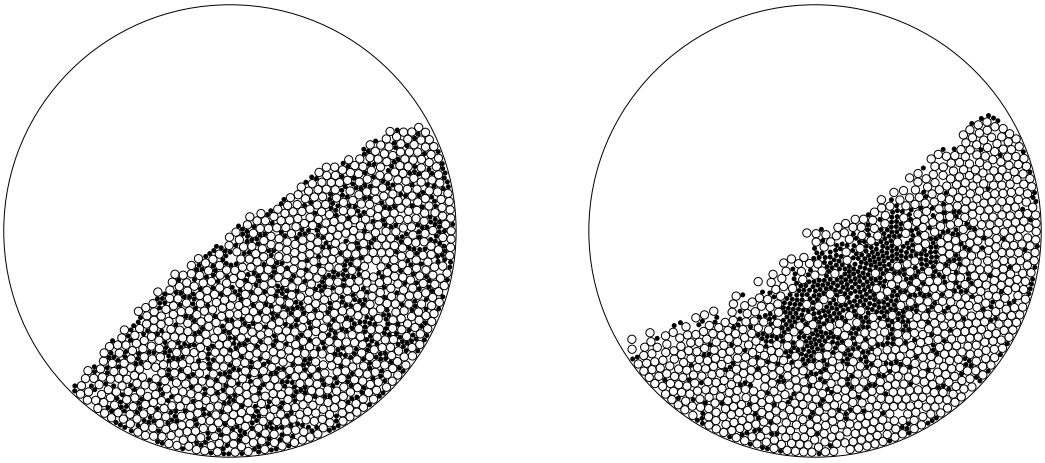

(a) Snapshot of the drum right before the first avalanche.

(b) Snapshot of the drum after rotating $t = 60s$ with angular velocity $\Omega = 1.0$ Hz, i.e. after 9 rotations.

Figure 6.6: 2D-Drum: small particles are drawn as filled circles and large particles as open circles.

6.2.1 Rotating drum

We are starting with a half filled drum in order to minimize the effect of mixing [Metcalfe et al., 1995; Peratt and Yorke, 1996] shown in Fig.6.6(a) and then let the drum rotate with angular velocity Ω . We choose Ω in a region with continuous surface flow just above where we would get distinct avalanches (see Chapter 4). After some revolutions we get a clearly segregated core composed out of small particles drawn as black circles shown in Fig.6.6(b). In order to characterize the segregation quantitatively we investigate the density of small particles at a given distance r from the center of the drum which is similar to the method used by Baumann et al. [1994]. It is interesting to note that right at the wall boundary the density of small particles increases again which we found in all our 2D simulations for different model parameter $k_s\,, \mu, \gamma_n$ and regardless of the angular velocity of the drum. It's height $\rho_{end} := \rho_\Delta(R - \Delta)$ seems to be related to the quality of the segregation since values of ρ_{end} close to or above ρ_0 always gave not well segregated cores. This could be due to some finite size effects and depends on the thickness of the fluidized zone, however in 3D we do not see such an effect. Even though the angle of repose is nearly constant in our range of Ω, $\Theta \approx 33°$, the thickness of the fluidized zone grows with Ω [Ristow, 1996; Nakagawa et al., 1993] and so the small particles can not segregate fast enough through the fluidized layer to the solid block and will end up at the wall. For lower values of Ω, the depletion of the small particles in the outermost shell is faster and the final value around which ρ_{end} fluctuates is lower. This indicates that the

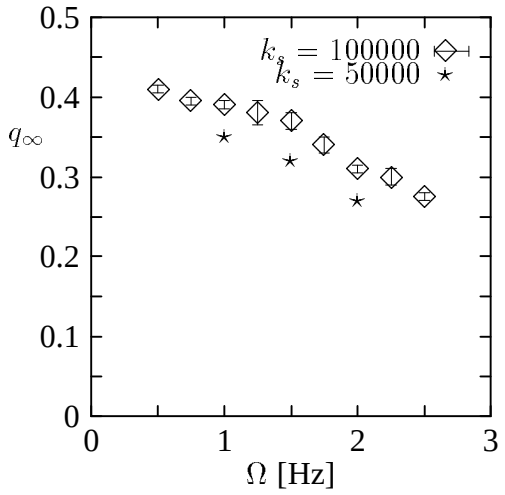

(a) The coefficient $q_\infty(\Omega)$for the quality of the segregation

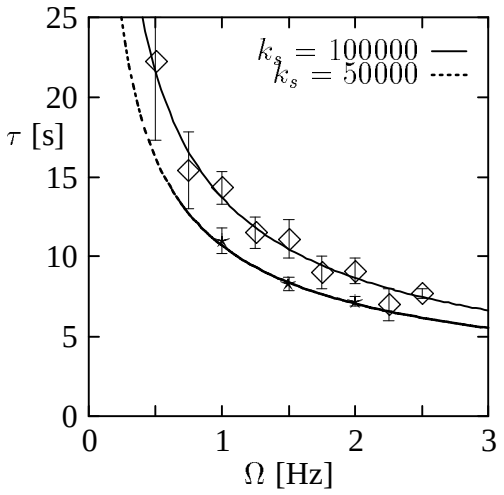

(b) The coefficient $\tau(\Omega)$ for the characteristic segregation time. The solid line corresponds to $\tau(\Omega) = 13.7 \cdot \Omega^{-0.66}$

Figure 6.7: Dependence of the radial segregation $q(t, \Omega)$ on the angular velocity.

maximal achievable amount of segregation is higher for smaller Ω which will be verified and quantified in the next section using our order parameter for two dimensions.

6.2.2 Dynamics of the segregation process

When evaluating the data given in Fig.6.4(b), we get for $\Omega = 0.75$ Hz (a) values of $q_\infty = 0.395$ and $\tau = 15.4s$ whereas for $\Omega = 2.5$ Hz (b) values of $q_\infty = 0.275$ and $\tau = 7.7s$. This states that even though the initial segregation speed is higher for higher values of Ω, the final amount of segregation is less. In order to half the characteristic segregation time τ, Ω has to be increased by a factor of 3. Also shown in Fig. 6.4(b) as dotted line is a test run where we started with a more segregated configuration. The value of q decreases in time and verifies that the order parameter indeed does not reach a value of 1 but rather approaches q_∞. But what is the exact dependence of the quality of the segregation and the characteristic segregation time on the angular velocity of the rotating drum? We start with a rotating speed Ω just above the distinct avalanche regime which gives $\Omega = 0.5$ Hz for our simulation parameters and increase Ω in steps of 0.25 Hz up to 2.5 Hz . The corresponding values of q_∞ and τ are given as function of Ω in Fig. 6.7(a) and 6.7(b), respectively. With increasing Ω , q_∞ decreases only slightly in the beginning up to $\Omega = 1$ Hz but for higher values of Ω the decrease becomes more pronounced. The segregation mechanism is based on the surface flow and with no surface flow there is no segregation. Therefore it is clear that in the limit $\Omega \to 0$ we get $\tau \to \infty$, because for lower and lower Ω we are in the discrete avalanche regime and the separation of the

avalanches grows more and more. The best fit for $\tau(\Omega)$ by a power law gives :

$$\tau(\Omega) = 13.7 \cdot \Omega^{-0.66} \,. \tag{6.6}$$

The natural time scale for the segregation process is the average frequency a particle is exposed to the surface, i.e. the number of revolutions. Defining $n_R := \frac{\tau(\Omega)\Omega}{2\pi}$, we can rewrite the above equation for $\tau(\Omega)$ and obtain

$$n_R = 2.18 \cdot \Omega^{0.33} \,, \tag{6.7}$$

which is shown in Fig. 6.8(a) as solid line where the data points from Fig. 6.7(b) are replotted in this dimensionless fashion. One can see that for higher Ω we need more revolutions to achieve segregation.

In order to discuss the influence of the thickness of the fluidized layer on the characteristic segregation time $\tau(\Omega)$, we vary our simulation parameter k_s which is related to the surface roughness of the material being used. How this influences the layer thickness d_f is shown in Fig. 6.8b) as function of Ω for the three different values $k_s = 50000(\star), 100000(\circ)$ and $150000(\bullet)$. The thickness increases with decreasing k_s. In our regime of Ω, the thickness of the fluidized zone is increasing with increasing angular velocity Ristow [1996]; Nakagawa et al. [1993]. This means that for higher angular velocities the small particles need more time to segregate through the fluidized layer onto the solid block than for lower Ω, therefore the final amount of segregation cannot be as good as for low values of Ω. Even though the segregation speed is better for higher Ω which is due to the greater throughput of material in the fluidized zone it will need more revolutions to achieve the saturated state than for lower angular velocities.

The effect of a larger fluidized zone on the final amount of segregation q_∞ and the initial segregation speed τ is demonstrated in the Fig. 6.7(a), Fig. 6.7(b) and Fig.6.8 by adding some data points for $k_s = 50000$. The dotted line corresponds to the power law fits $\tau'(\Omega) = 10.6 \cdot \Omega^{-0.6}$ and $n'_R = 1.69 \cdot \Omega^{0.4}$, respectively, which verifies that a larger fluidized layer corresponds to a faster initial segregation speed (lower value of τ). But from Fig. 6.7(a), one also reads off that this means a lower value for the final amount of segregation. Thus decreasing the internal friction of the grains seems to have the same effect as increasing the rotation speed of the drum.

6.2.3 Results

Radial segregation is well observed experimentally in rotating drums and we have studied its dynamics and its dependence on the external angular velocity of the drum and the thickness of the fluidized layer with the help of DEM. We found that the quality of the segregation decreases with increasing angular velocity and the characteristic segregation time decreases. The latter seems to diverge in the limit $\Omega \to 0$.

We speculate that in three spatial dimensions, radial segregation is more easily to achieve, since the voids between the particles are connected by a network and small particles could

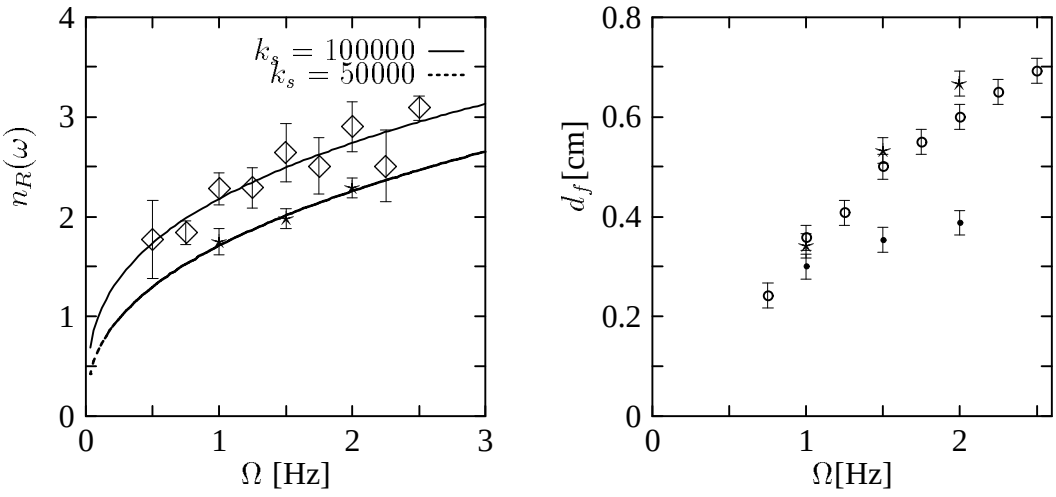

(a) Number of characteristic revolutions n_R to achieve segregation.

(b) Dependence of the thickness of the fluidized zone on k_s for the values $k_s = 50000(\star), 100000(\circ)$ and $150000(\bullet)$

Figure 6.8: Influence of the shear coefficient on the segregational behavior.

traverse through it which will lead to a better segregation. Also in three dimensions small particles colliding with larger ones can be deflected parallel to the direction of the rotational axis and therefore the velocity in direction of the downwards flow is reduced. Hence the particles have more time to segregate until they hit the wall. These hypotheses will be tested in the next section by performing real three-dimensional numerical simulations and investigating the diffusion constants in different directions.

6.3 Three dimensions

Now we turn to 3-dimensional simulations again. In many radial and axial segregation experiments, one of the components are glass beads. They are commercially available in large quantities and can easily be sieved to nearly uniform size distribution. In order to model the dynamics of glass beads correctly with our model, we include rolling friction.

When sufficiently large, the cohesion forces are negligible. In the continuous flow regime, the dynamic angle of repose for glass spheres is independent of the rotation speed of the cylinder as long as the surface remains flat (Sec. 4.1.1 and Zik et al. [1994]). Since they are nearly perfectly round, particle rotations are an important degree of freedom and cannot be neglected in a theoretical or numerical description. Even though the experimentally measured friction coefficient for fresh glass beads is $\mu = 0.092$ [Foerster et al., 1994] for binary collisions, however this can only be viewed as a lower bound in our case due to the wear of material caused by the uncountable bead collisions in the course of the experiment. For particle–particle collisions we use $\mu = 0.19$, and for particle–wall collisions, $\mu_w = 0.6$ to get the right angle of repose. The coefficient of restitution for wall

collisions is set to 0.97 and to 0.831 for particle–particle collisions, which are the measured values for glass beads [Foerster et al., 1994] and the density was set to $\rho = 2.5\frac{g}{cm^3}$. For our value of $\Omega = 15$rpm, we are in the continuous flow regime with a flat free surface and the Froude number is

$$\mathrm{Fr} = \frac{\langle v \rangle^2}{lg} = (2.3 \ldots 9.1) \times 10^{-2} \quad ,$$

so we can neglect inertia effects.

In order to save computer time, we set $\tilde{Y}$ to $6 \cdot 10^4$ Pa m which is about one order of magnitude softer than glass, but we checked that this has no effect on the investigated properties of the material (Chapter 3). This gives a contact time during collisions of $1.1 \cdot 10^{-6}$ s, which is still quite small. The total number of particles we used were up to 17000.

For our simulation we are using a cylinder with diameter $D = 7$cm and periodic boundary conditions along the rotation axis. The cylinder length was 2.5cm with periodic boundary conditions; this is more than twice the range of the boundary effects (see Chapter 5). The cylinder was filled with a binary mixture of large beads having a radius of $R = 1.5$mm and small beads $r \in \{0.75\text{mm}, 1.0\text{mm}, 1.25\text{mm}\}$, where the small particles can have a concentration of 50% or 33% by volume. The aspect ratio of the drum diameter D and the average particle diameter $2r$ is $D/(2r) = 28$, this is of the order of laboratory experiments, where we have $D/(2r) = 25$ up to 40 for the example in Nityanand et al. [1986].

6.3.1 Time evolution of the order parameter

Usually the initial state is a random mixture of small and large particles which gives a value of $q \approx 0$. The order parameter will show a global trend of increasing in time and saturates on the long run when the cylinder rotation is started. A typical time evolution of q using a 50% volume fraction of 1.0mm smaller particles is shown in Fig. 6.9. The general trend can be well approximated by an exponential saturating function of the form of Eq. (6.5) with a characteristic segregation time t_c and a final amount of segregation q_∞. The best fit to the data points for a 50% filling of each of 1.0mm and 1.5mm beads was obtained for the parameters $t_c = (6.1 \pm 0.3)$s and $q_\infty = 0.644 \pm 0.040$ which was added in Fig. 6.9.

Effects of the filling fraction

Experiments performed in the discrete avalanche regime using mono-disperse particles show that the mixing time depends strongly on the volume filling fraction of the cylinder and no mixing is seen for an exactly half-filled cylinder [Metcalfe et al., 1995]. A theoretical description could be given which is based on the mixing between wedges [Metcalfe et al., 1995; Peratt and Yorke, 1996; Dorogovtsev, 1998]. When working in the discrete

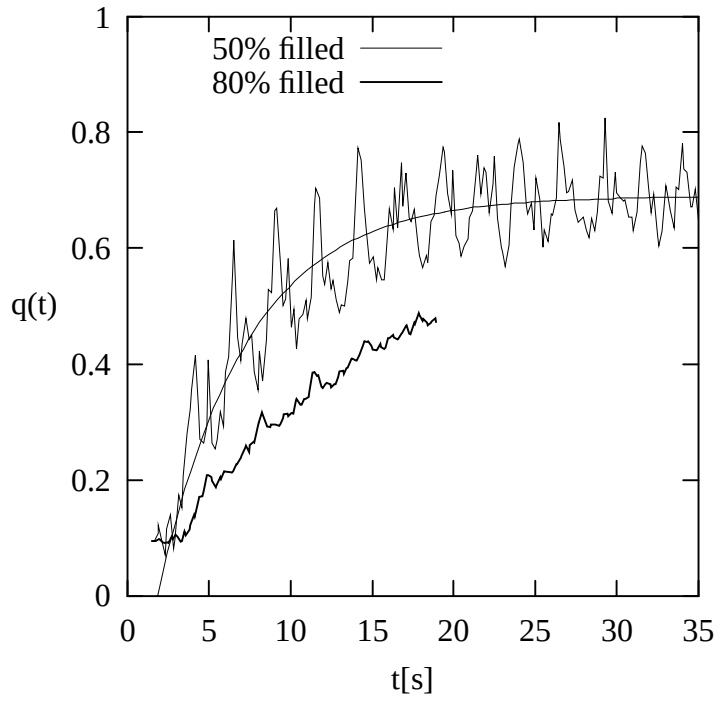

Figure 6.9: Typical time series of the order parameter q for two different filling fractions of the cylinder with 1.0mm and 1.5mm beads.

avalanche regime with an unary mixture , it was found in experiments by Metcalfe et al. [1995] and mathematical models by Peratt and Yorke [1996]; Dorogovtsev [1998] that the least amount of geometrical mixing is given for a half filled drum which could be explained by the avalanche mixing of wedges. Peratt and Yorke [1996] applied their model also to the continuous avalanche regime by taking the limit of an infinitely thin flowing layer and no change in the angle of repose during the flow. This should lead to "infinitely" many avalanches during one revolution and with a finite avalanche duration all these avalanches are superposed and could lead to continuous avalanches (steady flow). However radial segregation is always observed in the continuous flow regime, regardless of the filling fraction of the cylinder and we are investigating numerically the interplay of the two competing phenomena of mixing and segregation, a problem first studied by Rose [1959] and restated by Behringer [1995]. Motivated by these findings, we expected for our setup to get the least geometrical mixing for filling fractions around 50% as well and the strong fluctuations which are most pronounced for a filling fraction of 50% are a clear sign for slow geometrical mixing.

Fourier-transforming these fluctuations gives main peaks for the 50% and the 80% filled drum at $T = (2.56 \pm 0.09)s$ and $T = (3.18 \pm 0.15)s$, albeit the peak for the 80% filled case is much less pronounced than in the 50% case as is shown in Fig. 6.10; higher harmonics are also visible. These times are exactly the time it takes for a particle to make

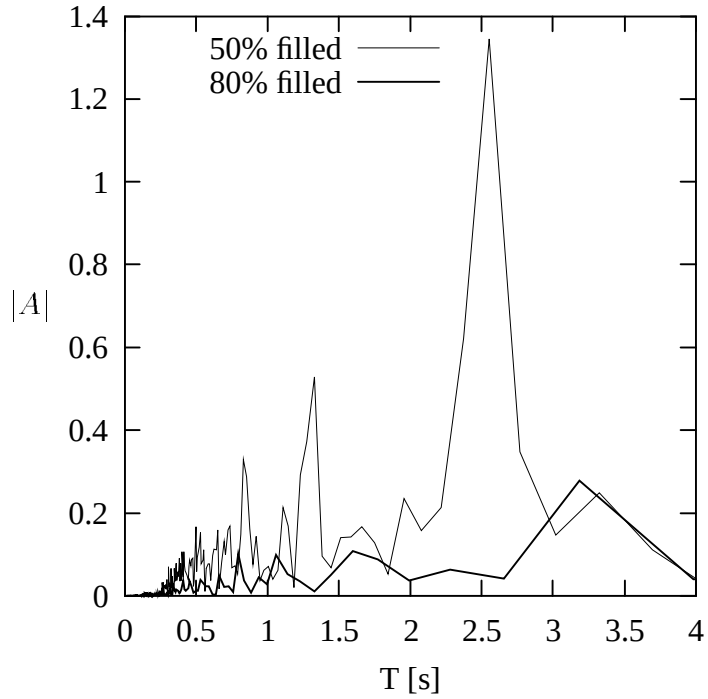

Figure 6.10: Fourier transform of $q(t)$ of Fig. 6.9.

one revolution, i.e. to appear at the same spot again, given as

$$T = \frac{\alpha}{\Omega} + \frac{l}{\langle v \rangle} \tag{6.8}$$

where Ω is the angular velocity of the drum, α the arc where the particle is in the solid block, l the length of the fluidized layer and $\langle v \rangle$ the average velocity of the particles in the fluidized layer. For a half-filled drum this gives $\alpha = \pi$ and $l = 2R$. From this we calculate $\langle v \rangle$ to be $\langle v \rangle = 12.5 \frac{cm}{s}$ in each case. The depth of the fluidized layer is determined as in Chapter 3 by looking at the velocity profile along a line through the center of the drum and perpendicular to the free surface. The depth of the fluidized layer is the distance from the free surface to the point where the velocity profile reaches its zero value.

In Fig. 6.9, the thin line corresponds to a half-filled cylinder and due to a slight asymmetric start configuration, which persists due to the bad geometric mixing, large fluctuations which decrease in time are visible. For other filling ratios of the cylinder the asymmetry in the beginning gets erased by the geometrical mixing and the fluctuations are suppressed or are decaying in a rapid way. This is illustrated by the thick line in Fig. 6.9 which is for a volume filling fraction of 80% and as expected the fluctuations have a much smaller amplitude and do not show such a pronounced periodicity.

To verify the speculation in Sec. 6.2, an extended three-dimensional drum was simulated, containing a binary mixture of small and large particles having a size ratio of 1.65:1, a number ratio of 1:1, and a total of more than 280 000 particles, see Fig. 3.2.

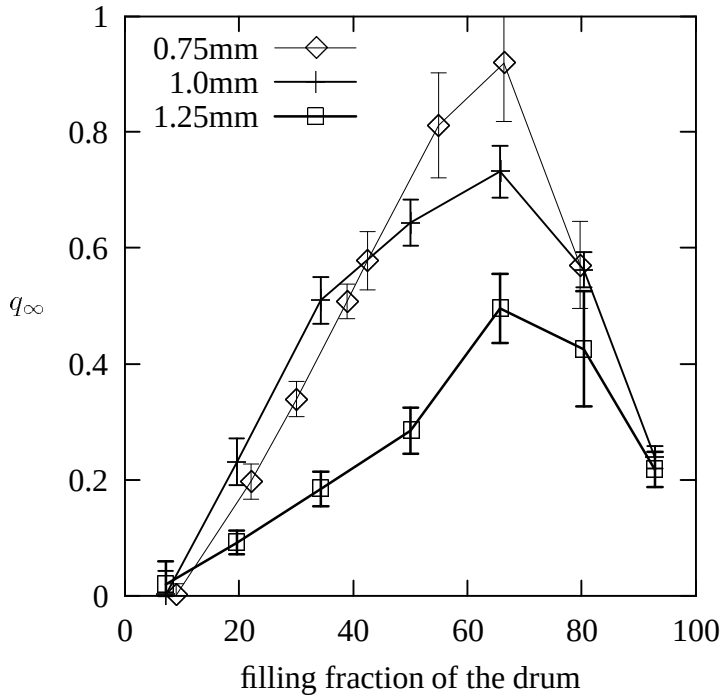

Figure 6.11: Final amount of segregation for a concentration of 50% of small particles and three different size ratios.

We will now turn to the pre-factor of the exponential fit in Eq. (6.5), q_∞, which quantifies the final amount of segregation and study its dependence on the volume filling fraction and on the particle size ratio. This is shown in Fig. 6.11 for three different particle sizes, corresponding to a size ratio of $\Phi := \frac{r}{R} = 0.5, 0.67$ and 0.83 and a concentration of small particles of 50%. For smaller particles, the final amount of segregation is higher for nearly all filling ratios of the cylinder. This can be explained by the higher mobility of the small particles for traversing through the network of voids of the large particles.

Since the geometrical mixing will cause also mixing of the segregated core of small particles with the large particles, best segregation should be achieved for zero mixing, i.e. a filling fraction of 50% when mono-disperse particles are used, see also Sec. 6.3.1. In our case where we have a fluidized layer with finite width, the best segregation occurs not for a half-filled cylinder, instead it occurs for a cylinder where the solid block under the fluidized layer is 50%. So, the width of the fluidized layer plays an important role and it was found that with increasing width, q_∞ will decrease since more and more portions of the already segregated regions will be destroyed again. The segregation speed also increases with the rotation speed of the drum which corresponds to an increase in width of the fluidized layer as well. In our case the fluidized layer has a width of about three to four particles and hence the total filling fraction for the least geometrical mixing would be for a filling fraction of 60%, which is in agreement with our simulations (see Fig. 6.11).

Concerning different concentrations of small particles, our parameter was chosen in such

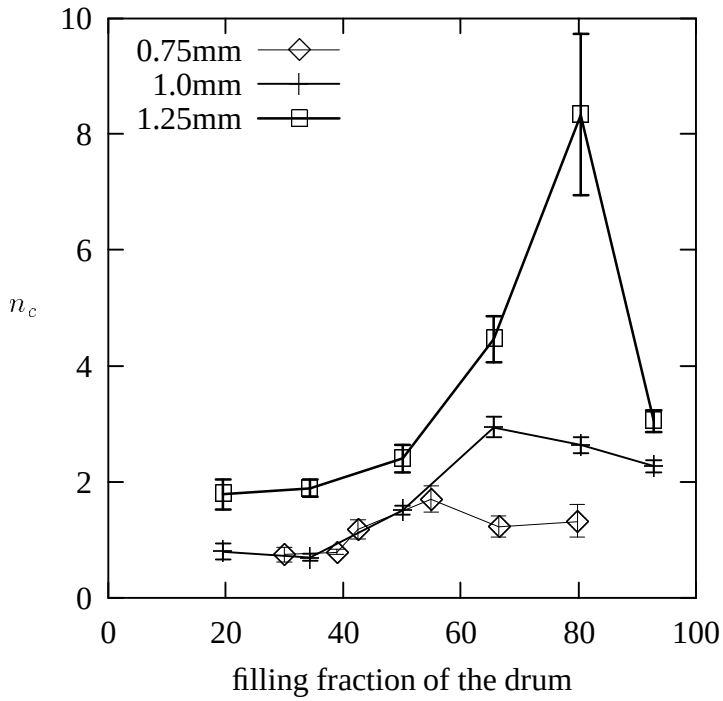

Figure 6.12: Characteristic number of revolutions for segregation for a concentration of 50% of small particles.

a way that the final amount of segregation should be independent of the volume fraction of small particles in the cylinder. We checked this numerically for a concentration of 50% and 33% and found a perfect agreement within the error bars. The speed of the segregation is characterized by t_c, see Eq. (6.5), stating that for $t = t_c$ the system has reached a segregation of 63% of the final value of q_∞. In Fig. 6.12, we plot the characteristic number of revolutions, defined as $n_c = \frac{\Omega t_c}{2\pi}$, as a function of the volume filling fraction of the cylinder for three different sizes of the small particles corresponding to particle size ratios of $\Phi = 0.50, 0.67$ and 0.83 again. The segregation times are sufficiently smaller for the smaller particles which is also found in experiments [Williams, 1976]. They also show a general trend of increasing with increasing filling fraction. However, for a more than half-filled drum, where the exact value depends on the particle size due to the different width of the fluidized layers, the segregation becomes faster again. This can be explained as follows: Due to the nature of the geometrical mixing, an unmixed core will persists in the middle of the cylinder for a filling fraction greater than 50%. The exact number depends on the width of the fluidized layer which depends e.g. on the rotation speed of the cylinder. Close to a filling fraction of one, only a small ring close to the cylinder wall can participate in the segregation process. Consequently, the final amount of segregation is small which agrees with Fig. 6.11, but this value is reached fast, therefore the segregation time, t_c, is small. The numerical data indicates that the filling fraction which corresponds to the maximal value of t_c decreases with decreasing particle size.

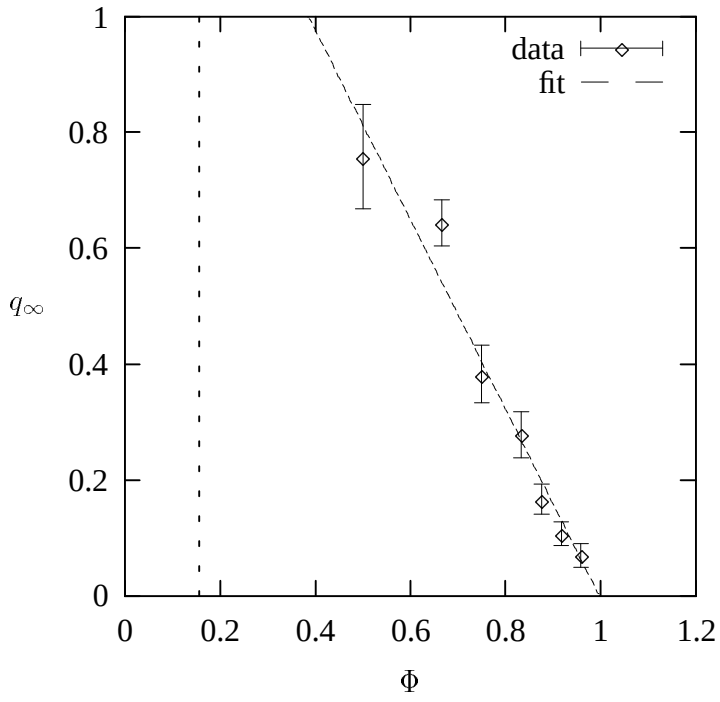

Figure 6.13: Final amount of segregation as function of the particle size ratio $\Phi = \frac{r}{R}$ (the vertical dashed line denotes Φ_T).

Segregation for small size ratio

It is well known, that the segregation process is faster and more pronounced if the particle size ratio becomes smaller [Williams, 1976]. The results from a two dimensional rotating drum model indicate that segregation is observed for an arbitrary small size ratio [Baumann et al., 1994], whereas the data from vertical shaking experiments suggest a cut-off ratio around $\Phi = 0.5$ [Vanel et al., 1997]. In order to address this question, we show in Fig. 6.13 the final amount of segregation, q_∞, as a function of the particle size ratio, Φ, for a concentration of small particles and a volume filling fraction of 50%. Even though obtaining accurate data for values of Φ close to one is rather difficult due to the long segregation time, the data shown in Fig. 6.13 support the hypothesis from [Baumann et al., 1994] that segregation will be present for any finite size difference. This was determined by using a linear fit of the form

$$q_\infty(\Phi) = c(\Phi_0 - \Phi) \tag{6.9}$$

which gives $c = 1.6 \pm 0.1$ and $\Phi_0 = 1.00 \pm 0.02$ when all seven data points are used for the fit; shown as a dashed line in Fig. 6.13. Due to our definition, the maximal achievable value for the final amount of segregation is $q_\infty = 1$. Therefore for small size ratios, the behavior must deviate from the linear dependence which is already visible for the value for $\Phi = 0.5$ which was obtained by interpolating between two filling fractions. Obtaining data points for even lower values of Φ is nearly infeasible by todays computers, due to the large demand on computer time caused by the large particle numbers. For values

of $\Phi \leq \frac{2-\sqrt{3}}{\sqrt{3}}$ (wide dashed line in Fig. 6.13) we expect a completely different behavior since the small particles are then sufficiently small to propagate through the voids of a three–dimensional hexagonal packing. Please note that since we have a random packing, see Fig. 6.2(a), the threshold value should even be higher and $\Phi_T := \frac{2-\sqrt{3}}{\sqrt{3}}$ just serves as a lower bound.

6.3.2 Centroids

In addition, we start with an initial configuration similar to the one used in the original experiment on the mixing of mono-disperse particles Metcalfe et al. [1995] to demonstrate how the radial segregation competes with the mixing process.

After having discussed the segregation dynamics as function of filling fraction and particle size ratio in the preceding sections, we will now turn to illustrate the interplay between mixing and segregation. As already mentioned in Sec. 6.3.1, no geometrical mixing was found for an exactly half-filled drum in the discrete avalanche regime. The continuous flow limit taken in Peratt and Yorke [1996] suggests that this is also true in the continuous flow regime but the numerical data sets given in Fig. 6.11 and 6.12 do not support this hypothesis which can be attributed to the fact that the fluidized layer has a non-zero width.

In order to illustrate this point in more depth, we are starting with an initial configuration where the left half of the cylinder is purely composed out of large beads (R=1.5mm) and the right half out of small beads (r=1.0mm) giving a total number of 4420 particles (see Fig. 6.14, top left picture). After turning the drum counter-clockwise for 1.6 seconds at $\Omega = 15$rpm, which would simple interchange the regions occupied by large and small particles if no mixing would be present, the interface is still well defined and nearly a straight line (top right picture). After turning for 2.8 seconds, the interface between the large and small beads is still quite sharp, albeit it is not a straight line anymore. After the start of the rotation, it takes 0.23 seconds for the continuous flow to set in and from Sec. 6.3.1, we recall that it takes roughly 2.65 seconds for a particle to undergo a full revolution. The tongue of small particles into the large ones at the center of the cylinder is the starting point of forming a core of small particles. After rotating for 5.3 seconds, which corresponds to two full particle revolutions, the formation of a core of small (white) particles is even more pronounced. After two full particle revolutions, $t = 7.8$s, the shape of the interface between large and small particles close to the cylinder wall becomes even more diffusive. It rather resembles a diffusion process along the azimuthal direction which can be described in a similar fashion as the front propagation along the axial direction in rotating cylinders [Ristow and Nakagawa, 1998]. The segregation mechanism in the pre–set cylinder starts immediately, i.e. *no* mixing of the two components is necessary in order to obtain a radially segregated core of small particles. The final picture in Fig. 6.14 (bottom right) corresponds to 28 particle revolutions and shows a nearly symmetric, well segregated cluster of small particles. Also note that hardly any large

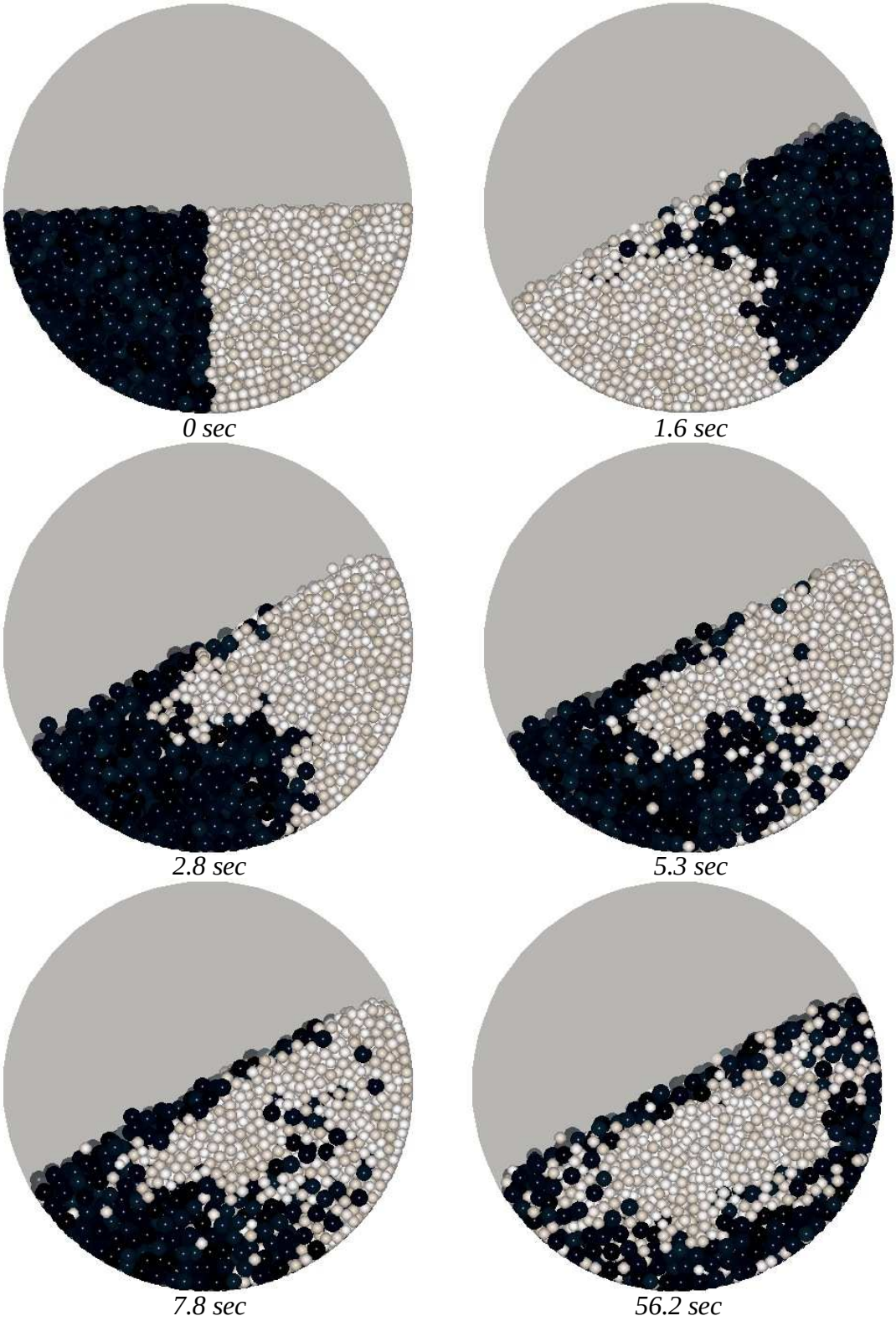

Figure 6.14: Different snapshots of the cylinder with a starting condition, where initially all the small (large) particles are on the right (left) side of the cylinder (particle radii 1.0mm and 1.5mm).

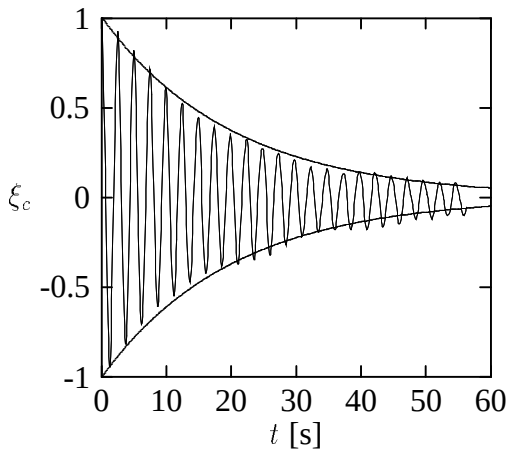

(a) Normalized centroid position projected onto the free surface of a half-filled cylinder with 1.0mm and 1.5mm particles.

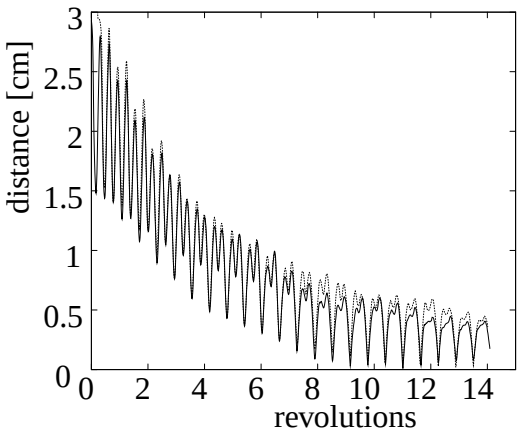

(b) Distance of the centers of a half–filled cylinder with 1.0mm and 1.5mm particles (- - - clockwise, — counter-clockwise rotation).

Figure 6.15: Centroid distance.

particles are found in the segregated core of small particles whereas smaller particles are still found close to the wall of the drum. We expect the latter effect to disappear when the drum is rotated for long enough times.

In order to determine the degree of mixing in the horizontal cylinder along the initially sharp vertical front we use a procedure proposed by Metcalfe et al. [1995]. We calculate the center of mass for each particle size, project it onto the free surface which is initially horizontal and calculate the distance of each of the two centers of mass. The time evolution of this distance, ξ_c, which was made dimensionless by dividing by the distance of the start configuration is shown in Fig. 6.15(a). It corresponds to the configuration shown in Fig. 6.14, i.e. a half-filled cylinder containing an equal volume fraction of 1mm and 1.5mm particles. This procedure was used [Metcalfe et al., 1995] to show the mixing of mono-disperse particles in a rotating drum at a filling fraction of $f = 39\%$. Since geometrical mixing is observed for this filling fraction, the centroid positions decayed in time and could be well approximated by

$$\xi_c(t) = \cos\left(\frac{2\pi t}{T}\right) e^{-t/t_c} \tag{6.10}$$

where T stands for the period, see Eq. (6.8). On the contrary, no geometrical mixing is observed for mono-disperse particles in a half-filled drum which would correspond to a characteristic time $t_c = \infty$ in Eq. (6.10) and lead to non-decaying oscillations. For a binary particle mixture, the segregation process will lead to a decay of the distance of the two centroids in time for *any* filling fraction and we have chosen to present numerical results for counter-clockwise rotation and $f = 50\%$ in Fig. 6.15(a) to illustrate this.

The numerical data can be well fitted by an exponentially decaying oscillation according to Eq. (6.10). This gives $T = 2.48$s which is in excellent agreement with Fig. 6.10, and values of $t_c = 20.7$s for clockwise rotation and $t_c = 20.1$s for counter-clockwise rotation which are the same within the error. The exponentially decaying part was added to Fig. 6.15(a) as dashed line. In the beginning, $t < 20$s a slight asymmetry is visible towards negative values which was also observed in other numerical simulations using a two dimensional geometrical model Baumann [1997]. However, if this persists on the long run and will led to a final non-zero value for the centroid position could not be determined by this procedure since the deviations from the exponential fit were usually higher than the calculated offset of (0.004 ± 0.001)cm. Since the numerical data seems to indicate that a pure exponential decay is too slow in the beginning and two fast for longer times we also tried a stretched exponential decay of the form $e^{-(t/t_c)^\beta}$. This gives values of $t_c = (14.0 \pm 1.8)s$ and $\beta = 0.88 \pm 0.05$. However, we can not rule out that the deviation of the exponential law may be due to the numerical noise and a more general statistical theory is needed to resolve this question.

The procedure described above to follow the centroid dynamics is not capable to determine the depth of the centroid position below the free surface due to the projection onto the surface. However, the last picture of Fig. 6.14 shows that the number of layers of large particles below and above the segregated cluster of small particles is not the same. This leads to different distances of the center of mass below the free surface for small and large particles. To determine its dynamic, we plot in Fig. 6.15(b) the Euclidean distance of the two centroids. When properly shifted by $T/2$, the curves for clockwise and counter-clockwise rotations show a similar behavior where fluctuations are a little less pronounced for the latter case. The minima correspond to configurations similar to the one shown in the bottom right picture of Fig. 6.14 when the two centers of mass lie on a line which goes through the origin of the drum. Even though the minimal distance during the time evolution is close to zero, a non-zero value of 0.22cm is estimated for the stationary state without oscillations.

6.4 Results

The main conclusions of this chapter are as follows. In the continuous flow regime size segregation takes place for arbitrary small differences in particle size. To quantify this result, we introduced an appropriate order parameter, which allowed us to compare directly all different drum scenarios. From this we showed that the radial segregation process is faster and more pronounced for particles with a large size difference and that the final amount of segregation shows a linear dependence when approaching a particle size ratio of one; thus no threshold value for radial segregation exists, which was an unresolved question for long time.

We also studied in detail the interplay between mixing and segregation in rotating cylinders for different volume filling fractions of the cylinder and found that the highest

achievable segregation can be obtained for a slightly more than half-filled cylinder and therefore also least mixing. The difference to a mono-disperse system in the discrete avalanche regime could be attributed to the fluidized layer leading to a partial destruction of the underlying already segregated core where the destruction increases with layer width.

When starting with an initial configuration that contains well–separated regions of small and large particles no mixing of the components is necessary in order to obtain a radially segregated core. This inter-penetration process resembles a diffusion process and segregation starts immediately without undergoing a previous mixing of the two particle components.

7 Diffusion coefficients

Whereas in the previous chapter only the dynamics in slices perpendicular to the rotational axis were studied, i.e. radial segregation, we are looking now on the dynamics along the rotational axis, motivated by the phenomenon of axial segregation (first observed by Oyama [1939]). When particles with different sizes are put in a rotating drum, eventually bands composed of small particles will likely emerge along the rotational axis. These bands of small particles are relatively pure, whereas the separating regions are not only composed of large particles, but sometimes also a radial core of small particles is present. This band formation we call *axial segregation*. This kind of segregation happens on a much longer time scale than radial segregation, axial bands are typically formed within minutes to hours. Also in contrast to the radial segregation, not all polydisperse systems show axial segregation; this is still an unsolved question whether a polydisperse mixture of particles will eventually segregate or not. This phenomenon of axial segregation is long known [Oyama, 1939; Donald and Roseman, 1962; Bridgewater, 1976] and an example is shown in Fig. 2.2, but the origin of these bands [Nakagawa, 1994; Zik et al., 1994; Hill and Kakalios, 1995] and whether they are stable [Choo et al., 1997; Frette and Stavans, 1997] or not is still debated. One suggested mechanism builds on the observation that axial segregation occurs when the smaller particles have a higher angle of repose. Due to local concentration fluctuations, there will be regions with less small particles and therefore with a lower angle of repose (as shown in Fig. 2.3). Now the larger particles from the neighboring sides with the higher angle of repose will go into this region and therefore enlarge the fluctuation. This systematic self-concentrating effect would lead to zones with no large particles and zones with a very high percentage, eventually 100%, of large particles. Another possible mechanism is due to the percolation of small particles in the solid block. This might become the dominating mechanism when the radial segregation has set in. In that case, only few small particles will be present in the fluidized surface layer and the particle transport of the smaller species has to go through the radially segregated core, which is certainly much slower than the surface mechanism. But more work needs to be done to fully understand the interplay of these mechanisms.

To demonstrate the band formation, we prepared different binary mixtures, 50:50 by volume, of various round particles, e.g. glass beads, pharmaceutical pills, mustard and poppy seeds. No band formation could be observed using the pharmaceutical pills and the most stable configuration was obtained by using small mustard seeds with a diameter of 1.7 mm and poppy seeds with a diameter of 1 mm. The drum was 26 cm long, 7 cm in diameter and half filled with the initially well mixed particles. In Fig. 7.1, we show the concentration of poppy seeds along the rotation axis in weight percentage.

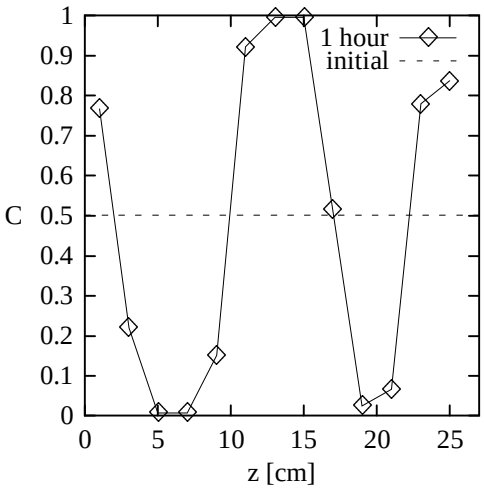

Figure 7.1: Density profile for poppy seeds after rotating a mixture of poppy and mustard seeds for one hour.

Two curves are shown: The dashed line corresponds to the initially mixed state, with an average value of 49.7%, which agrees very well with the wanted 50%. The second line with the diamonds corresponds to the weight percentage of the poppy seeds after the drum was rotated for one hour at 30 rpm. Then the mixture of small mustard seeds with poppy seeds shows a very sharp and pure stable band pattern with 3 bands and 2 end bands.

The common method to study the segregation process starts from a well mixed state and records the segregation amount or pattern as function of time. This works well in the case of radial segregation and quantitative results regarding the dependence of the segregation process on rotation speed and size ratio were obtained using a suitable, normalizable order parameter (Chapter 6). However, the axial segregation process is much richer due to the three-dimensional particle motion. Small changes in the initial mixture seem to have a large effect on the band formation process. The final number of bands, their positions and widths varied from experiment to experiment. Nakagawa [1994] found the three band configuration to be stable after an extended number of rotations. These bands are normally not pure and a radially segregated core of smaller or/and denser particles might still be present. Chicharro et al. [1997] rotated two sizes of Ottawa sand for two weeks at 45 revolutions per minute (rpm) and found a final state of two *pure* bands each filling approximately half of the cylinder, i.e. *no* radial core was found.

In order to have a better defined initial configuration for binary mixtures, it was proposed to fill one half of the drum with one particle component and the other half with the other component [Nakagawa et al., 1997b] which is sketched in Fig. 7.2 for a system with different size particles.

The large particles have a diameter of 3 mm and a density of $\rho_l = 1.3\frac{g}{cm^3}$. The material properties of the large particles were chosen to correspond to the measured values of

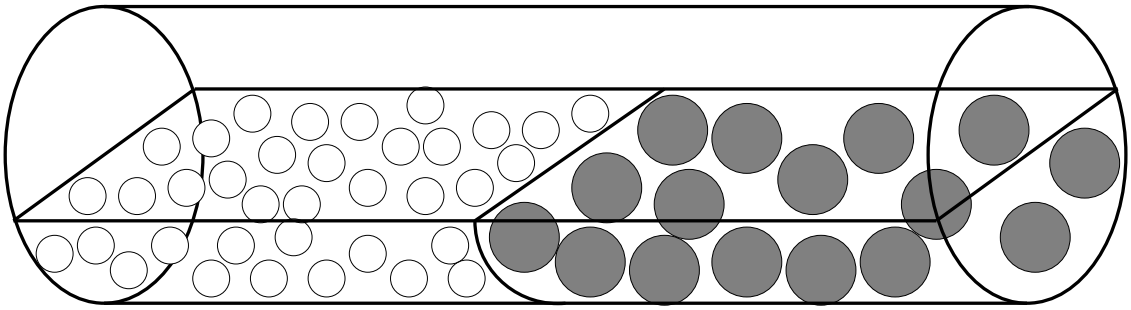

Figure 7.2: Sketch of the initial configuration: large particles are all in the right half of the cylinder and shown in gray. Taken from Dury and Ristow [1998b]

mustard seeds [Nakagawa et al., 1993]. The small particles have a diameter of 2 mm. In order to save computer time, we set $\tilde{Y}$ to $8 \cdot 10^3$ Pa m which is about one order of magnitude softer than desired, but we checked that this has no effect on the investigated properties of the material. This gives a contact time during collisions of $8.5 \cdot 10^{-5}$ s. The total number of particles we used were up to 13 300.

7.1 Dynamic angle of repose

Depending on the particle kinds used in the experiments, the band formation process is more or less pronounced and for some combinations not observed at all. Different explanations have been proposed:

(a) Donald and Roseman [1962] concluded from their experiments that no banding occurs when the smaller particles have a smaller *static angle of repose*;

(b) Das Gupta et al. [1991] modified this statement by saying that the relevant quantity is the difference in surface angle of the two components at a specific rotation speed (*dynamic angle of repose*) and

(c) Hill and Kakalios [1995] proposed a model based on a diffusion equation with an *effective diffusion coefficient* to account for their finding of "reversible axial segregation".

Recently it was argued that other transport mechanisms can drive the segregation process, especially that avalanches play a role [Frette and Stavans, 1997].

Using numerical simulations enables us to study arbitrary angle differences by varying the inter-particle friction coefficient μ in the tangential forces (Eq. 3.10). For collisions between large particles, a value of $\mu_l = 0.2$ is used, whereas when large particles touch the wall, a value of $\mu_w = 0.4$ is used. The additional friction at the end caps leads to an angle difference of 5° in our case which is in agreement with experiments. In order to test different angle differences, the inter-particle friction coefficient for the small particles, μ,

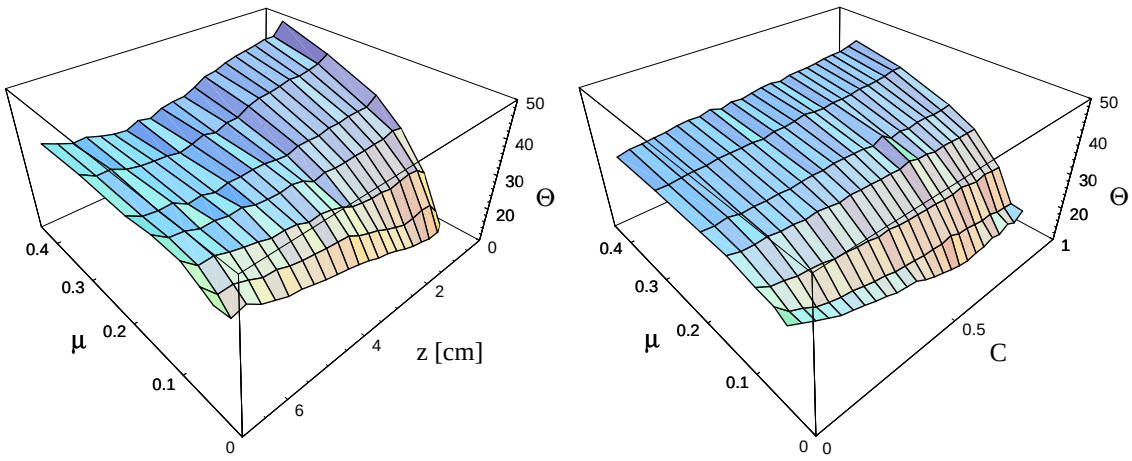

(a) Position along the rotation axis z.

(b) Concentration of small particles C.

Figure 7.3: Surface plot showing the dynamic angle of repose as function of friction parameter μ.

was varied from 0.05 to 0.4. For collisions between large and small particles, a value of $\mu_{\text{eff}} = \sqrt{\mu_l \, \mu}$ is used.

In Fig. 7.3(a), we show the spatial variation of the dynamic angle of repose, Θ, and its dependence on μ. The drum length was $L = 7$ cm and the region initially occupied by small particles corresponds to the interval $z = 0 \ldots 3.5$ cm to the right. The angles were measured by dividing the drum into 22 slices along the rotation axis and we determined the angle of repose for a rotation speed of 15 rpm via the center of mass of all particles in each slice. In order to reduce the fluctuations, we averaged the angles over an interval of 2 seconds after the first initial avalanches. When μ is increased from 0.05 to 0.4, the measured angle at the right wall shows a drastic increase from roughly 10° to 45°. For glass beads, no size dependence of the dynamic angle of repose is observed [Zik et al., 1994], which corresponds to a value of $\mu = 0.2$ in our numerical model. Also clearly visible are the effects of the two cylinder end caps at $z = 0$ and 7 cm, which lead to a higher angle due to the additional wall friction and was studied in detail in Chapter 5.

From our numerical data, we can also calculate the concentration dependence of the dynamic angle of repose. In order to reduce the influence of the boundary caps, we only use the values for the angle of repose from the 16 central slices and calculate the volumetric concentration of small particles in each slice, denoted by C, which is shown in Fig. 7.3(b) as function of the friction coefficient of the small particles, μ. The graph shows the same general trend as Fig. 7.3(a) and one can read off that no concentration dependence is observed for $\mu = 0.2$ which agrees very well with an experimental study of 2 and 4 mm liquid-filled spheres [Hill et al., 1997b]. In the same experiment, the concentration dependence was investigated for a rotation speed of 30 rpm and it was

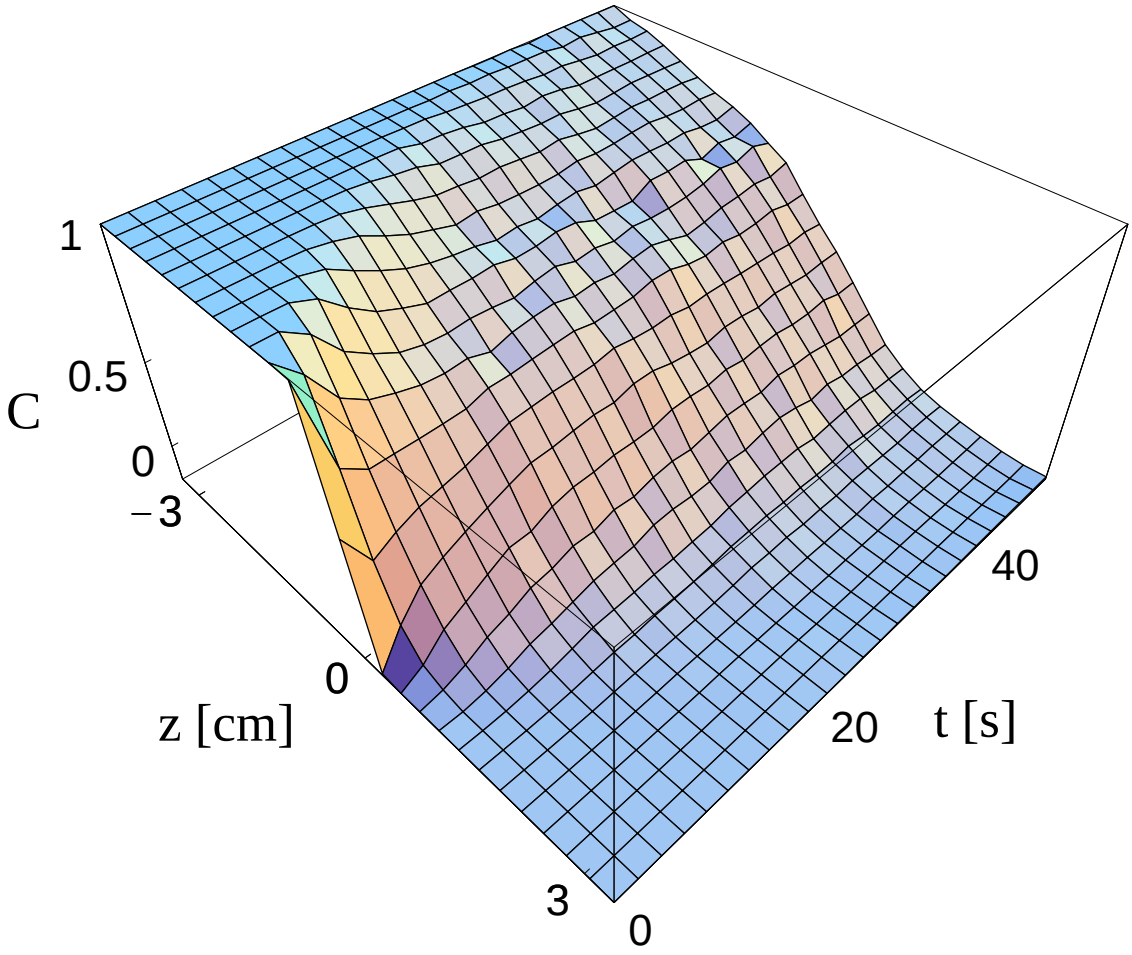

Figure 7.4: Surface plot showing the time evolution of the concentration profile for small particle along the rotation axis z.

found that the angle increases with increasing concentration. Our numerical data clearly indicates that such a behavior can also be found when the small particles have a higher friction coefficient than the large particles, see e.g. the values for $\mu = 0.4$ in Fig. 7.3(b).

7.2 Front advancement

The initial sharp interface between the regions occupied by large and small particles, see Fig. 7.2, will deform and move mostly due to particle diffusion in the fluidized surface layer. The shape dynamics and the interface propagation was investigated for 1 and 4 mm liquid-filled spheres using magnetic resonance imaging (MRI) [Ristow and Nakagawa, 1998]. A nearly fully segregated core of small particles was observed after rotating a 10 cm long, 7 cm wide drum for 10 min at 11.4 rpm. Since recording a full three-dimensional MRI-image is still a time-consuming task and requires special equipment, most studies divide the drum into vertical slices along the rotation axis and record the particle concentration in each slice [Hogg et al., 1966; Cahn and Fuerstenau, 1967;

Nakagawa et al., 1997b]. This leads to a one-dimensional description of the mixing or segregation process and a typical example from our numerical study is shown in Fig. 7.4. The origin was shifted by half the drum length to give a position of $z = 0$ cm for the initial interface which will be used throughout the rest of this chapter. The friction coefficient was $\mu = 0.2$ and the density ratio $\rho/\rho_l = 0.82$ where ρ_l denotes the reference density of the large particles. The initial sharp interface is clearly visible to the left and one notes how the interface broadens in time. For $t = 36$ s, the first small particles have reached the right wall and consequently, the concentration values at the boundaries will start to deviate from their initial values, already visible in the profile to the far right for $t = 50$ s.

7.2.1 Approximation through pure diffusion process

Assuming random particle motion in the axial direction (z axis), one component systems could be well described by a diffusion process according to Fick's Second Law [Hogg et al., 1966; Cahn and Fuerstenau, 1967]. The interface of a two component system can also be studied in this fashion and the diffusion equation reads

$$\frac{\partial C(z,t)}{\partial t} = \frac{\partial}{\partial z}\left(D\frac{\partial C(z,t)}{\partial z}\right) \tag{7.1}$$

where $C(z,t)$ and D denote the relative concentration by volume of the smaller particles and the corresponding diffusion coefficient, respectively. The initial condition for a cylinder with length L are

$$C(z,0) = \begin{cases} 1, & -\frac{L}{2} \leq z < 0 \\ 0, & 0 < z \leq \frac{L}{2} \end{cases}$$

whereas the boundary conditions read

$$\left.\frac{\partial C}{\partial z}\right|_{z=-\frac{L}{2}} = \left.\frac{\partial C}{\partial z}\right|_{z=\frac{L}{2}} = 0$$

which states that there is zero axial flux at the boundaries due to the end caps.

For a constant diffusion coefficient, Eq. (7.1) can be solved analytically for the specified initial and boundary conditions and the solution reads

$$C(z,t) = \frac{1}{2} - \frac{2}{\pi}\sum_{k=1}^{\infty}\frac{1}{2k-1}\exp\left(-\frac{(2k-1)^2\pi^2 Dt}{L^2}\right)\sin\left(\frac{(2k-1)\pi z}{L}\right) .$$

In order to study the short time behavior, we can solve our system by diffusion in an infinite cylinder. This is valid as long as the concentrations at the real cylinder boundaries have their initial values. Solving Eq. (7.1) for this system gives [Crank, 1975]

$$C(z,t) = \frac{1}{2}\left[1 - \mathrm{Erf}\left(\frac{z}{2\sqrt{Dt}}\right)\right] \tag{7.2}$$

where $\mathrm{Erf}(x) = \frac{2}{\sqrt{\pi}} \int_0^t e^{-t^2} dt$ is the error function. To determine now the diffusion coefficient we build the norm of

$$\mathfrak{A}(t) := (C(.,t) - C(.,\infty)) \in \boldsymbol{L}_2[0, \frac{L}{2}] \tag{7.3}$$

where $C(z,\infty) = \frac{1}{2}$ is the steady state concentration:

$$\begin{aligned} ||\mathfrak{A}(t)||^2 &= \int_{-L/2}^{0} (C(z,t) - C(z,\infty))^2 \, dz \\ &= \int_{-L/2}^{0} \left(\mathrm{Erf}\left(\frac{z}{2\sqrt{Dt}} \right) \right)^2 dz \end{aligned} \tag{7.4}$$

which leads to

$$\begin{aligned} &= \frac{L}{2} \mathrm{Erf}^2 \left(\frac{L}{4\sqrt{Dt}} \right) - \sqrt{\frac{Dt}{\pi}} \left\{ -2\sqrt{2} \mathrm{Erf} \left(\frac{L}{2\sqrt{2Dt}} \right) \right. \\ &\quad \left. + 4 \exp\left(\frac{-L^2}{16Dt} \right) \mathrm{Erf} \left(\frac{L}{4\sqrt{Dt}} \right) \right\} . \end{aligned} \tag{7.5}$$

But this result holds anyway just for small t where $C(L/2,t) \simeq 1$ and therefore we have

$$\mathrm{Erf}\left(\frac{L}{4\sqrt{Dt}} \right) \simeq 1$$

and out of the monotonic behavior of Erf() also

$$\mathrm{Erf}\left(\frac{L}{2\sqrt{2\,Dt}} \right) \simeq 1$$

and for small t we also have

$$\exp\left(-\frac{L^2}{16\,Dt} \right) \simeq 0 \, .$$

Using this we finally get

$$||\mathfrak{A}(t)|| = ||\mathfrak{A}(0)|| \left(1 - \frac{4}{L} \sqrt{\frac{2Dt}{\pi}} \right) \, . \tag{7.6}$$

The physical interpretation of $||\mathfrak{A}(t)||$ will become clearer by looking at a concentration profile extracted from Fig. 7.4 which is shown in Fig. 7.5(a). Three profiles are shown, namely the theoretical initial concentration profile as thick line, a computed profile for $t = 10$ s denoted by circles and the expected steady state profile as dotted line. The

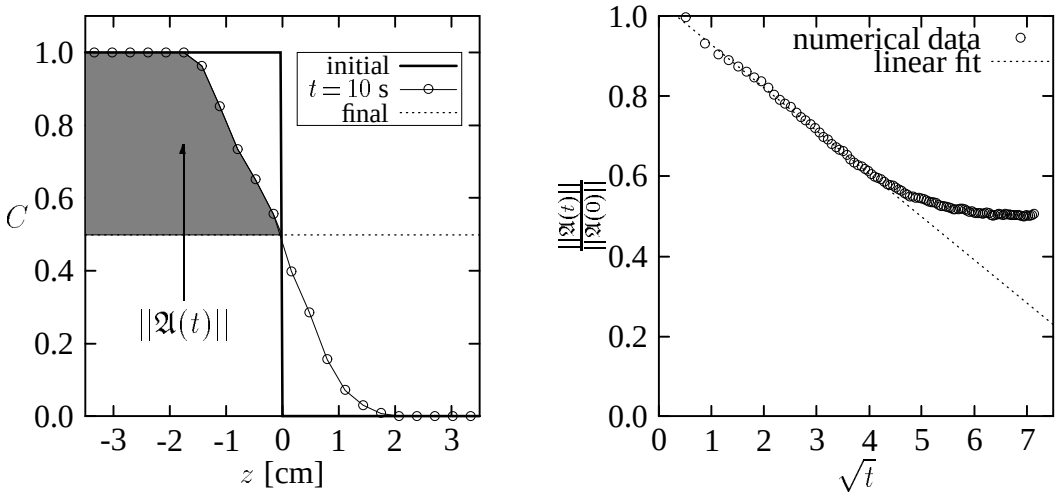

(a) Concentration profiles for different times, from Fig 7.4.

(b) Plot of $\frac{||\mathfrak{A}(t)||}{||\mathfrak{A}(0)||}$ vs. $\sqrt{t}$. The linear fit, shown as dashed line, is used to determine the diffusion coefficient.

Figure 7.5: Determination of the diffusion coefficient out of the concentration profile.

quantity $||\mathfrak{A}(t)||$ is a measure of how close the concentration profile is to the expected steady state profile and we shaded the region which enters our calculations in Eq.(7.4).

The highest value of $||\mathfrak{A}(t)||$ is given for $t = 0$ s and a decrease linear in $\sqrt{t}$ is expected for short times, see Eq. (7.6). This is shown in Fig. 7.5(b), using the same simulation parameters as for Figs. 7.4 and 7.5(a), where we plot $||\mathfrak{A}(t)||$ normalized by the initial value $||\mathfrak{A}(0)||$ vs. $\sqrt{t}$. From the slope of the linear fit shown as dotted line in Fig. 7.5(b), we can calculate a constant diffusion coefficient based on our approximations which gives $D = 0.022 \pm 0.002$ cm^2/s and agrees well with values extracted from experiments [Ristow and Nakagawa, 1998]. When small particles are close to the opposite wall, our approximation of an infinite long cylinder does not hold anymore which leads to a systematic deviation from the $\sqrt{t}$-behavior, visible for times larger than 20 s in Fig. 7.5(b). For this specific run, the first small particle can be found in the slice at the opposite wall at $t = 32$ s. This time difference of 15 s where the graph deviates from the linear behaviour and the time the first particle reaches the boundary comes from the fact that the particles feel the boundary quite early.

7.2.2 Dependence on friction coefficient

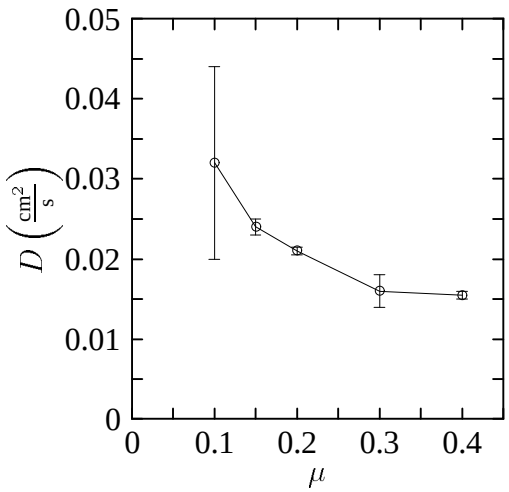

Figure 7.6: Diffusion coefficient for different values of μ of the small particles.

The dependence of the diffusion coefficient on the friction coefficient of the small particles is quite small and shown in Fig. 7.6. The tendency of lower D for higher μ even persists for quite large friction coefficient where small particles have a much higher angle of repose than the large particles (for $\mu = 0.2$ and $\Omega = 15$ rpm the angle of repose is the same for large and small particles). This weak dependence can be explained by the so called "roller coaster" effect. Suppose we have a sharp front between small and large particles, then the angle of repose exhibits also a sharp front. A particle on top of the free surface with the higher angle of repose will see the angle difference and the motion of the particle will be directed towards the region of the lower angle of repose. But the same thing happens in the lower part of the free surface, where now the situation is reversed, and the particle will move back. Therefore, in first approximation, there will be no net effect on the drift (or diffusion) due to this differences in the angle of repose and what is left is a normal random walk on the free surface of the particle. If we now pay tribute to the fact that our particles have different sizes and therefore will exhibit radial segregation, the "roller coaster" motion will not be as perfect as described above. Suppose the small particles exhibit a higher angle of repose ($\mu > 0.2$), the path of small particles will lead over the free surface of the large particles and they can therefore be trapped into a radial core, thus will be removed from the free surface motion and so also from the diffusion process, which decreases the diffusion coefficient D. On the other hand for $\mu < 0.2$, large particle will not be trapped into a core and can continue to participate in the diffusional process even when they get stuck during the "roller coaster" motion, which is more probable the wider the "roller coaster" path, i.e. the larger the differences in the angle of repose. So D increases with decreasing μ.

In order to demonstrate the increase of radial segregation due to an increase of friction coefficient, we show in Fig. 7.7 two cross sections of the drum which represent the configuration close to the initial interface. For a value of $\mu = 0.15$, we show in part (a) the particle configuration at $t = 33$ s and a segregation of the small particles, drawn in white, is hardly visible. In contrast to this, a nice segregation is visible in part (b), which shows a configuration for $\mu = 0.4$ and $t = 27$ s. This supports our hypothesis that radial segregation will *hinder* the diffusion of small particles and thus decrease the diffusion

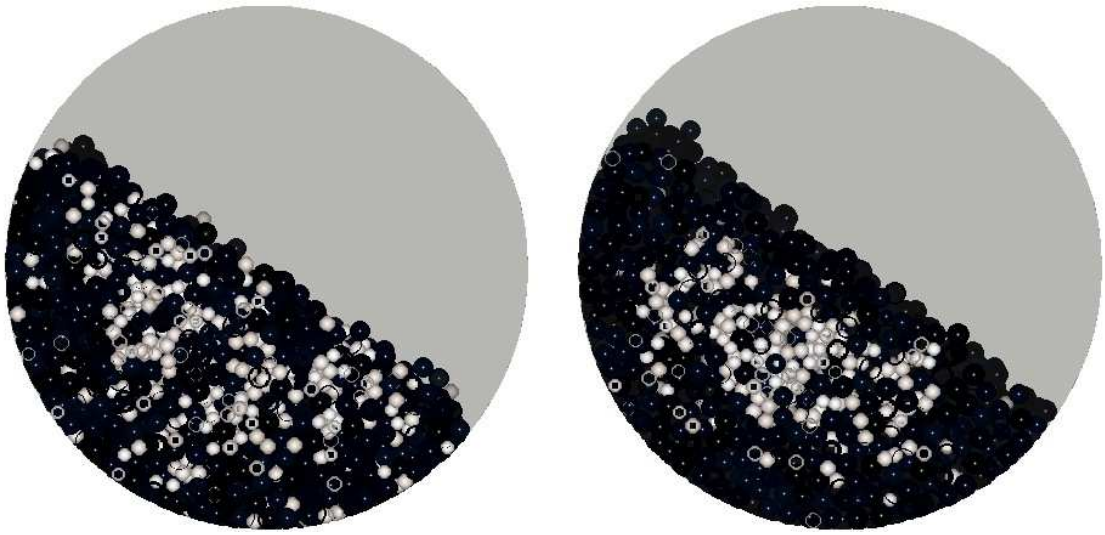

(a) $\mu = 0.15$ at $t = 33$ s (b) $\mu = 0.4$ at $t = 27$ s

Figure 7.7: Cross section of the drum close to the inital interface.Large particles are shown in black and small particles in white.

coefficient with increasing friction coefficient.

7.2.3 Dependence on rotation speed

When investigating the mixing process of glass beads, Hogg et al. [1966] found that the dynamics could be well described by using the number of revolutions instead of the time in Eq. (7.1). This immediately implies that the calculated diffusion constant should be directly proportional to the rotation speed of the drum. We checked this for our system by investigating an Ω-range of 7.5 to 45 rpm for the simulation parameters $\rho/\rho_l = 1$ and $\mu = 0.15$ which is shown in Fig. 7.8. Also shown as dashed line is the linear dependence proposed in Hogg et al. [1966] and as expected it is only a valid assumption for low rotation speeds. On the other hand, our numerically calculated values for D rather shows a more than linear dependence when the whole Ω-range is considered, which we fitted by a quadratic function and added as a solid line to Fig. 7.8. This deviation from the linear behavior is due to the fact that the particle will bounce off the cylinder wall, after they flowed down the free surface. This effect of bouncing is also observed in experiments.

7.2.4 Dependence on density ratio

Turning now to different density ratios ρ/ρ_l for constant $\mu = 0.2$, shown in Fig. 7.9, we see a quite huge dependence of the diffusion coefficient (Fig. 7.9(a)). In contrast to the previous section, the radial segregational behaviour will change. In general, smaller and denser particles will segregate radially, so increasing the density ratio will enhance radial segregation, but when decreasing the density ratio, the larger particles become denser and

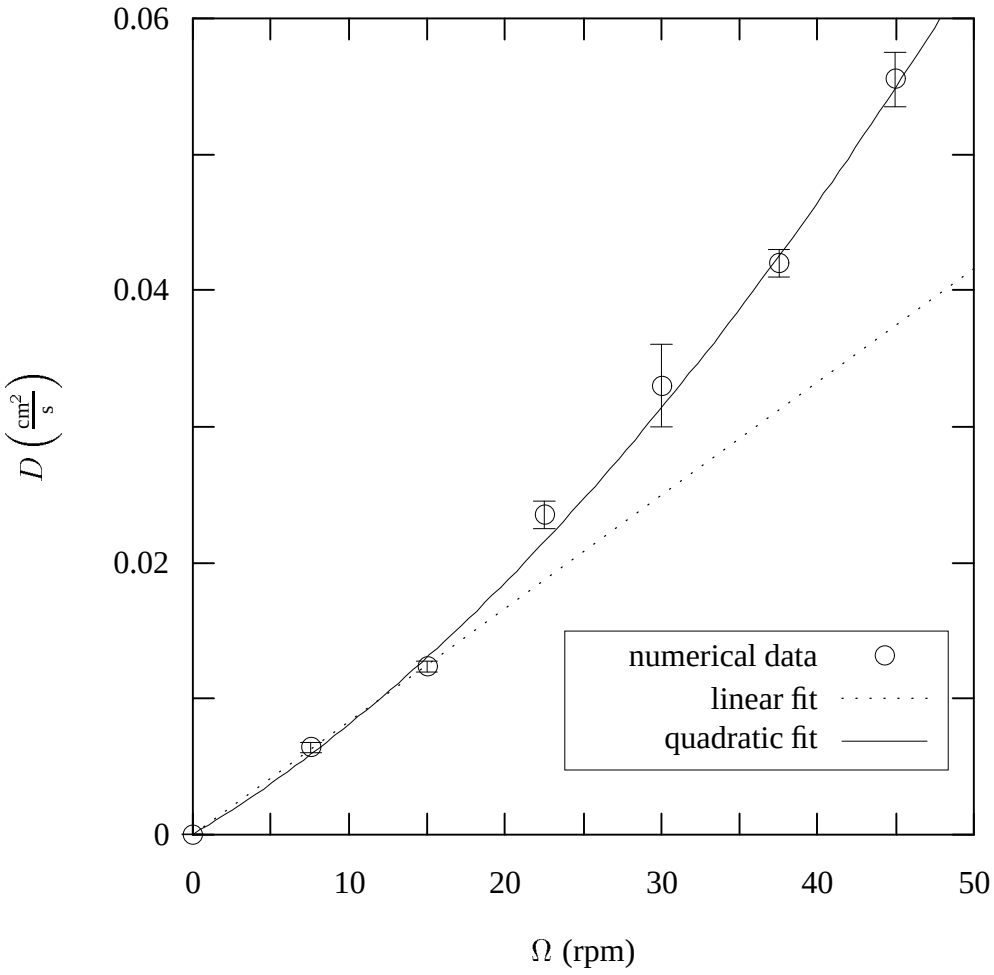

Figure 7.8: Diffusion coefficient for different values of the angular velocity Ω of the drum.

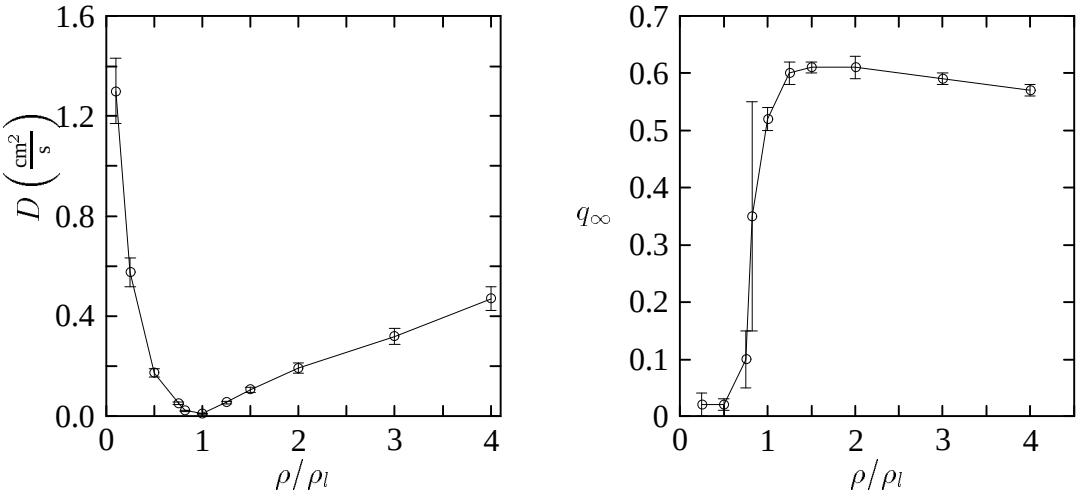

(a) diffusion coefficient D (b) q_∞-values

Figure 7.9: Different values of the density ratio $\frac{\rho}{\rho_l}$ of the small particles.

eventually the large particles will segregate into the radial core. For $\rho/\rho_l = 0.5$, the two competing effects of size- and mass segregation cancel each other and we get a perfect mixing of small and large particles indicated by a small value of q_∞ (see Chapter 6) in Fig. 7.9(b). Remembering our hypothesis that radial segregation will hinder diffusion from Sec. 7.2.2, we wonder why the diffusion coefficient starts to rise again for $\rho/\rho_l > 1$ where we get better segregation, whereas for $\rho/\rho_l < 1$ the diffusion coefficient rises as expected. In contrast to the previous section, we now have to take different densities for the particle into account. We are starting with an initial front where the small particles are on the left and the large particles on the right half of the drum (see Fig. 7.2). The pressure at the interface resulting from the particles above is in first approximation the hydrostatic pressure for granular media [Wieghardt, 1974]:

$$p = c\rho g\left(1 - e^{\frac{-h_d}{c}}\right) \tag{7.7}$$

where c is a parameter, which depends on the friction coefficient and the boundaries of the investigated geometry. The initial pressure for small depths h_d is like in a fluid $p = \rho g h_d$, but for larger h_d the pressure saturates exponentially to $p = \rho g c$, in contrast to all normal liquids. This general pressure dependence is by itself an interesting property for granular media and is independent of the grain size.

For density ratios different than 1, we get a pressure difference at the interface which itself enhances the mixing of the particles; this results in our simple model in a higher diffusion coefficient and will be more thoroughly discussed in Sec. 7.3. Hence for $\rho/\rho_l = 1$ we get a minimum in D.

7.3 Microscopic calculation of the flow properties

Another way to investigate the front diffusion is, to take a look at the trajectories of the individual particles. Here we get a microscopic diffusion coefficient D out of

$$\langle z(t)^2 \rangle - \langle z(t) \rangle^2 = 2Dt + \langle z(0) \rangle^2 \,, \tag{7.8}$$

where we look only on the displacement along the rotational axis of the particles and the average is done over all observed particles via

$$\langle . \rangle := \frac{1}{N} \sum_{i=1}^{N} .i \tag{7.9}$$

where N is the number of observed particles. In contrast to the previous section, where we incorporated everything into the diffusion constant, we now also consider a drift of the particles. This technique to obtain a microscopic diffusion constant is similar to the one used in the experiments by Zik and Stavans [1991], they investigated the diffusional behavior of vertically shaken granular material. There is also the possibility of a drift of the particles with velocity v, defined by the following relation:

$$\langle z(t) \rangle - \langle z(0) \rangle = vt \,. \tag{7.10}$$

Another possibility to obtain a diffusion coefficient would be

$$\langle (z(t) - z(0))^2 \rangle = 2Dt \,,$$

but there one would absorb a possible drift into the diffusion coefficient. It is therefore only useful for pure diffusion processes and thus will not be further used in this section, because we explicitly want to investigate the drift velocity and the diffusion coefficient separately.

7.3.1 Diffusion

To ignore the effect of the initial rearrangement during the first half second, we start our measurements $t = 0$ at the point when the continuous flow begins to start; i.e. after one eights of a revolution. To get a spatial resolution, we divide the drum into 14 slices and look at the diffusion coefficient in each slice for different density ratios and compare it to an unary mixture of large particles (shown in Fig. 7.10(a)). One thing to note is that the diffusion for the unary mixture and the binary mixture with equal density is nearly the same despite the size differences in the binary mixture, this shows the magnitude of the effect of different densities.

In Fig. 7.10(b) we distinguish for $\rho/\rho_l = 0.5$ between the small and large particles. The squares [$\square$] denotes the average diffusion coefficient, as it was used in Fig. 7.10(b), the cross [$\times$] (triangle [$\triangle$]) the diffusion coefficient separately for the small (large) particles.

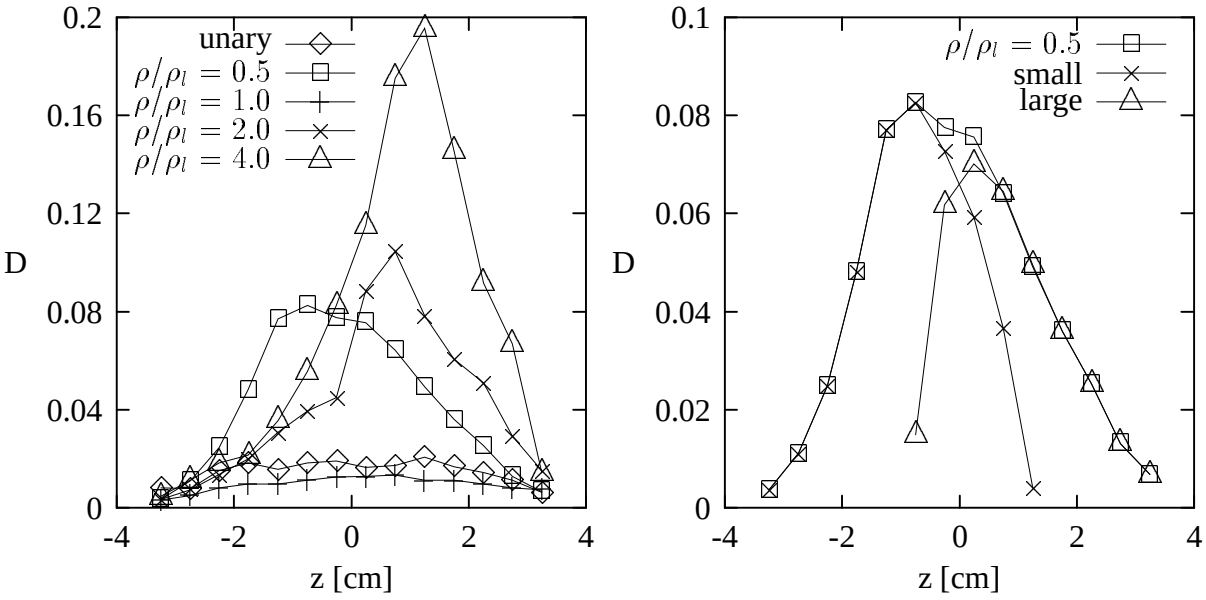

(a) Diffusion coefficient for different density ratios.

(b) Diffusion coefficient calculated separately for the small and large particles for $\rho/\rho_l = 0.5$

Figure 7.10: Microscopic calculated diffusion coefficients.

The maximum for the small particles is larger than for the large particles, whereas for $\rho/\rho_l \gtrsim 1$ the larger particles have a larger maximum diffusion coefficient. This also confirms the experimental observation that for particles with the same density the large particles have a higher mobility than the small particles [Das Gupta et al., 1991]. It is also nicely seen, (Fig. 7.10(b)), that the maximum diffusion coefficient for the small particles is in the region, where the small particles have been initially. For the large particles the maximum value of the diffusion coefficient is in the region where the large particles have been initially.

For density ratios not equal to one, the diffusion increases dramatically. In the case where $\rho/\rho_l > 1$ the maximum diffusion coefficient can be found in the region of the larger particles ($z > 0$cm) and for $\rho/\rho_l < 1$ in the region of the smaller particles; i.e. the region with lower particle density has a higher diffusion coefficient. But in each case the maximum value of the diffusion coefficient is close to the middle.

7.3.2 Drift

Looking also on the drift velocity in each slice (see Eq. (7.10) and shown in Fig. 7.11(a)) we see that for density ratios of one the drift velocities of the particles is around zero, whereas for $\rho/\rho_l \neq 1$ a drift clearly exists. This can be explained by applying a “hydrostatic picture” again: The hydrostatic pressure at the interface is given by Eq.(7.7). If we

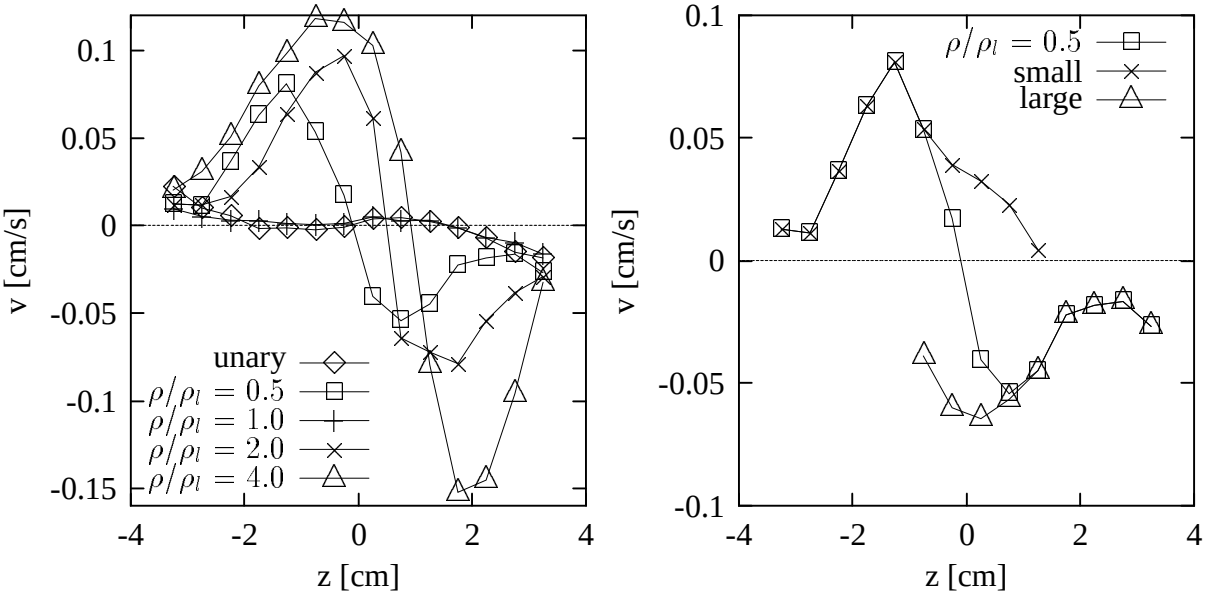

(a) Drift velocity for different density ratios.

(b) Drift velocities calculated separately for the small and large particles for $\rho/\rho_l = 0.5$.

Figure 7.11: Microscopic calculated drift velocities.

now have two different values for ρ at the interface, there will be a pressure difference of

$$\Delta p \propto |\rho - \rho_l| g \left(1 - e^{\frac{-h_d}{c}}\right) \tag{7.11}$$

which causes the drift. This drift will not happen on the free surface (where the pressure difference is zero), instead the denser particle will push their way through the lighter ones near the center of revolution, which is well below the rotational axis. So even the "roller coaster" effect (Sec. 7.2.2) still applies here, due to the motion inside the granular material we get a drift in the case of two different densities for the particles.

Splitting up the drift velocities for small and large particles for $\rho/\rho_l = 0.5$ (Fig. 7.11(b)) we see that the large particles at the boundary ($z < -2.5$cm) do nearly not drift at all, whereas for regions near the initial interface the drift is very large; but all large particles have a drift to the side with the small particles, even when they are already in the region with mainly small particles. For small particles the same is true, but the drift is always to the side with large particles.

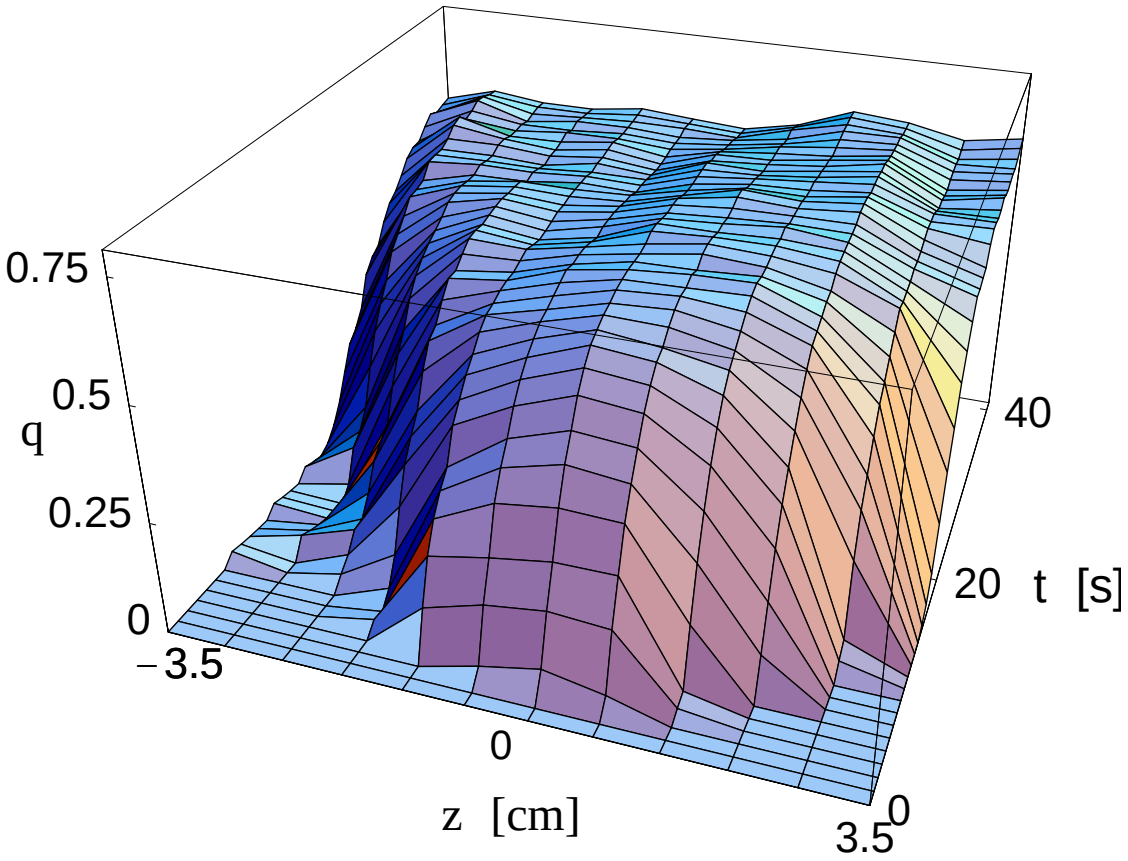

Figure 7.12: Time evolution of the radial segregation $(\rho/\rho_l = 2)$.

7.3.3 Front propagation with radial segregation

In a case where we get good radial segregation, e.g. $\rho/\rho_l = 2$, we take a look on the spatially resolved order parameter $q(t, z)$ shown in Fig. 7.12. In the beginning, we have $q(0\text{s}, z) = 0$, because we have either only large or only small particles (each an unary mixture by itself), hence there is no radial segregation by definition. For later times, we get nearly immediate radial segregation when small and large particles are getting axially mixed. This can be seen in Fig. 7.12 where the slope of $q(t, z)$ is very steep in t direction and saturates everywhere to approximately the same value of $q_\infty = 0.60$; also it takes more time for the particles to get to a slice which is more apart from the initial front, the slope there starts later. After ca. 30s, there is a radial core throughout the drum, despite that the concentration profile still has not reached the steady state. We also verified the existence of the core visually by using AVS[1] (a sample slice is shown in Fig. 2.1(b)). But how the drift of the particles takes place is much better seen when we have no radial segregation.

[1] AVS - Advanced Visualizing System

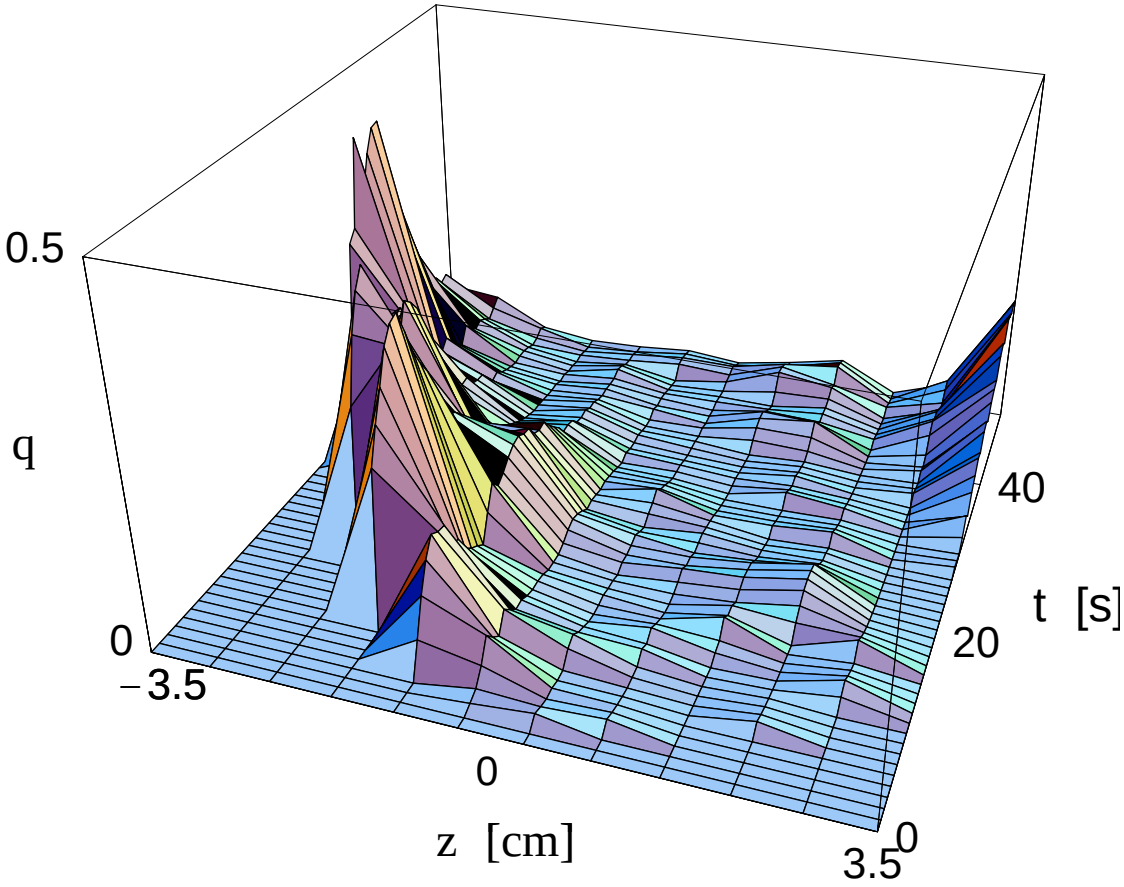

Figure 7.13: Time evolution of the radial segregation $(\rho/\rho_l = 0.5)$ ("segregation wave").

7.3.4 Front propagation without radial segregation

When the effects of size segregation and density segregation cancel each other, we have least radial segregation (for our size ratios $\rho/\rho_l = 0.5$). In contrast to the case with $\rho/\rho_l = 2$, the final order parameter q_∞ is around zero.

Due to the effective higher friction of the particles at the end caps, the small particles maybe able to segregate radially (see Sec. 7.2.2), this would also explain the increasing value of q at the right cylinder boundary for large times $t > 30$s.

Here the large particles are the denser ones and so, they push into the region of the smaller particles (direction to the negative z). Plotting our order parameter for this case (Fig. 7.13), gives an entirely different picture than Fig. 7.12. The starting condition is the same as before, but from the position of the front there starts a "segregation wave" into the region of small particles which ends at the wall and finally dissolves, whereas to the right in the region of large particles nothing drastic happens. In the "segregation wave", as mentioned before, the denser particles will push into the lighter particles as a core coming from the interface. This process is demonstrated in Fig. 7.14, for three

different times by taking a cross section of the drum in three different regions of the small particles. Shortly after the rotation of the drum started at $t = 1.3$s, we see a core of large particles near the initial interface (Fig. 7.14(c)), a smaller one in a more distant region (Fig. 7.14(b)) and none nearly halfway to the drum boundary (Fig. 7.14(a)). Here the core of large particles has not yet reached the drum boundary and we also see that no large particle happens to be in the free surface layer, so it is a pure core is flow of large particles. Two drum revolutions later, the core extends far into the left half of the drum (Fig. 7.14(d)) and it starts to dissolve where it was in the previous revolutions (Fig. 7.14(e) and Fig. 7.14(f)). Five revolutions later the whole core dissolved and we have a nicely mixed binary mixture (Fig. 7.14(g), Fig. 7.14(h) and Fig. 7.14(i)).

This core movement of denser material also shows the possibility for other mechanism, than free surface flow, to exists that effects front advancement or axial segregation.

Looking at the diffusion in direction to the region of large particle, there is nearly no change of q from zero; here the small particles flow in the free surface and get directly mixed into the large ones (also verified by AVS).

7.4 Results

We started with an initially sharp front of particles with different properties and looked how this front gets diffused. In the first part of this chapter we showed that this process can be well approximated by a pure diffusional process, for particles with the same density. Also we found that radial segregation hinders diffusion, because the process of radial segregation will sort the smaller particles out which are then unable to take place in the diffusion process.

When changing the density of the small particles, we get least mixing for particles with the same density. For different density there is a pressure difference at the interface and the denser particles will penetrate into the lighter ones. This is not a pure diffusional process anymore, because of the non vanishing drift of the particles, it is more like a core movement combined with diffusion.

Previous to this work the core was mostly thought to be a solid block in which no (or just minimal) movements can take place. We now showed that for different particle densities, and maybe also for other different particle properties, core movement is indeed possible. This could shed light on future work of the axial segregation mechanism.

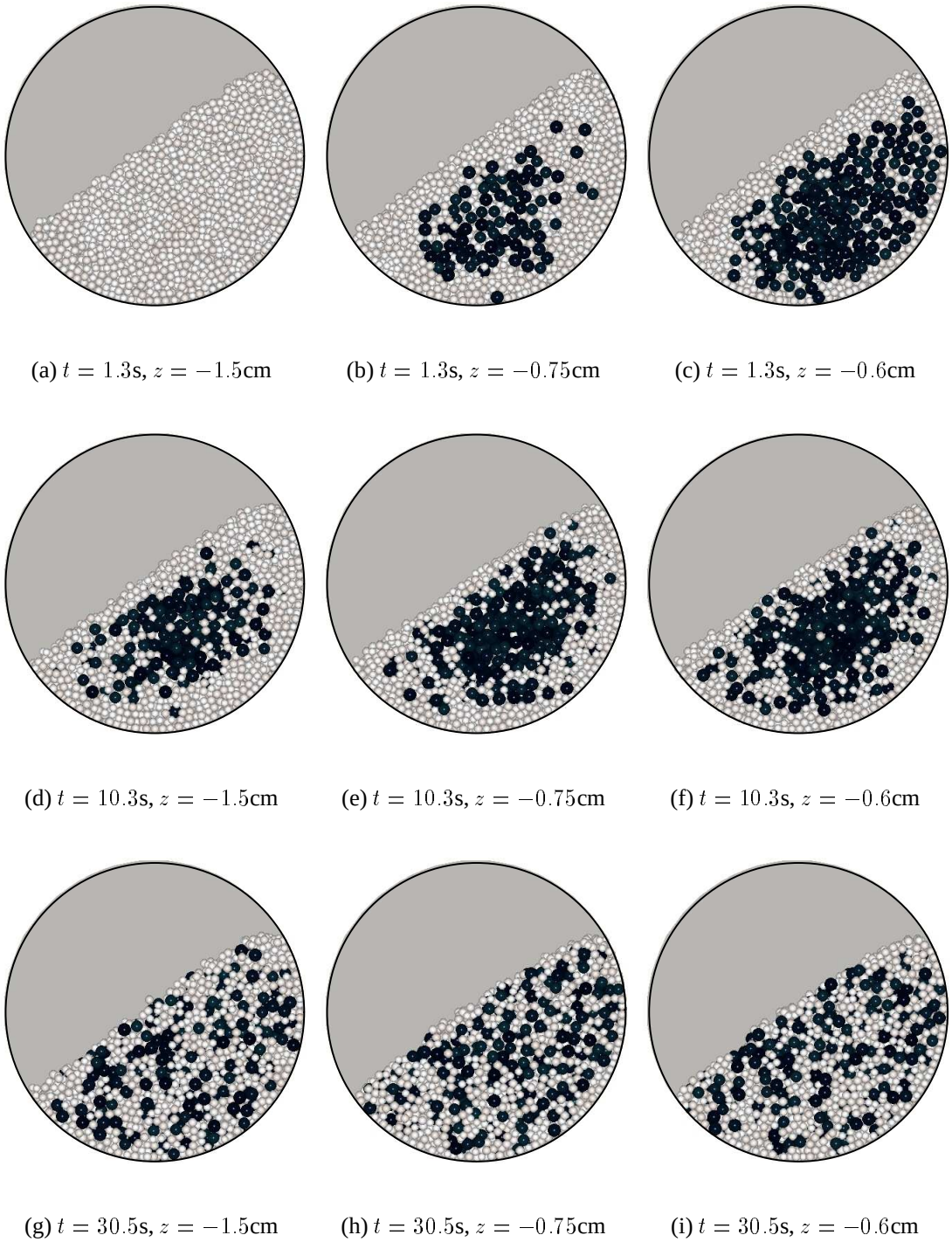

(a) $t = 1.3$s, $z = -1.5$cm (b) $t = 1.3$s, $z = -0.75$cm (c) $t = 1.3$s, $z = -0.6$cm

(d) $t = 10.3$s, $z = -1.5$cm (e) $t = 10.3$s, $z = -0.75$cm (f) $t = 10.3$s, $z = -0.6$cm

(g) $t = 30.5$s, $z = -1.5$cm (h) $t = 30.5$s, $z = -0.75$cm (i) $t = 30.5$s, $z = -0.6$cm

Figure 7.14: Core movement for $\rho/\rho_l = 0.5$.

Bibliography

M. P. Allen and D. J. Tildesley. *Computer Simulation of Liquids*. Oxford University Press, Oxford, 1987.

G. Baumann. *Mixing of granular material in a two-dimensional rotating drum*. PhD thesis, University of Duisburg, Duisburg, Germany, 1997.

G. Baumann, I. Janosi, and D. E. Wolf. Particle trajectories and segregation in a two-dimensional rotating drum. *Europhys. Lett.*, 27:203, 1994.

G. Baumann, I. M. Janosi, and D. E. Wolf. Surface properties and flow of granular material in a two-dimensional rotating drum model. *Phys. Rev. E*, 51:1879, 1995.

R. P. Behringer. Mixed predictions. *Nature*, 374:15, 1995.

J.-P. Bouchaud, M. E. Cates, J. R. Prakash, and S. F. Edwards. Hysteresis and metastability in a continuum sandpile model. *Phys. Rev. Lett.*, 74:1982, 1995.

J. Bridgewater. Fundamental powder mixing mechanisms. *Powder Technol.*, 15:215, 1976.

D. S. Cahn and D. W. Fuerstenau. Simulation of diffusion mixing of particulate solids by monte carlo techniques. *Powder Technol.*, 1:174, 1967.

F. Cantelaube. *Ecoulement granulaires dans un tambour à deux dimensions, Ségégation*. PhD thesis, University of Rennes I, Rennes, France, 1995.

F. Cantelaube and D. Bideau. Radial segregation in a 2d drum: an experimental analysis. *Europhys. Lett.*, 30:133, 1995.

R. Chicharro, R. Peralta-Fabi, and R. M. Velasco. Segregation in dry granular systems. In R. P. Behringer and J. T. Jenkins, editors, *Powders & Grains 97*, page 479, Rotterdam, 1997. Balkema.

K. Choo, T. C. A. Molteno, and S. W. Morris. Traveling granular segregation patterns in a long drum mixer. preprint, 1997.

E. Clément, J. Rajchenbach, and J. Duran. Mixing of a granular material in a bidimensional rotating drum. *Europhys. Lett.*, 30:7, 1995.

J. Crank. *The Mathematics of Diffusion*. Oxford University Press, London, 1975.

P. Cundall and O. D. L. Strack. A discrete numerical model for granular assemblies. *Géotechnique*, 29:47, 1979.

S. Das Gupta, D. V. Khakar, and S. K. Bathia. Axial segregation of particles in a horizontal rotating cylinder. *Chem. Engineering Science*, 46:1513, 1991.

M. B. Donald and B. Roseman. Mixing and demixing of solid particles. *Br. Chemical Engineering*, 7:749, 1962.

S. N. Dorogovtsev. Avalanche mixing of granular solids. *Europhys. Lett.*, 41:25, 1998.

T. G. Drake and O. R. Walton. Comparison of experimental and simulated grain flows. *J. Appl. Mech.*, 62:131, 1995.

Y. Du, H. Li, and L. P. Kadanoff. Breakdown of hydrodynamics in a one-dimensional system of inelasatic particles. *Phys. Rev. Lett.*, 74:1268, 1995.

C. M. Dury, R. Knecht, and G. H. Ristow. Size segregation of granular materials in 3d rotating drum. In P. Sloot, M. Bubak, and B. Hertzenberger, editors, *Lecture Notes in Computer Science 1401 – High-Performance Computing and Networking*, page 860, Berlin, 1998a. Springer.

C. M. Dury, I. Rehberg, and G. H. Ristow. *Lecture Notes in Physics – Dynamics of granular flow*, chapter 11, page 0. Springer, Berlin, 1998b.

C. M. Dury and G. H. Ristow. Radial segregation in a two-dimensional rotating drum. *J. Phys. I France*, 7:737, 1997.

C. M. Dury and G. H. Ristow. Competition of mixing and segregation in rotating cylinders. submitted to Physics of Fluids, 1998a.

C. M. Dury and G. H. Ristow. Radial segregation through axial migration. preprint, 1998b.

C. M. Dury, G. H. Ristow, J. L. Moss, and M. Nakagawa. Boundary effects on the angle of repose in rotating cylinders. *Phys. Rev. E*, 57:4491, 1998c.

C. M. Dury, G. H. Ristow, and M. Nakagawa. Angle of repose in a rotating drum. In R. P. Behringer and J. T. Jenkins, editors, *Powders & Grains 97*, page 499, Rotterdam, 1997. Balkema.

P. Evesque and J. Rajchenbach. Characterization of glass bead avalanches by using the technique of a rotating calinder. *C.R. Acad. Sci. Paris, Série II*, 307:223, 1988.

S. F. Foerster, M. Y. Louge, H. Chang, and K. Allia. Measurements of the collision properties of small spheres. *Phys. Fluids*, 6:1108, 1994.

V. Frette and J. Stavans. Avalanche-mediated transport in a rotated granular mixture. *Phys. Rev. E*, 56:6981, 1997.

A. Goldshtein and M. Shapiro. Mechanics of collisional motion of granular materials. part 1. general hydrodynamic equations. *J. Fluid Mech.*, 282:75, 1995.

W. Hager, S. Linz, and P. Hänggi. Surface flow of rotated granular systems and the impact of micromechanical stochastics. In D. E. Wolf and P. Grassberger, editors, *Friction, Arching, Contact Dynamics*, page 317, Singapore, 1997. World Scientific.

K. M. Hill, A. Caprihan, and J. Kakalios. Bulk segregation in rotated granular material measured by magnetic resonance imaging. *Phys. Rev. Lett.*, 78:50, 1997a.

K. M. Hill and J. Kakalios. Reversible axial segregation of binary mixtures of granular materials. *Phys. Rev. E*, 49:3610, 1994.

K. M. Hill and J. Kakalios. Reversible axial segregation of rotating granular media. *Phys. Rev. E*, 52:4393, 1995.

K. M. Hill, J. Kakalios, K. Yamane, Y. Tsuji, and A. Caprihan. Dynamic angle of repose as a function of mixture concentration: Results from mri experiments and dem simulations. In R. P. Behringer and J. T. Jenkins, editors, *Powders & Grains 97*, page 483, Rotterdam, 1997b. Balkema.

R. Hogg, D. S. Cahn, T. W. Healy, and D. W. Fuerstenau. Diffusion mixing in an ideal system. *Chem. Engineering Science*, 21:1025, 1966.

H. M. Jaeger, S. R. Nagel, and R. P. Behringer. The physics of granular materials. *Physics Today*, 4:32, 1996.

J. T. Jenkins and S. B. Savage. A theory for the rapid flow of identical, smooth, nearly elastic, spherical particles. *J. Fluid Mech.*, 130:187, 1983.

K. L. Johnson. *Contact Mechanics*. Cambridge University Press, Cambridge, 1985.

D. V. Khakhar, J. J. McCarthy, and J. M. Ottino. Radial segregation of granular mixtures in rotating cylinders. *Phys. Fluids*, 9:3600, 1997a.

D. V. Khakhar, J. J. McCarthy, T. Shinbrot, and J. M. Ottino. Transverse flow and mixing of granular materials in a rotating cylinder. *Phys. Fluids*, 9:31, 1997b.

G. Kuwabara and K. Kono. Restitution coefficient in a collision between two spheres. *Jap. J. Appl. Phys.*, 26:1230, 1987.

M. Y. Louge. Computer simulations of rapid granular flows of spheres interacting with a flat, frictional boundary. *Phys. Fluids*, 6:2253, 1994.

C. K. K. Lun, S. B. Savage, D. J. Jeffrey, and N. Chepurniy. Kinetic theories for granular flow: Inelastic particles in couette flow and slightly inelastic particles in a general flowfield. *J. Fluid Mech.*, 140:223, 1984.

G. Metcalfe and M. Shattuck. Pattern formation during mixing and segregation of flowing granular materials. *Physica A*, 233:709, 1996.

G. Metcalfe, T. Shinbrot, J. J. McCarthy, and J. M. Ottino. Avalanche mixing of granular solids. *Nature*, 374:39, 1995.

M. Nakagawa. Axial segregation of granular flows in a horizontal rotating cylinder. *Chem. Engineering Science-Shorter Communications*, 49:2544, 1994.

M. Nakagawa. private communication, 1997.

M. Nakagawa, S. Altobelli, A. Caprihan, E. Fukushima, and E.-K. Jeong. Non-invasive measurements of granular flows by magnetic resonance imaging. *Experiments in Fluids*, 16:54, 1993.

M. Nakagawa, S. A. Altobelli, A. Caprihan, and E. Fukushima. Nmri study: Axial migration of radially segregated core of granular mixtures in a horizontal rotating cylinder. *Chem. Engineering Science*, 52:in press, 1997a.

M. Nakagawa, J. L. Moss, K. Nishimura, and T. Ozeki. Stable configuration of binary mixtures in a horizontal rotating cylinder: Axial migration of granular particles. In R. P. Behringer and J. T. Jenkins, editors, *Powders & Grains 97*, page 495, Rotterdam, 1997b. Balkema.

N. Nityanand, B. Manley, and H. Henein. An analysis of radial segregation for different sized spherical solids in rotary cylinders. *Metall. Trans. B*, 17:247, 1986.

Y. Oyama. *Bull. Inst. Phys. Chem. Res. (Tokyo), Rep.*, 18:600, 1939.

R. Peralta-Fabi, E. Morales, and V. Romero-Rochin. On the dynamics of avalanches for 2d systems. In R. P. Behringer and J. T. Jenkins, editors, *Powders & Grains 97*, page 499, Rotterdam, 1997. Balkema.

B. A. Peratt and J. A. Yorke. Continuous avalanche mixing of granular solids in a rotating drum. *Europhys. Lett.*, 35:31, 1996.

F. Radjai, J. Schäfer, S. Dippel, and D. Wolf. Collective friction of an array of particles: A crucial test for numerical algorithms. *J. Phys. I France*, 7:1053, 1997.

J. Rajchenbach. Flow in powders: From discrete avalanches to continuous regime. *Phys. Rev. Lett.*, 65:2221, 1990.

G. H. Ristow. Granular dynamics: a review about recent molecular dynamics simulations of granular materials. In D. Stauffer, editor, *Annual Reviews of Computational Physics I*, page 275, Singapore, 1994a. World Scientific.

G. H. Ristow. Particle mass segregation in a two-dimensional rotating drum. *Europhys. Lett.*, 28:97, 1994b.

G. H. Ristow. Dynamics of granular materials in a rotating drum. *Europhys. Lett.*, 34: 263, 1996.

G. H. Ristow and M. Nakagawa. Shape dynamics of segregation front in rotating cylinders. submitted to *Phys. Rev. Lett.*, 1998.

G. H. Ristow, F.-X. Riguidel, and D. Bideau. Different characteristics of the motion of a single particle on a bumpy inclined line. *J. Phys. I France*, 4:1161, 1994.

H. E. Rose. A suggested equation relating to the mixing of powders and its application to the study of the performance of certain types of machine. *Trans. Instn Chem. Engrs.*, 37:4, 1959.

J. Schäfer, S. Dippel, and D. E. Wolf. Force schemes in simulations of granular materials. *J. Phys. I France*, 6:5, 1996.

C. Tang and P. Bak. Critical exponents and scaling relations for self-organized critical phenomena. *Phys. Rev. Lett.*, 60:2347, 1988.

L. Vanel, A. D. Rosato, and R. Dave. Rise-times regimes of a large sphere in vibrated bulk solids. *Phys. Rev. Lett.*, 78:1255, 1997.

O. R. Walton and R. L. Braun. Simulation of rotating-drum and repose tests for frictional spheres and rigid sphere clusters. In M. Roco and S. Plasynski, editors, *Proceedings of the joint DOE/NFS workshop on FLOW OF PARTICULATES AND FLUIDS*, New York, 1993. Ithaca.

K. Wieghardt. *Theoretische Strömungslehre*. Teubner, Stuttgart, 1974.

J. C. Williams. The segregation of particulate materials. a review. *Powder Technol.*, 15: 245, 1976.

O. Zik, D. Levine, S. G. Lipson, S. Shtrikman, and J. Stavans. Rotationally induced segregation of granular materials. *Phys. Rev. Lett.*, 73:644, 1994.

O. Zik and J. Stavans. Self-diffusion in granular flows. *Europhys. Lett.*, 16:255, 1991.

Index